DOCTORAATSPROEFSCHRIFT

2008 | Faculteit Wetenschappen

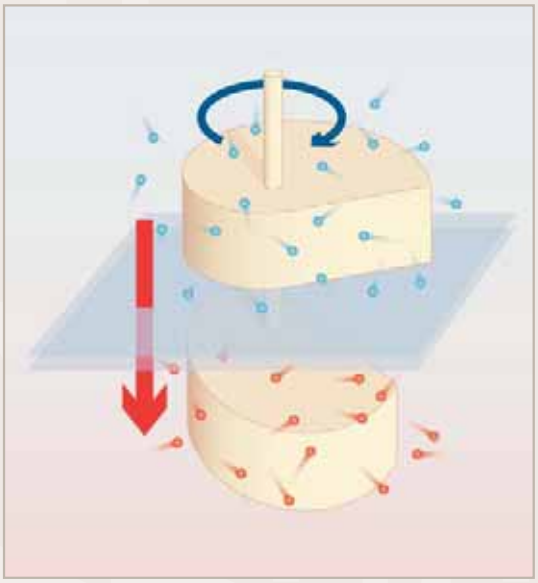

Cooling with Chirality
Investigations in the world of Brownian machines

Proefschrift voorgelegd tot het behalen van de graad van
Doctor in de Wetenschappen, richting natuurkunde, te verdedigen door:

Martijn VAN DEN BROEK

Promotor: prof. dr. Christian Van den Broeck

universiteit hasselt

DOCTORAATSPROEFSCHRIFT

2008 | Faculteit Wetenschappen

Cooling with Chirality
Investigations in the world of Brownian machines

Proefschrift voorgelegd tot het behalen van de graad van
Doctor in de Wetenschappen, richting natuurkunde, te verdedigen door:

Martijn VAN DEN BROEK

Promotor: prof. dr. Christian Van den Broeck

D/2008/2451/49

universiteit hasselt

Contents

—1—

Introduction

1.1 The world of Brownian machines

It is difficult for us, living in a "macroscopic" environment, to imagine the world at the nanoscale. It is a hostile and restless environment. For a nanoparticle in a fluid or gaseous medium, fluctuations are omnipresent. Its energy will continually change in units of k_BT, with k_B the Boltzmann constant and T the temperature of the environment. The effects of such energy fluctuations were demonstrated [1] by the observation of kinesin molecules climbing the cytoskeletal track in a juddering motion (Fig. 1.1). The motion of F_1-ATPase, a 10 nm small molecular machine that can pump ions through a membrane by the hydrolysis of ATP molecules (the molecules that provide the energy in living systems) was captured in a movie (Fig. 1.2): it rotates, but in a jiggling, seemingly erratic way [2, 3].

It will be obvious that our familiar macroscopic notions of how machines can convert energy into useful purposes cannot be simply transferred to the nanoworld. In fact, Nature already shows us very efficient alternative methods to operate on the nanoscale. The intertwinement between the current advances in nanotechnology and the growing understanding of biological systems on the molecular scale, is discussed by

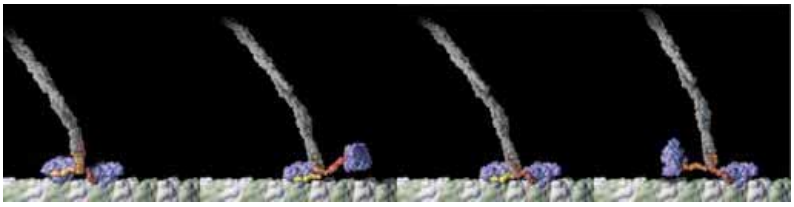

Figure 1.1: The step-like motion of kinesin molecules in the body is subject to random fluctuations.

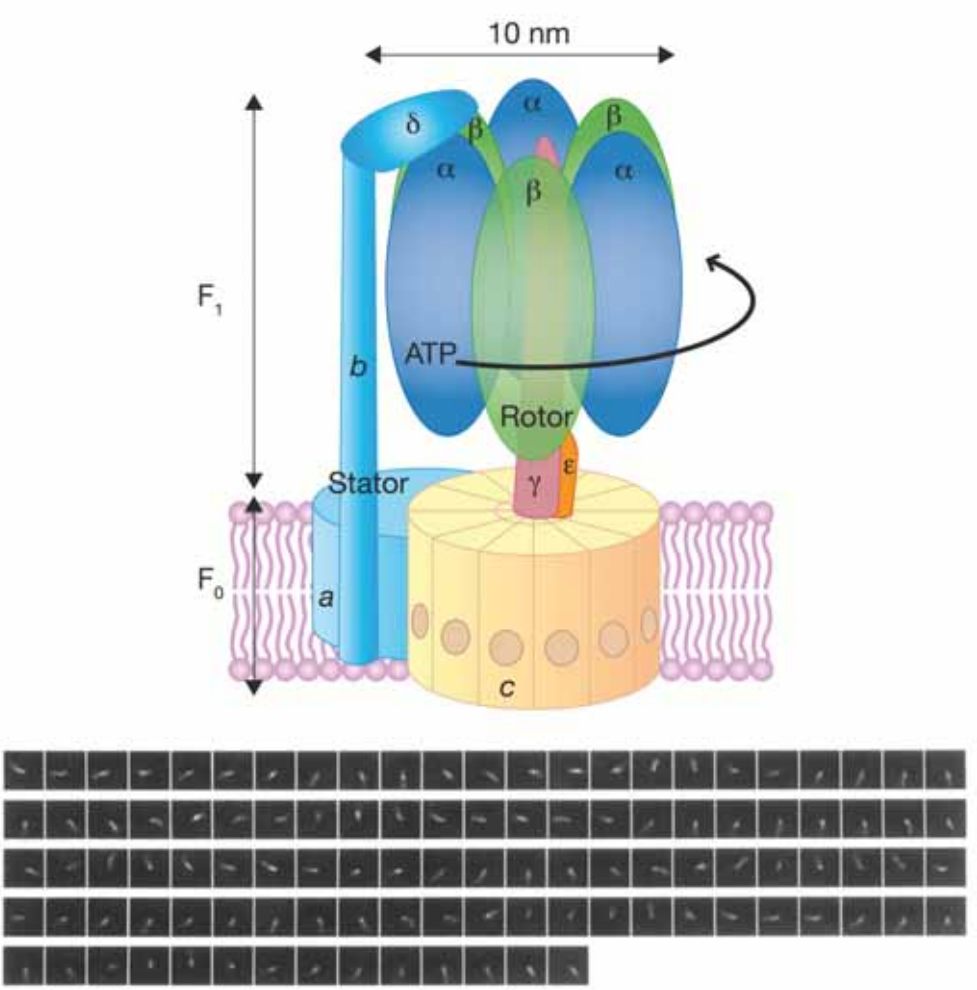

Figure 1.2: Upper figure: F_1-ATPase is a naturally occurring rotating molecular motor. It works as a pump for ions through a membrane. Its driving force is chemical, through the hydrolysis of ATP. Our interest in this molecular motor lies in its environment (in the cytoplasm, subject to fluctuations), its construction (rotational, and through a biological membrane), its physical characteristics (size of the order of 10 nm) and dynamical properties (rotational frequency of the order of 100 Hz). Lower figure: Sequential images of a rotating actin filament attached to the γ-subunit in $\alpha_3\beta_3\gamma$ subcomplex (from [2]).

Hänggi and Marchesoni in their very recent review paper [4] on artificial Brownian motors: *Nanotechnology has been intricately linked with biological systems since its inception. Fascinated by the complexity and smallness of the cell, Feynman [5] challenged the scientific community to "make a thing very small which does what we want". In his visionary response, Drexler [6] proposed to focus on protein synthesis as a pathway for creating nanoscale devices. Both Feynman and Drexler's propositions have been met with much skepticism as accurate manipulations at the nanoscale were deemed impossible. However, in view of the recent advances in systems biology [7], cellular mechanisms are now being cited as the key proof of the nanotechnological viability of devices with atomic precision. In spite of their established complementarity, a fundamental difference between systems biology and nanotechnology is their ultimate goal. Systems biology aims to uncover the fundamental operation of the cell in an effort to predict the exact response to specific stimuli and genetic variations, whereas nanotechnology is chiefly concerned with useful design. Manufacturing nanodevices through positional assembly and self-assembly of biological components available at the cellular level is the goal of the so-called biomimetic approach – as opposed to the inorganic approach aimed at fabricating nanomechanical devices in hard, inorganic materials (e.g., using modern lithographic techniques, atomic force and scanning tunneling microscopy, etc). Nature has already proven that it is possible to engineer complex machines on the nanoscale; there is an existing framework of working components manufactured by Nature than can be used as a guide to develop our own biology inspired nanodevices. It is also true that the molecular machinery still outperforms anything that can be artificially manufactured by many orders of magnitude. Nevertheless, inorganic nanodevices are attracting growing interest as a viable option due to their potential simplicity and robustness, without forgetting that inorganic nanodevices may provide additional experimental access to the molecular machinery itself.* With regard to the inorganic approach to nanodevices, Hänggi and Marchesoni, in the same review, also put forward three interesting main assumptions: *(1) That, in view of the most recent developments on nonequilibrium thermodynamics, the science of nanodevices, regardless of the fabrication technique, is inseparable from the thermodynamics of microscopic engines; (2) That the fabrication techniques on the nanoscales become more and more performing following*

the trend of the last two decades; (3) That a better understanding of the molecular machinery can help devise and implement new transport and control mechanisms for biology inspired nanodevices. In other words, we bet on a two-way crossfertilization between the biomimetic and the inorganic approach. These main assumptions also form the premises of our own investigations in the world of nanomachines. As an illustration of the rapid advances in nanotechnology, we mention the very recent report [8] of the construction of an array of anchored nanosized rotors on a gold surface, see Fig. 1.3.

The quintessential example of such a nanomachine operating under the influence of fluctuations is the *Brownian motor*. Such a device exploits unbiased thermal fluctuations to drive directed motion. Brownian motion was first detected in 1827 by botanist Robert Brown while examining pollen grains and the spores of mosses and Equisetum suspended in water under a microscope. Brown observed minute particles within vacuoles in the pollen grains executing a continuous jittery motion. These particles made a *random walk*, but on average did not show systematic displacement. Albert Einstein, in one of the landmark papers [9] he wrote in his annus mirabilis (1905), laid the theoretical foundations of the description of Brownian motion. The possibility to attain directed motion, or concomitantly, to gain useful work out of unbiased random fluctuations, was first raised by von Smoluchowski in 1912 [10] and was later popularized and extended by Feynman [11].

In their thought experiment, they considered a paddle rigidly connected through an axle with a so-called ratchet, resembling a circular saw with asymmetric sawteeth (Fig. 1.4). The device is imagined to be placed in a gas at thermal equilibrium. Random collisions with the gas molecules would then cause the device to exhibit rotational Brownian motion. Then, a pawl is added to the ratchet configuration, which seems to block the rotation in one sense, hence opening the potential of generating systematic rotational motion in one direction. If a small load is attached via a string to the axle, work could be performed, lifting the load against gravity while the string rolls up. Obviously, this mechanism contradicts the laws of thermodynamics. However, there is something fundamentally wrong in our predictions. The clue is in the thermal motion of the pawl itself, which is also subject to collisions with the gas particles. Every now and then, the pawl lifts itself up and the sawteeth

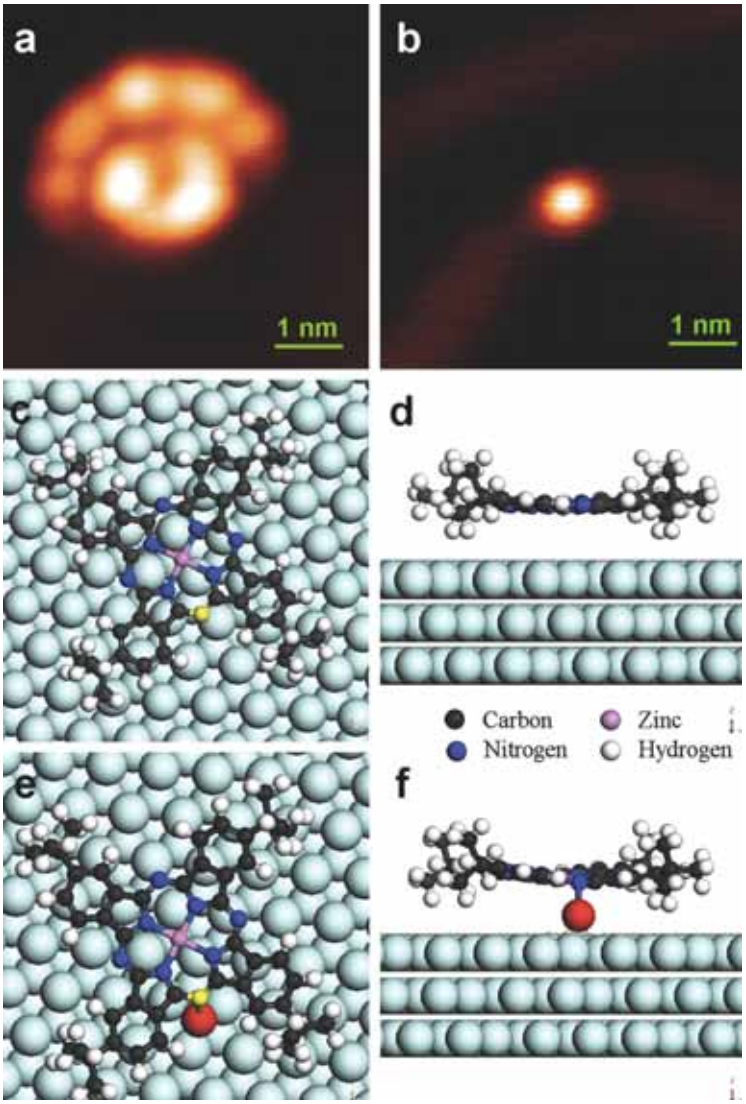

Figure 1.3: (a) STM image of single molecular rotor at the elbow position. (b) Bright spot found at the rotation center after the molecule observed in (a) was removed during scanning. (c) Top view and (d) side view of the optimized adsorption configuration of a (t-Bu)$_4$-ZnPc molecule on the released Au(111) surface. (e) Top view and (f) side view of the optimized configuration of a (t-Bu)$_4$-ZnPc molecule adsorbed on the Au(111) surface via a gold adatom. The molecular formula of (t-Bu)$_4$-ZnPc is $C_{48}H_{48}N_8Zn$. From [8].

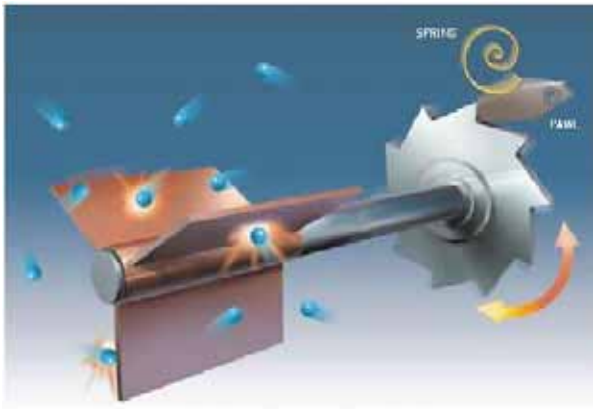

Figure 1.4: The ratchet and pawl mechanism.

can freely travel underneath. A detailed analysis of the probabilities for the ratchet to move forward and backward, when the paddle and ratchet are surrounded by gases at equal temperature, shows that the average rotation over time is zero. In spite of the built in asymmetry, no preferential direction of motion is possible. Feynman however goes one step further in considering the case that the gas around the paddles is in a box at temperature T_1, while the ratchet and pawl are in contact with a different bath (e.g., another gas in a box) at temperature $T_2 \neq T_1$. Such conditions do produce systematic rotation in one direction (the sense is determined by the sign of $T_1 - T_2$) and lifting a small load, or doing useful work, becomes possible. Note that here there is no violation of the second law of thermodynamics as we extract work from heat baths that are not at equilibrium with each other. We also mention the report of a misconception in the analysis of Feynman [12].

Ending our short discourse on the historic perspective, we wish to cite some landmark papers that appeared in the 1993-1994 period on the subject of directed transport and Brownian motors: Magnasco [13], Ajdari and Prost [14], Astumian and Bier [15], Bartussek et al. [16], Doering et al. [17], Prost et al. [18], Rousselet et al. [19]. After that, there was an outburst of work on the subject, for which we refer to some excellent review papers, and references therein [20, 21, 22, 4].

Returning our attention to the basic concept of the *Brownian motor*, we note that in addition to its operation in an environment of unbiased random fluctuations, its key attribute lies in the *breaking of underlying symmetries*, more specifically

1. the *symmetry of detailed balance*, governing thermal equilibrium dynamics,

2. the *spatial symmetry*.

It would lead us too far to summarize the multiplicity of theoretical, artificially realized or naturally occurring possibilities that conform to these prescriptions. We only mention the two most cited paradigms: the flashing and rocking ratchets [23], in which an external space-periodic but space-asymmetric forcing using a ratchet-like potential acts on a particle in a viscous environment. Theoretical models and solution methods based on Langevin-type equations (or the Fokker-Planck equation for the probability distribution) have become standard tools in nonequilibrium statistical physics. At variance however with the microscopically exact description of the fluctuations we present in subsequent chapters of this thesis, these models introduce an ad-hoc Gaussian (white or colored) noise.

Aside from the well-known Brownian motor, recent spectacular developments in nanotechnology have spurred intensive research in other functionalities. In the realm of mechanical devices, wheels, ratchets, pivots, shafts, barrels, which can function as gates, gears, switches, actuators, pedals, elevators, muscles, rotors, gyroscopes etc. have been reported [24, 25, 26, 27]. Another concept of particular interest is that of the Brownian refrigerator [28]. Such a device shows the potential to transport heat away from a hot region or to cool down a small compartment, akin in functionality to macroscopic heat pumps and refrigerators, but entirely different in its underlying mechanism.

1.2 Outline of the thesis

The work presented in Chapter 2 is the study of a new type of Brownian motor. The objective was to calculate the characteristics a of three-dimensional motor with convex constitutive parts using a perturbational

solution of the Boltzmann equation. Special emphasis was on obtaining estimates of the resulting sustained velocity for parameter values that correspond with physically realistic systems, in particular for nanoscale devices. The Brownian motor in question belongs to the category of *thermal Brownian motors*. Recollecting the discussion on the breaking of underlying symmetries in the previous section, this type of Brownian motor breaks detailed balance through the presence of its constitutive parts in separate heat baths at different temperature. The motion of the device is along a linear track. The necessary breaking of spatial symmetry is then accomplished through the asymmetry of the shape of the parts with respect to the remaining free direction of motion. Interactions with the heat bath are microscopically described by the collisions of the individual gas particles with the surface of the motor. Under the assumption of molecular chaos, the probability of the motor subjected to these interactions to assume a particular momentary velocity, can be described by a master-Boltzmann equation. The solution of this Boltzmann equation is through the calculation of the moments of the velocity, the first moment under stationary state conditions effectively representing the average sustained velocity. Only a perturbational solution in a small parameter given by the ratio of masses of a gas particle and the motor is attainable.

Various three-dimensional shapes for the parts were considered, along with the relative positioning of the parts. In addition to predictions of the friction coefficient and the diffusion coefficient based on entirely microscopic derivations, orders of magnitude were obtained for the predicted net velocity. As an example, for a motor consisting of cone-shaped silica units of size 20 nm, one obtains a drift speed of about $0.1\,\mu$m/s when subject to 0.1 K temperature difference in a gaseous environment.

In Chapter 3, we present the principal results of our study of a *rotating* thermal Brownian motor. A partial motivation for this work was that rotational motion is localized and possibly easier to realize than linear motion. The rotational Brownian motion is only similar to the linear Brownian motion described in Chapter 2 when the axis of rotation is far removed from the body of the motor. When the axis in close to, or in the interior of the body, the characteristics of the device were found to depend in an intriguing way on the location of the axis. While for the linear case the effect of the requirement of spatial asymmetry on concrete

shapes was rather obvious and predictable, this was certainly not the case for the rotational setup. In the latter, the *chirality* of the shape of the motor plays a key role. Under the assumption of a homogeneous interior, we arrived at an optimal shape for the motor parts that is far from trivial.

The analysis also here was entirely analytical, starting from the microscopic interactions of the motor with the environment. The obtained solutions for the dynamical behavior were in the form of moments of the angular velocity of the rotor. With physical parameters corresponding to small proteins we found typical sustained rotation frequencies of kHz for a 0.1 K temperature gradient.

As mentioned already, the concept of a nanoscale Brownian *cooling device* has exciting technological potential. We combined this concept with the introduced Brownian rotor setup, see Chapter 3 for the central results. The idea is simple: applying a torque on the rotor consisting of two chiral parts in separate gas compartments at equal temperature, will produce a heat flux from one container to the other. This phenomenon can be explained in terms of Le Chatelier's principle: a system in equilibrium that is externally perturbed will generate processes that counteract the original perturbation. This is similar to the effect of moving a ferromagnetic core into a coil. According to Lenz' law, currents will be induced in the coil, such that the resulting magnetic field will expel the core, hence counteracting the original disturbance. Other well-known examples of this principle are in its application to electro-thermal devices, displaying the Peltier, Seebeck and Thompson effects. The property that a Brownian motor can be turned into a Brownian refrigerator is, at least in the regime of linear response, a direct consequence of the Onsager reciprocity relations: if a temperature gradient generates motion, an applied force will generate a heat flux. The rectification of nonequilibrium thermal fluctuations provide the driving mechanism for Brownian refrigeration. The latter become more prominent, and so do the resulting motor and cooling functions, as the apparatus becomes smaller.

Apart from the described cooling flow, other currents appear while operating the Brownian refrigerator. There will be Joule dissipation when the motor is turned against a viscous medium, causing both gases to heat up. Fortunately, this frictional heating is proportional to the square of the torque's magnitude, while the cooling flux is proportional to the torque. This consideration leaves open a window of small torques that allows for

one reservoir to cool down. When a temperature gradient is achieved, an opposite flow, transporting heat from the hot to the cold compartment, in accordance with Fourier's law of heat conduction, will also inevitably appear, even if we would succeed in adiabatically enclosing the two compartments and minimizing the thermal conductivity of the rotor. This heat conduction arises solely from the dynamic interactions of the rotor with both gases. The crucial comparison of distinct heat flows (cooling, dissipative and conductive) and the specific role of the magnitude of the torque was examined in detail and led to additional ways to optimize the device's performance. These optimizations predict, for a nanoscale device, net cooling rates of the order of femtojoules per second. A parallel setup of multiple nanocoolers would enhance the cooling power accordingly. Similarly, the small sustainable temperature gradient of one device could be utilised to attain large temperature differences over macroscopic distances by a serial line-up of the devices.

For the work presented in Chapter 4 we turned to another remarkable feature of asymmetric Brownian particles: they display directed motion in an external unbiased and symmetric time-periodic force field. Under the influence of the external field, a Brownian particle will continuously be out of thermal equilibrium, hence detailed balance is broken. We introduced a generic formalism for the dynamical (linear or rotational) behavior that enabled us to quantify the net particle velocity. This formalism couples the deviation of the second moment of the particle's velocity from thermal equilibrium with the time evolution of the first moment of the velocity. The intrinsic asymmetry of the particle appears in this formalism as one dimensionless parameter. First order analytical expressions for the net velocity in terms of this asymmetry, the amplitude of the external forcing and the period of force modulation were derived for several force profiles and compared with numerical results. Event-driven molecular dynamics simulations of a rotational setup in an ideal gas setting confirmed the validity of our formalism. Consequently, we can predict that drift speeds comparable to thermal speeds are feasible for nanosized asymmetric Brownian particles under the described ratchet operation.

In Chapter 5 we revisit the chiral Brownian rotor and heat pump, introduced in Chapter 3. In addition to a comprehensive theoretical derivation in two and three spatial dimensions, we report a detailed study of the parameters, in particular the essential chiral shape and its opti-

mization. We also present recent molecular dynamics simulation results that substantiate our theoretical predictions for the dynamic and cooling behavior of the chiral device.

—2—

Rectifying the thermal Brownian motion of three-dimensional asymmetric objects

Published: M. van den Broek and C. Van den Broeck, Phys. Rev. E **78**, 011102 (2008).

–Abstract–

We extend the analysis of a thermal Brownian motor reported in Phys. Rev. Lett. **93**, 090601 (2004) by C. Van den Broeck, R. Kawai, and P. Meurs to a three-dimensional configuration. We calculate the friction coefficient, diffusion coefficient, and drift velocity as a function of shape and present estimates based on physically realistic parameter values.

2.1 Introduction

Spectacular advances in bio- and nanotechnology make it possible, not only to measure or observe, but also to manipulate and construct objects at a very small scale. At the same time there is growing interest in techniques which can add functionality. In particular, the development of molecular engines is a theme which has received great attention over the last two decades. The appearance of fluctuations in small systems has led to new concepts for characterizing or operating such devices, exploiting rather than fighting these very same fluctuations.

These so-called Brownian motors [21, 22] have an additional theoretical interest through their relation with the old issue of Maxwell demons and the second law of thermodynamics. In return, this theoretical connection allows to make statements on the efficiency of such engines [29, 30] or to transform them from engines into mini-refrigerators [28, 31]. Most of the studies on Brownian motors start with an ad hoc separation of systematic and noise terms, based on linear Langevin equations. This approach however offers little insight into the origin of the rectification of random fluctuations. As pointed out by van Kampen [32], the rectification of nonlinear fluctuations cannot be addressed starting from the standard Langevin description with additive Gaussian white noise. In [33, 34, 35, 36] a theoretical and numerical study of a thermal engine is presented in which rectification arises at the level of nonlinear response. The analysis therein starts from a microscopic description based on Newton's laws of motion. There is another related distinct feature of the model: the asymmetry of the thermal engine lies in the geometry of the motor itself, in contrast to the asymmetry imposed by the application of an external potential, appearing in the so-called flashing and rocking ratchet models.

The characteristic properties of the engine, such as the friction coef-

ficient, the speed and the diffusion coefficient, are calculated exactly in [33, 34, 35, 36] and are found to be in excellent agreement with the results from hard disk molecular dynamics. However, the results are reported in dimensionless units, in part due to the fact that the analysis was, for reasons of simplicity and for comparison with molecular dynamics, limited to the case of two dimensions. In view of the technological interest of motors in bio- and nanotechnology, we report here a full and detailed analysis of the three-dimensional version. Our analysis is particularly welcome in view of the spectacular developments in the nanotechnology of chemical, mechanical and electronic devices, including wheels, ratchets, pivots, shafts, barrels, which can function as gates, gears, switches, actuators, pedals, elevators, muscles, motors, rotors, gyroscopes etc.[24, 25, 26, 27].

This paper is organized as follows. First, the model, notations, and working hypothesis are introduced in section 2.2. The calculation method, based on the kinetic theory of gases, is presented in section 2.3, with a discussion of the analytical solution following in section 2.4. Finally, in section 2.5 we report and discuss the results for the friction coefficient, diffusion coefficient, and drift velocity as a function of shape and present estimates based on physically realistic parameter values.

2.2 The model

The model presented in [33] reproduces in a simplified way the principle ingredients of Feynman's ratchet and pawl mechanism [11]: a temperature difference between two reservoirs and the presence in at least one reservoir of an asymmetric object. The construction, extended to the case of three spatial dimensions, is as follows. We consider any number of reservoirs (denoted by index i), each containing a gas at equilibrium at a temperature T_i. Fig. 2.2 gives a schematic picture of the two-reservoir system. Solid objects with no internal degrees of freedom, called 'motor units', are located inside the containers. These objects are coupled rigidly to each other, so that the motor moves as a single entity, with total mass M, along a given straight axis, corresponding to its single translational degree of freedom. For simplicity, we disregard any rotational degree of freedom (for a detailed discussion of this case, see [31]).

Due to collisions with the gas particles (mass m), the motor will

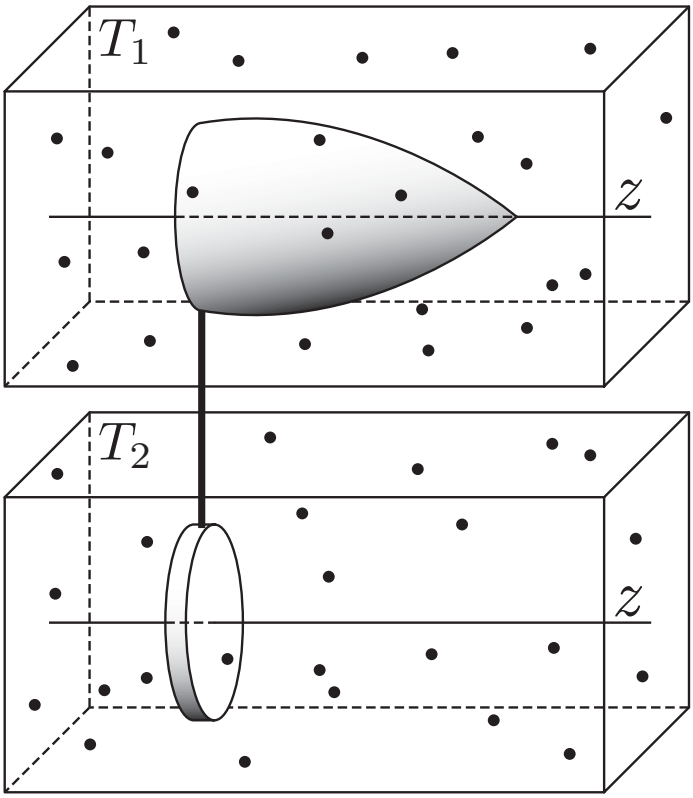

Figure 2.1: The two-reservoir model of the thermal engine: two solid objects are confined in separate containers (scaled down for illustration purposes) that contain gases at temperatures T_1 and T_2. The objects are assembled with a rigid connection. The ensemble can move freely along the z-axis.

change its velocity $V(t)$ in the course of time t. The statistics of these collisions can be described under the assumption of molecular chaos, which is valid when the gases are in the high Knudsen number regime and the containers are large enough to avoid acoustic and other boundary effects. In addition, the shape of the units' surfaces must be such that no re-collisions with the motor occur, namely for convex and closed shapes. With these assumptions, the precollisional velocities are random and uncorrelated. Hence the time evolution of the probability $P(V,t)$ that the motor has speed V at time t can be described by a master equation:

$$\frac{\partial P(V,t)}{\partial t} = \int dV' \left[W(V|V')P(V',t) - W(V'|V)P(V,t) \right]. \tag{2.1}$$

Here $W(V|V')$ represents the transition probability per unit time for the motor to change its speed from V' to V.

2.3 Kinetic theory

In this section we study the collisions of gas particles from either temperature reservoir with a motor part and derive the resulting total transition probability $W(V|V')$ for the motor to change speed from V' to V. We introduce a Cartesian coordinate system (x,y,z) where the z-axis points along the free direction of movement of the motor.

2.3.1 Conservation rules

A gas particle will, upon collision with a motor unit, undergo an instantaneous change of velocity from $\vec{v'} = (v'_x, v'_y, v'_z)$ before collision to $\vec{v} = (v_x, v_y, v_z)$ afterwards. Due to conservation of momentum along the free z-direction, one has:

$$mv'_z + MV' = mv_z + MV. \tag{2.2}$$

In addition, when the collision is perfectly elastic, the total energy is conserved:

$$\frac{1}{2}MV'^2 + \frac{1}{2}mv_x'^2 + \frac{1}{2}mv_y'^2 + \frac{1}{2}mv_z'^2 = \frac{1}{2}MV^2 + \frac{1}{2}mv_x^2 + \frac{1}{2}mv_y^2 + \frac{1}{2}mv_z^2. \tag{2.3}$$

We will also suppose that the collision is described in terms of a (short-range) central force, implying that the component of the momentum of the gas particle along any direction tangential to the surface of the motor is conserved. The orientation of the tangent plane to the motor surface is

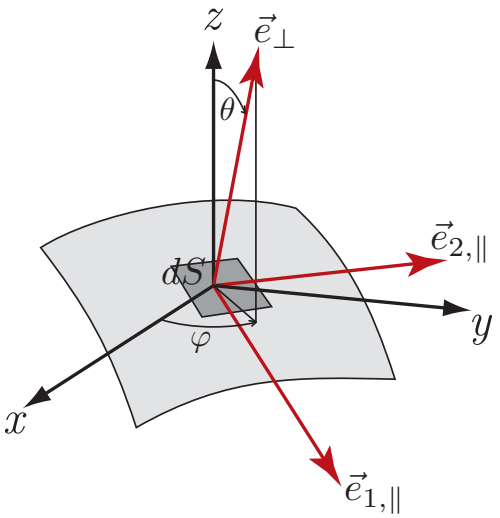

Figure 2.2: The orientation of an infinitesimal surface element dS is represented by an outer-pointing unit normal vector $\vec{e}_\perp$ and determined by the spherical coordinates φ and θ. The polar angle θ is measured from the z-axis, which is chosen as the free direction of movement of the motor. x, y complete the Cartesian coordinate system and the azimuthal angle φ starts from the x-axis. Two orthogonal unit vectors $\vec{e}_{1,\shortparallel}$ and $\vec{e}_{2,\shortparallel}$ determine the plane that is tangent to the motor unit in dS.

determined uniquely by a normal outward vector on an infinitesimal element dS of the surface at the point of collision. In spherical coordinates, this normal vector is given by

$$\vec{e}_\perp\big|_{\text{cart}} \doteq (\sin\theta\cos\varphi, \sin\theta\sin\varphi, \cos\theta), \tag{2.4}$$

with θ the polar angle from the z-axis ($0 \leqslant \theta \leqslant \pi$) and φ the azimuthal angle in the xy-plane from the x-axis ($0 \leqslant \varphi < 2\pi$), cf. Fig. 2.3.1.

We also introduce two mutually perpendicular unit vectors within the tangent plane:

$$\vec{e}_{1,\shortparallel} \doteq (\cos\theta\cos\varphi, \cos\theta\sin\varphi, -\sin\theta), \tag{2.5}$$

$$\vec{e}_{2,\shortparallel} \doteq (-\sin\varphi, \cos\varphi, 0), \tag{2.6}$$

so that we can write the conservation of tangential momentum as

$$\vec{v'} \cdot \vec{e}_{1,\shortparallel} = \vec{v} \cdot \vec{e}_{1,\shortparallel}, \tag{2.7}$$

$$\vec{v'} \cdot \vec{e}_{2,\shortparallel} = \vec{v} \cdot \vec{e}_{2,\shortparallel}. \tag{2.8}$$

Solving the conservation rules [Eqs. (2.2,2.3,2.7,2.8)] for V, v_x, v_y, v_z leads to the following expression for the postcollisional speed V of the motor in terms of the precollisional speeds:

$$V = V' \tag{2.9}$$

$$+ \frac{2\frac{m}{M}\cos^2\theta}{1+\frac{m}{M}\cos^2\theta}(v'_x\tan\theta\cos\varphi + v'_y\tan\theta\sin\varphi + v'_z - V'). \tag{2.10}$$

2.3.2 Transition probability

The motor is subject to random collisions by gas particles form the different reservoirs i. The particle density and velocity distribution in reservoir i are denoted by ρ_i and $\phi_i(v_x, v_y, v_z)$, respectively. The contribution $dW_i(V|V')$ to the total transition probability $W(V|V')$, coming from collisions on an infinitesimal surface element dS_i of the motor unit in reservoir i, can then be found by considering the number of gas particles that collide with this surface element dS_i in a unit time step:

$$\begin{aligned} dW_i(V|V') = dS_i \int_{-\infty}^{+\infty} dv'_x \int_{-\infty}^{+\infty} dv'_y \int_{-\infty}^{+\infty} dv'_z \\ \times H[(\vec{V'} - \vec{v'}) \cdot \vec{e}_\perp] |(\vec{V'} - \vec{v'}) \cdot \vec{e}_\perp| \rho_i \phi_i(v'_x, v'_y, v'_z) \\ \times \delta\big[V - V' \\ - B(\theta)(\tan\theta\cos\varphi\, v'_x + \tan\theta\sin\varphi\, v'_y + v'_z - V')\big]. \end{aligned} \tag{2.11}$$

Here H represents the Heaviside function, δ the Dirac distribution, and

$$B(\theta) = \frac{2\frac{m}{M}\cos^2\theta}{1+\frac{m}{M}\cos^2\theta}. \tag{2.12}$$

The Dirac delta distribution selects those particles that produce the required postcollisional speed V , following the collision rules [Eq. (2.10)]. Assuming that the velocity distribution of the gas particles is Maxwellian at the reservoir temperature T_i,

$$\phi_i(v_x, v_y, v_z) = \left(\frac{m}{2\pi k_B T_i}\right)^{3/2} \exp\left[-\frac{m(v_x^2 + v_y^2 + v_z^2)}{2k_B T_i}\right], \tag{2.13}$$

the integrals over v_x', v_y', v_z' in Eq. (2.11) can be calculated explicitly. The total transition probability for the motor to change velocity from V' to V in a unit time, is then found by integrating $dW_i(V|V')$ over the surface S_i of each motor part and summing over all the reservoirs i:

$$\begin{aligned} W(V|V') = \frac{1}{4}\sum_i \rho_i \sqrt{\frac{m}{2\pi k_B T_i}} \\ \times \left((V - V')H[V - V'] \int_{S_i, \cos\theta > 0} dS_i \right. \\ \left. + (V' - V)H[V' - V] \int_{S_i, \cos\theta < 0} dS_i \right) \left(\frac{M}{m\cos\theta} + \cos\theta \right)^2 \\ \times \exp\left[-\frac{m}{2k_B T_i} \cos^2\theta \left(V' + \frac{1}{2}(1 + \frac{M}{m\cos^2\theta})(V - V') \right)^2 \right]. \end{aligned} \tag{2.14}$$

We note that in the case of a single reservoir or for multiple reservoirs at the same temperature, the transition probability satisfies the following relation:

$$W(V|V')P^{eq}(V') = W(-V'|-V)P^{eq}(-V), \tag{2.15}$$

with $P^{eq}(V)$ the Maxwell Boltzmann distribution for the speed V of the motor unit (at the temperature of the reservoir(s)). This is in agreement with the general principle of detailed balance in a system at equilibrium [37].

2.4 Solution method

We follow the method of [34, 35, 36] to solve the master equation [Eq. (2.1)] for the moments of the motor velocity,

$$\langle V^n \rangle = \int_{-\infty}^{\infty} P(V,t) V^n dV. \tag{2.16}$$

This method is based on the van Kampen $1/\Omega$ expansion [32].

2.4.1 Solution of the master equation

It is convenient to scale the motor velocity V to a dimensionless variable

$$X = \sqrt{\frac{M}{k_B T_{\text{eff}}}} V, \tag{2.17}$$

with the effective temperature T_{eff} to be determined self-consistently from the condition $\langle X^2 \rangle = 1$ in steady state operation. We can expand the integrand in Eq. (2.1) in a Taylor series about X':

$$\frac{\partial P(X,t)}{\partial t} = \sum_{n=1}^{\infty} \frac{(-1)^n}{n!} \frac{d^n}{dX^n} \{ J_n(X) P(X,t) \}. \tag{2.18}$$

Here the 'jump moments' are given by

$$J_n(X) = \int \Delta X^n W(X; \Delta X) d\Delta X, \tag{2.19}$$

with $W(X'; \Delta X) = W(X|X')$ and $\Delta X = X' - X$. Using Eq. (2.18) a coupled set of equations for the time evolution of the moments $\langle X^n \rangle$ can then be constructed:

$$\frac{\partial \langle X^n \rangle}{\partial t} = \sum_{k=1}^{n} \binom{n}{k} \langle X^{n-k} J_k(X) \rangle, \tag{2.20}$$

with $\binom{n}{k}$ the binomial coefficients.

The exact expression for the jump moments $J_n(X)$ is obtained by integration over ΔX in Eq. (2.19). In terms of parabolic cylinder functions [38],

$$\mathrm{D}_n(z) = \big(\exp[-z^2/4]/\Gamma[-n]\big) \times \int_0^\infty \exp[-zx - x^2/2] x^{-n-1} dx \quad (\text{for } n < 0), \quad (2.21)$$

and the Gamma function (Γ), the result reads:

$$\begin{aligned} J_n(X) =& \frac{2^n}{\sqrt{2\pi}} \Gamma[n+2] \left(\sqrt{\frac{M}{m}}\right)^n \\ & \times \sum_i \rho_i \sqrt{\frac{k_B T_i}{m}} \left(\sqrt{\frac{T_i}{T_{\text{eff}}}}\right)^n \\ & \times \int_{S_i} dS_i \left(\cos\theta + \frac{M}{m}\frac{1}{\cos\theta}\right)^{-n} \\ & \times \exp\left[-\frac{1}{4}\frac{m}{M}\frac{T_{\text{eff}}}{T_i} X^2 \cos^2\theta\right] \\ & \times \mathrm{D}_{-n-2}\left[\frac{1}{2}\sqrt{\frac{m}{M}}\sqrt{\frac{T_{\text{eff}}}{T_i}} X \cos\theta\right]. \end{aligned} \quad (2.22)$$

An exact solution of Eq. (2.20) is not available. We therefore turn to a perturbational approach in terms of the parameter

$$\varepsilon = \sqrt{m/M}. \quad (2.23)$$

This is consistent with the observation that the mass M of the motor is expected to be much larger than the mass m of the gas particles. Even for a motor with dimensions of nanometers operating in a gaseous environment, ε is of order of 10^{-3}.

The expansion of the parabolic cylinder functions is given by

$$\begin{aligned} 2^{-n/2}\Gamma[n+2]\,\mathrm{D}_{-n-2}(z) =& \Gamma[\frac{n+2}{2}] - \sqrt{2}\Gamma[\frac{n+3}{2}]z \\ & + \frac{2n+3}{4}\Gamma[\frac{n+2}{3}]z^2 - \frac{2n+3}{6\sqrt{2}}\Gamma[\frac{n+3}{2}]z^3 \\ & + \frac{4n^2+12n+11}{96}\Gamma[(2+n)/2]z^4 + O(z^5). \end{aligned} \quad (2.24)$$

Table 2.1: The geometric moments σ_2 and σ_3 for some basic three-dimensional shapes. The lowest orders σ_2 and σ_3 ($\sigma_1 = 0$) are tabulated in terms of the total surface area S of the geometry. For illustrations of the shapes and their parameters, see Fig. 2.4.1.

Shape	σ_2/S	σ_3/S	Surface S
Disk	1	0	$2\pi r^2$
Blade	1	0	$2lw$
Sphere	1/3	0	$4\pi r^2$
Cone	$\sin\alpha$	$\sin\alpha(\sin\alpha - 1)$	$\pi r^2(1 + \csc\alpha)$
Pyramid	$\sin\alpha$	$\sin\alpha(\sin\alpha - 1)$	$\frac{1}{4}nr^2 \cot\frac{\pi}{n}\,(1 + \csc\alpha)$
Spherical cap	$\frac{\cos 2\alpha + 5\cos\alpha + 6}{3\cos\alpha + 9}$	$\frac{\sin^4\alpha}{\cos 2\alpha + 4\cos\alpha - 5}$	$\pi r^2(3 + \cos\alpha)/(1 + \cos\alpha)$
Spherical cone	$\frac{3\sin^3\alpha - 2\cos^3\alpha + 2}{3\sin\alpha - 6\cos\alpha + 6}$	$\frac{2\sin^4\alpha + cos^4\alpha - 1}{4\cos\alpha - 2\sin\alpha - 4}$	$\pi r^2 \csc\alpha(1 + 2\tan(\alpha/2))$

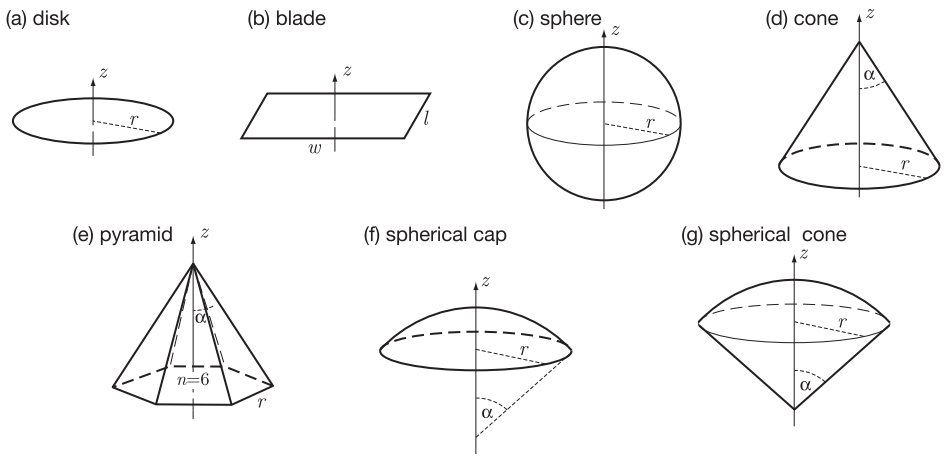

Figure 2.3: Examples of simple three-dimensional geometries that can be treated analytically. The parameters that determine the relative areas of the surfaces are indicated in the illustrations.

Introducing a scaled time $\tau = \varepsilon^2 t$, we find the following expansion for the equation of the first moment:

$$\begin{aligned}\frac{\partial\langle X\rangle}{\partial\tau} = \sum_i \rho_i \sqrt{\frac{k_B T_i}{m}} \Bigg[& \varepsilon^{-1} \sqrt{\frac{T_i}{T_{\text{eff}}}} \sigma_{1,i} - 2\sqrt{\frac{2}{\pi}} \langle X\rangle \sigma_{2,i} \\ & + \varepsilon \left(\sqrt{\frac{T_{\text{eff}}}{T_i}} \langle X^2\rangle - \sqrt{\frac{T_i}{T_{\text{eff}}}} \right) \sigma_{3,i} \\ & + \frac{\varepsilon^2}{3} \sqrt{\frac{2}{\pi}} \left(6\langle X\rangle - \frac{T_{\text{eff}}}{T_i} \langle X^3\rangle \right) \sigma_{4,i} \\ & + \varepsilon^3 \left(\sqrt{\frac{T_i}{T_{\text{eff}}}} - \sqrt{\frac{T_{\text{eff}}}{T_i}} \langle X^2\rangle \right) \sigma_{5,i} \Bigg] + O(\varepsilon^4). \end{aligned} \tag{2.25}$$

The geometry of the motor is contained in the shape factors $\sigma_{n,i}$, defined as:

$$\sigma_{n,i} = \int_{S_i} dS_i \cos^n \theta. \tag{2.26}$$

At this point we remark that the azimuthal angle φ has dropped out, and that the geometric dependency is determined only by the (polar) angle θ between the surface and the direction of movement. Also note that the term in ε^{-1} in Eq. (2.25) is zero by application of Gauss' theorem:

$$\sigma_{1,i} = \int_{S_i} dS_i \cos\theta = \int_{S_i} dS_i \vec{e}_\perp \cdot \vec{e}_z = \int_{V_i} dV_i (\nabla \cdot \vec{e}_z) = 0, \tag{2.27}$$

where the latter integral is over the interior volume V_i of a motor part. This is consistent with the fact that there is no net macroscopic force acting on the motor. The net motion that will be revealed below is the effect of fluctuations only.

Similarly, for the equation of the second moment, one finds the fol-

lowing expansion:

$$\frac{\partial\langle X^2\rangle}{\partial\tau} = \sum_i \rho_i \sqrt{\frac{k_B T_i}{m}} \Bigg[-4\sqrt{\frac{2}{\pi}} \left(-\frac{T_i}{T_{\text{eff}}} + \langle X^2\rangle \right) \sigma_i^2 - 2\varepsilon \left(4\sqrt{\frac{T_i}{T_{\text{eff}}}}\langle X\rangle - \sqrt{\frac{T_{\text{eff}}}{T_i}}\langle X^3\rangle \right) \sigma_i^3 + 2\varepsilon^2 \sqrt{\frac{2}{\pi}} \left(-4\frac{T_i}{T_{\text{eff}}} + 5\langle X^2\rangle - \frac{1}{3}\frac{T_{\text{eff}}}{T_i}\langle X^4\rangle \right) \sigma_i^4 \Bigg] + O(\varepsilon^3). \quad (2.28)$$

2.4.2 Linear relaxation

To order ε^0, Eq. (2.25) reduces to a linear relaxation law $M\partial_t\langle V\rangle = -\gamma\langle V\rangle$ with $\gamma = \sum_i \gamma_i$ the sum of linear friction coefficients γ_i of each part of the object:

$$\gamma_i = 4\rho_i \sqrt{\frac{k_B T_i m}{2\pi}} \sigma_{2,i} = \varrho_i \bar{v}_i \sigma_{2,i}, \quad (2.29)$$

where $\varrho_i = m\rho_i$ is the mass density of the gas, $\bar{v}_i = \sqrt{8k_B T_i/(\pi m)}$ is the mean gas velocity, and $\sigma_{2,i}$ is a geometric factor.

2.4.3 Nonlinearity: Steady state directed motion

If a constant temperature difference between the reservoirs can be maintained for a time longer than the relaxation time M/γ, the probability distribution will relax to its steady state value. Restricting ourselves to the first two moments, we turn to the steady state solution of Eqs. (2.25) and (2.28). First, from Eq. (2.28) we determine the effective temperature T_{eff}, which was defined earlier by the condition $\langle X^2\rangle = 1$. To lowest order, ε^0, we find that T_{eff} is the weighted average of the reservoir temperatures:

$$T_{\text{eff}} = \frac{\sum_i \gamma_i T_i}{\sum_i \gamma_i} = \frac{\sum_i \rho_i \sigma_{2,i} T_i^{3/2}}{\sum_i \rho_i \sigma_{2,i} T_i^{1/2}}. \quad (2.30)$$

Solving Eq. (2.25) to order ε^0 leads to a zero average drift speed $\langle X\rangle = 0$. Rectification of the thermal fluctuations occurs at higher levels

of the expansion and it is necessary to include nonlinear terms. Solving Eq. (2.25) up to order ε gives us an expression to lowest order for the average drift speed of the motor:

$$\begin{aligned}\langle V\rangle &= \sqrt{\frac{m}{M}}\sqrt{\frac{\pi k_B T_{\text{eff}}}{8M}}\frac{\sum_i \rho_i(\frac{T_i}{T_{\text{eff}}}-1)\sigma_{3,i}}{\sum_i \rho_i\sqrt{\frac{T_i}{T_{\text{eff}}}}\sigma_{2,i}} \\ &= \sqrt{\frac{m}{M}}\sqrt{\frac{\pi k_B}{8M}}\frac{\sum_i\sum_j \rho_i\rho_j\sigma_{3,i}\sigma_{2,j}(T_i-T_j)\sqrt{T_j}}{(\sum_i \rho_i\sqrt{T_i}\sigma_{2,i})^2}.\end{aligned} \tag{2.31}$$

2.5 Results and discussion

2.5.1 Friction and diffusion coefficients

Although not directly related to the main topic of this work, we briefly pause to discuss the new result for the linear friction coefficient, given in Eq. (2.29). Together with results from Table 2.1 for the geometric factors σ_2 this result provides the explicit expression for the linear friction coefficient of corresponding basic shapes. The result for a spherical shape with radius r,

$$\gamma = \frac{4}{3}\pi r^2 \varrho_i \bar{v}_i, \tag{2.32}$$

is in agreement with the result found in [39]. In combination with the Einstein relation $D = k_B T/\gamma$, we also obtain the explicit formulas for the corresponding diffusion coefficients D. As an illustration, numerical values are given in Fig. 2.5.1 for various shapes of cross section πr^2, $r =$ 100 nm. To be concrete, we consider highly diluted argon gas (density $10^{19}\,\text{m}^{-3}$) leading to diffusion coefficients of the order of $3\times10^{-4}\,\text{m}^2/\text{s}$, and corresponding friction coefficients of order $1.5\times10^{-17}\,\text{Ns/m}$. As expected, the conical shapes have higher diffusion coefficients and lower friction as one considers smaller opening angles α.

2.5.2 Equilibrium

When the reservoirs are all at the same temperature, $T_i = T$, we find $T_{\text{eff}} = T$, and the distribution of the moments is Gaussian:

$$\langle X\rangle = 0, \langle X^2\rangle = 1, \langle X^3\rangle = 0, \langle X^4\rangle = 3, \ldots \tag{2.33}$$

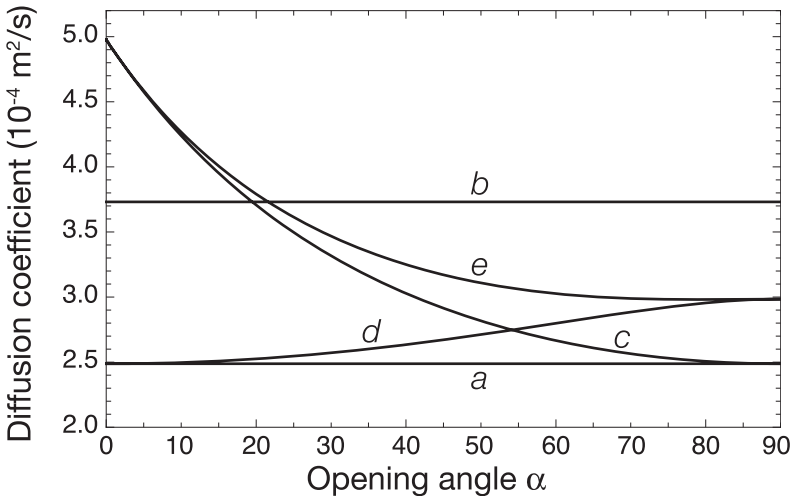

Figure 2.4: Diffusion coefficients of objects with different geometry but identical cross section πr^2 ($r = 100$ nm) in highly diluted argon gas ($10^{19}\,\mathrm{m}^{-3}$ particles, mean free path 2.3 μm) at 299 K temperature. The geometries are (a) a disk, (b) a sphere, (c) a cone, (d) a spherical cap, and (e) a spherical cone. See Fig. 2.4.1 for illustrations. For (c,d,e) the shapes and hence the diffusion coefficients depend on an opening angle α.

The notion that it is impossible to achieve directed motion (or equivalently, to extract work) from a system in thermal equilibrium is confirmed. At least two reservoirs at different temperature are necessary to break detailed balance and make possible the rectification of thermal fluctuations.

2.5.3 Asymmetry

The geometry of the motor units enters into the expression of the average speed via de shape factors σ_2 and σ_3. In table 2.1, we have reproduced these quantities for the objects depicted in Fig. 2.4.1. As is clear from symmetry arguments, the appearance of systematic motion in one direction requires, apart from non-equilibrium conditions, also the breaking of the spatial symmetry in the system. One easily verifies from Eq. (2.26) that

$$\sigma_{n,i} = 0, \quad n \text{ odd}, \tag{2.34}$$

when the surface of a motor element possesses reflection symmetry along the z-axis, the direction of motion. Consistent with this symmetry observation we find that the drift speed of the motor in steady state is indeed zero at lowest order in the perturbation when $\sigma_{3,i} = 0$, cf. Eq. (2.31). It is however interesting to note that reflection symmetry is a sufficient but not a necessary condition for $\sigma_{3,i} = 0$, and hence for obtaining zero sustained motion (at least in this order of the approximation). Consider for example a spherical cone, see Fig. 2.5.3. For a specific opening angle of $\approx 55^\circ$ $\sigma_{3,i}$ becomes zero, even though there is no reflection symmetry. A similar discussion can be applied to higher orders corrections in the ε-expansion (featuring the appearance of the higher shape factors σ_5, σ_7, and so on) indicating that there are special shapes which will have a very low average speed even though there are no immediate symmetry reasons to expect so.

2.5.4 Temperature gradient

For simplicity we limit the discussion of the drift velocity, in particular in relation to the applied temperature gradient, to the case of two reservoirs. Furthermore, the impact of the geometry is most clearly demonstrated

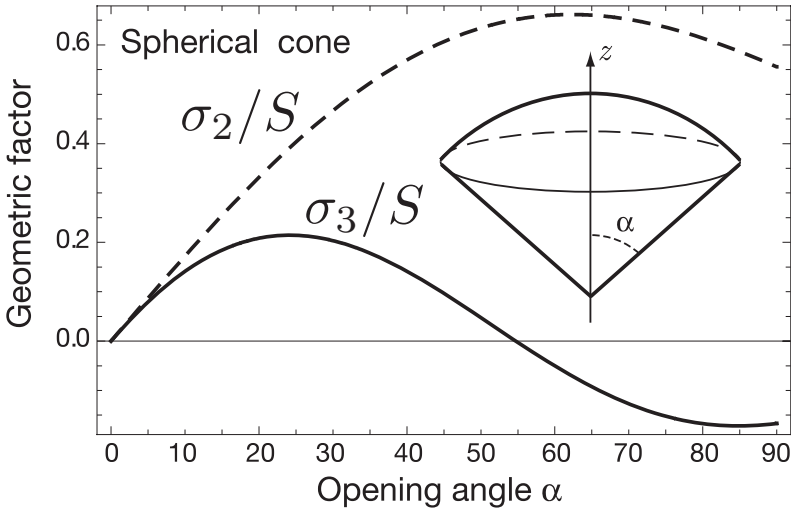

Figure 2.5: The geometric factors σ_2/S and σ_3/S as a function of the opening angle α for a spherical cone, with S the surface area. While σ_2 appears in the expression for the friction coefficient, σ_3 relates to the drift speed of the motor. When the geometry of the surface exhibits symmetry along the z-axis (the direction of movement), σ_3 is zero, and the motor shows no directed motion. The spherical cone is an example of a class of shapes for which σ_3 can become zero, and hence the drift speed (at least to the first approximation), without however showing reflection symmetry. For this particular case, $\sigma_3 = 0$ for $\alpha \approx 55°$.

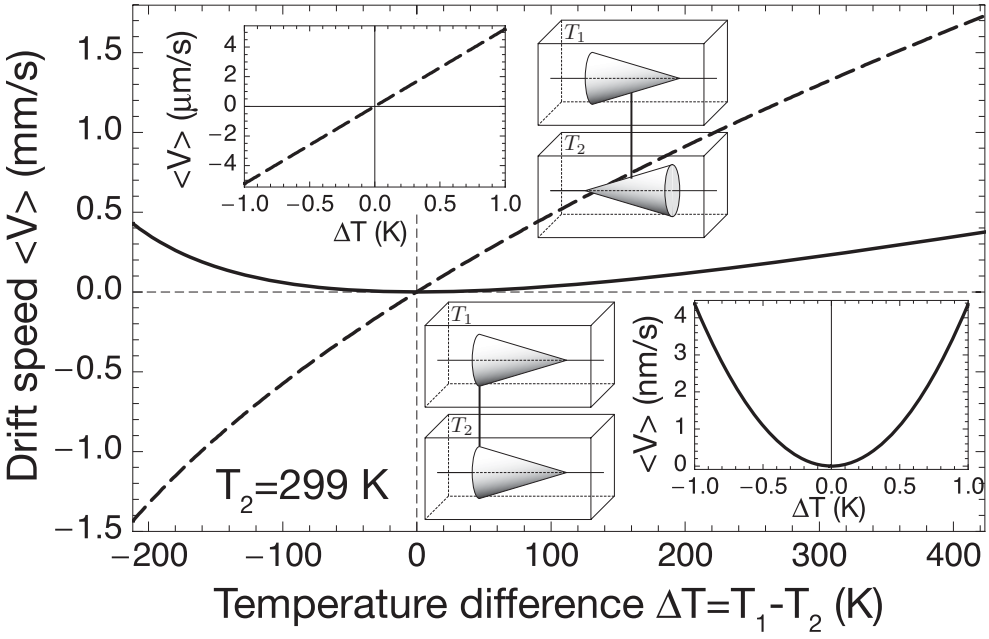

Figure 2.6: The drift speed as a function of the temperature difference $\Delta T = T_1 - T_2$ between the reservoirs for two configurations with identical motor units: parallel (solid curves and lower inset) and antiparallel (dashed curves and upper inset). The units are cone-shaped (opening angle 30°) and the motor mass is 1000 kDa. Both reservoirs are filled with argon gas of same density and T_2 is fixed at 299 K. For small ΔT (see insets), the dependence is parabolic for the parallel setup and linear for the antiparallel setup. The drift speed is of order nm/s (parallel) and μm/s (antiparallel) for $\Delta T \approx 1$ K.

when the motor units have an identical shape in both reservoirs. There are then two possibilities, namely either the units have the same orientation (parallel), or they are pointing in opposite direction (antiparallel), see Fig. 2.5.4 for a schematic representation. For the first scenario, with $\sigma_{2,1} = \sigma_{2,2} = \sigma_2$ and $\sigma_{3,1} = \sigma_{3,2} = \sigma_3$, Eq. (2.31) yields:

$$\langle V \rangle_e = \sqrt{\frac{m}{M}} \sqrt{\frac{\pi k_B}{8M}} \frac{\rho_1 \rho_2 (T_1 - T_2)(\sqrt{T_2} - \sqrt{T_1})}{(\rho_1 \sqrt{T_1} + \rho_2 \sqrt{T_2})^2} \frac{\sigma_3}{\sigma_2}. \tag{2.35}$$

For the second scenario, careful consideration of the sign of $\cos\theta$ in Eq. (2.26) leads us to write $\sigma_{2,1} = \sigma_{2,2} = \sigma_2$ as in the first scenario, but now when $\sigma_{3,1} = \sigma_3$, it follows that $\sigma_{3,2} = -\sigma_3$. The expression for the drift speed thus becomes:

$$\langle V \rangle_o = \sqrt{\frac{m}{M}} \sqrt{\frac{\pi k_B}{8M}} \frac{\rho_1 \rho_2 (T_1 - T_2)(\sqrt{T_1} + \sqrt{T_2})}{(\rho_1 \sqrt{T_1} + \rho_2 \sqrt{T_2})^2} \frac{\sigma_3}{\sigma_2}. \tag{2.36}$$

One striking feature of these results is that the drift velocity is scale-invariant. This is a general property: both σ_2 and σ_3 scale linearly with the total surface S of the motor units. As they appear in the denominator and the nominator respectively in Eqs. (2.35, 2.36), the scale dependence cancels out. This becomes even more apparent for the particular cases presented in Table 2.1, where σ_2/S and σ_3/S are expressed in topological terms. Note that the scale invariance of the drift speed is only valid with respect to the scale of the entire motor. The relative proportions of separate motor units do matter. Note also that scale invariance applies when disregarding the dependence on the mass M. For comparison with a physically realistic situation, we assume a constant density of the motor, so that the drift velocity will decrease with increasing size of an object, through its $1/M$-dependence.

To investigate the departure from the equilibrium state, we consider small deviations of T_1 and T_2 about the average T,

$$T_1 = T + \frac{\Delta T}{2}, \quad T_2 = T - \frac{\Delta T}{2}, \tag{2.37}$$

so that for $\Delta T/T \ll 1$ the drift speeds tend to:

$$\langle V\rangle_e \to -\frac{1}{16}\sqrt{\frac{\pi}{2}}\sqrt{\frac{m}{M}}\frac{\rho_1\rho_2}{(\rho_1+\rho_2)^2}\frac{\sigma_3}{\sigma_2}\sqrt{\frac{k_BT}{M}}\left(\frac{\Delta T}{T}\right)^2, \tag{2.38}$$

$$\langle V\rangle_o \to \frac{1}{4}\sqrt{\frac{\pi}{2}}\sqrt{\frac{m}{M}}\frac{\rho_1\rho_2}{(\rho_1+\rho_2)^2}\frac{\sigma_3}{\sigma_2}\sqrt{\frac{k_BT}{M}}\left(\frac{\Delta T}{T}\right). \tag{2.39}$$

We note that the respective orientation of the motor elements, parallel or antiparallel, plays a crucial role. In the first case the sustained average displacement is always in the same direction (that of $-\sigma_3$), indifferent of the sign of ΔT. This was to be expected because there is an additional symmetry in the system: the interchange of the temperature reservoirs has no effect. From the point of view of irreversible thermodynamics, this situation is special since there is no linear relation between the thermodynamic force (the temperature gradient) and flux (the resulting speed of the motor). For the second case of antiparallel alignment, one observes the usual situation of linear response between thermodynamic force and flux [22, 29, 30]: equilibrium is a point of flux reversal, the direction of net motion reversing with ΔT-inversion.

As an illustration, we reproduce, in table 2.2, explicit values for the drift speed in the case of a single asymmetric unit, namely a cylindrically symmetric cone, positioned in antiparallel alignment in the two reservoirs under physically realistic conditions. The degree of asymmetry is described by a single parameter, the opening angle α. The geometric factors σ_2 and σ_3 are known analytically (see Table 2.1) and we find the following simple expression for the drift speed:

$$\langle V\rangle = \sqrt{\frac{m}{M}}\sqrt{\frac{\pi k_B}{8M}}\frac{\rho_1\rho_2(T_1-T_2)(\sqrt{T_1}+\sqrt{T_2})}{(\rho_1\sqrt{T_1}+\rho_2\sqrt{T_2})^2}(\sin\alpha-1). \tag{2.40}$$

The drift speed will become zero for $\alpha = 90°$, namely when the cone loses its asymmetry and reduces to a flat disk. A natural question is whether there is an optimal opening angle α_o that maximizes the drift speed. For a fixed cross section, one finds $\alpha_o = \sec^{-1}[\sqrt{(1+\sqrt{5})/2}] \approx 38°$. If, on the other hand, one assumes that the mass is kept constant, a maximal speed is reached for an infinitely sharp cone.

Note finally the very strong size-dependence: objects of 20 nm cover their length 5 times per second, for 5 nm size objects this becomes 1200

Table 2.2: Values for the drift speed of the motor, as predicted by theory. Realizations of the motor at different length scales from micrometers to nanometers are presented. The motor units are modeled as silica (SiO_2) cone-shaped objects, located in two reservoirs containing argon gas at temperatures 299.0 K and 299.1 K. For constant motor mass, the speed increases as the opening angle α of the cone decreases.

	$\alpha = 30°$	$\alpha = 5°$	$\alpha = 30°$	$\alpha = 5°$
Motor mass (kDa)	Cylinder base (nm)		Drift speed (μm/s)	
10^{10}	2600	1400	5.2×10^{-8}	9.5×10^{-8}
10^{7}	260	140	5.2×10^{-5}	9.5×10^{-5}
10^{6}	120	55	5.2×10^{-4}	9.5×10^{-4}
10^{5}	63	29	5.2×10^{-3}	9.5×10^{-3}
10^{4}	26	14	0.052	0.095
1000	12	6.3	0.52	0.95
100	5.5	2.9	5.2	9.5
10	2.6	1.4	52	95

times per second. To date few artificial linear molecular motors are fabricated, and comparison with our numerical results is not straightforward. In one rotaxane-based system powered by light [40], a shuttle was moved 1.5 nm with a frequency of 10 kHz (see also [41] for an improvement of this technique). In [42] explicit numerical values for the drift speed of particles in a theoretical flashing ratchet are presented as a function of particles radius. Given an optimized flashing ratchet, a particle of diameter 100 nm can, in principle, drift almost 200 times its own size (19 μm) in every second.

2.6 Conclusion

We have calculated, on the basis of an exact microscopic theory, the properties of a thermal Brownian motor in a three-dimensional setup. When detailed balance is broken by the application of a temperature gradient, a systematic net speed appears, as given in Eq. (2.31). As an example, for a motor consisting of cone-shaped silica units of size 20 nm, one obtains a drift speed of about 0.1 μm/s when subject to 0.1 K temperature difference in a gaseous environment. It remains to be seen whether the predictions of our theoretical analysis (involving various simplifications such as molecular chaos, elastic and normal interactions between gas particles and motor, expansion in mass ratio) provide a realistic estimate, especially for motors operating in a viscous environment.

—3—

Chiral Brownian Heat Pump

Published: M. van den Broek and C. Van den Broeck, Phys. Rev. Lett. **100**, 130601 (2008).

–Abstract–

We present the exact analysis of a chiral Brownian motor and heat pump. Optimization of the construction predicts, for a nanoscale device, frequencies of the order of kHz and cooling rates of the order of femtojoule per second.

Brownian motors have been studied intensively since the early 1990s [22, 20, 21, 43]. This interest coincided with developments in bioengineering and nanotechnology, where understanding and designing a motor in the shape of a small biological or artificial device is an important issue. Most of the motors investigated in this context are powered by chemical energy. Brownian motors driven by a temperature gradient [10, 44, 33] have a fundamental appeal, since their operation is directly related to basic questions such as Carnot efficiency, Maxwell demons and the foundations of statistical mechanics and thermodynamics [12, 45, 46, 30]. The additional significance of the thermal Brownian motor comes from the recent observation that it can operate as a refrigerator [28, 47], see also [48]. In fact, this property is, at least in the regime of linear response, a direct consequence of Onsager symmetry: if a temperature gradient generates motion, an applied force will generate a heat flux. This principle is well known in its application to electro-thermal devices, displaying the Peltier, Seebeck and Thompson effects [49]. At variance however with these macroscopic devices, rectification of nonequilibrium thermal fluctuations provide the driving mechanism for Brownian refrigeration. The latter become more prominent, and so do the resulting motor and cooling functions, as the apparatus becomes smaller.

Previous models for the Brownian refrigerator assume translational motion of the engine [28, 47]. This construction obviously poses difficulties in its technological implementation, while the resulting friction is expected to lower the efficiency. In this letter, we present a chiral rotational model, in which these problems do not occur, and which has the extra benefit that the choice of the axis of rotation provides an additional parameter that can be optimized. A related question, that will also be addressed, is the optimal chiral shape of the device. The observed optimized performance is found to be significantly better than in the translational counterpart.

Since the properties of the Brownian heat pump follow by Onsager symmetry from those of the Brownian motor, we first focus on the latter.

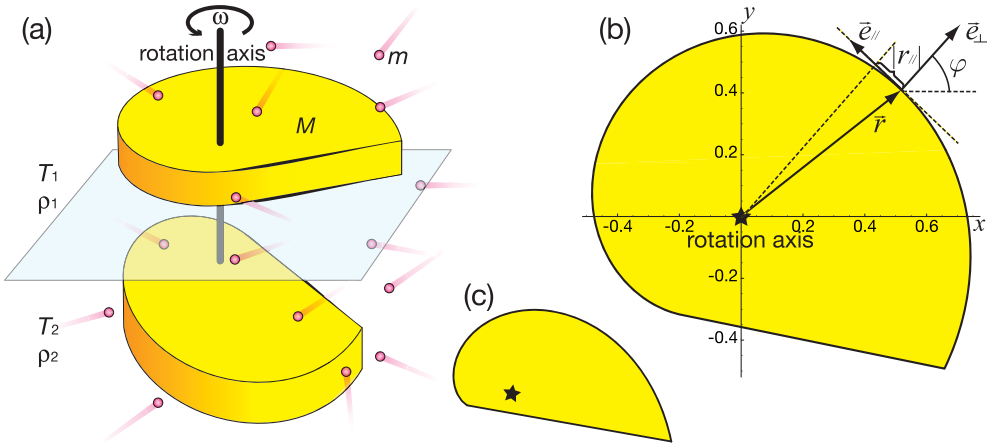

Figure 3.1: (a) Schematic representation of the chiral motor (mass M) rotating as a single unit along the vertical z-axis. Each motor element resides in a separate compartment, filled with gas particles (mass m) at temperatures T_1, T_2 and densities ρ_1, ρ_2, respectively. (b) The planar shape of one motor part is determined by the position vector $\vec{r}(x, y)$ of its perimeter (the origin being the axis of rotation). The collision rule Eq. (3.2) is given in terms of the polar angle φ, determining the direction orthogonal to the perimeter. The properties of the engine are expressed in terms of the tangential component $r_{\shortparallel} = \vec{r} \cdot \vec{e}_{\shortparallel}$ of $\vec{r}$ along the perimeter cf. Eqs. (3.3, 3.5-3.8). Maximal rotation and refrigeration speed is attained for one motor unit being the enantiomorph of the other. The corresponding optimal shape (with unit area) and axis implantation marked by a star, is the spiral form depicted here for maximum frequency (b) and maximum net cooling power (c).

The basic construction is represented in Fig. 3.1(a). The engine consists of two parts linked by a rigid axis (which we take to be the z-axis), around which the whole construction is free to rotate as a single entity. This rotational motion is induced, following Newton's laws, by the collisions with surrounding gas particles. The question of interest is under which conditions sustained rotational motion will arise. Following the Curie principle, the breaking of symmetry plays a crucial role. There are two obvious symmetries involved: the statistical symmetry of the microscopic dynamics and the chiral symmetry of the device. If the motor units are achiral, in the sense that clockwise and counterclockwise rotation cannot be distinguished, no sustained motion will appear. When both motor units reside in a single compartment at equilibrium, sustained rotational motion will not appear, even for chiral motor units, because it would violate the second law of thermodynamics, or referring to the basic underlying symmetry, because detailed balance should hold [37]. Both symmetries will be broken if we consider chiral units residing in separate compartments at unequal temperatures T_i. The index i runs over the different reservoirs, cf. Fig. 3.1(a) for a schematic representation in the case of two reservoirs $i = 1, 2$. As we proceed to show, the resulting average rotational frequency can be calculated exactly from microscopic dynamics, at least in a limiting case. For simplicity, we will restrict the theoretical analysis in this letter to the case of a two-dimensional device. The corresponding results for three-dimensional cylindrical objects, as depicted in Fig. 3.1(a), are obtained by appropriate rescaling with the hight h of the units (for more details, see [50]).

Turning to the exact microscopic analysis, we consider convex (two-dimensional) units, residing in reservoirs that are infinitely large and are filled with dilute gases at equilibrium. The reservoirs play the role of ideal thermostats with which the engine is exchanging energy. In the limit of high dilution and a heavy engine (mass M, moment of inertia I), the collisions of the engine parts with the gas particles (mass m) become uncorrelated events and the following exact Boltzmann master equation for the probability distribution $P_t(\omega)$ of its angular velocity holds:

$$\frac{\partial P_t(\omega)}{\partial t} = \int d\omega' \left[W_{\omega|\omega'} P_t(\omega') - W_{\omega'|\omega} P_t(\omega) \right]. \tag{3.1}$$

Here $W_{\omega|\omega'}$ is the transition probability per unit time for the motor to change its angular velocity from ω' to ω by one collision. We will assume that the collisions are perfectly elastic and that the interaction force is short-ranged and central. Conservation of the total energy and of the total angular momentum in the z-direction of the colliding pair, and of the tangential component of the momentum of the gas particle, leads to the following collision law:

$$\omega = \omega' + \frac{2(\omega' y + v'_x)\cos\varphi - 2(\omega' x - v'_y)\sin\varphi}{x\sin\varphi - y\cos\varphi + \frac{I}{m}\left(x\sin\varphi - y\cos\varphi\right)^{-1}}, \tag{3.2}$$

specifying ω in terms of its pre-collisional value ω' and the pre-collisional speeds $\vec{v'} = (v'_x, v'_y)$ of the gas particle. φ is the polar angle of the surface at impact, see Fig. 3.1(b).

The transition probability $W_{\omega|\omega'}$ can now be calculated following standard arguments from the kinetic theory of gases. Taking into account that the velocity distributions of the particles $\phi_i(\vec{v})$ are Maxwellian at the density ρ_i and temperature T_i of their bath, one finds the following explicit expression:

$$W_{\omega|\omega'} = \tfrac{1}{2\pi}\sum_i \oint dl_i \frac{\rho_i}{v_{T_i}}(r_{\shortparallel} + \frac{I}{m r_{\shortparallel}})^2 |\Delta\omega| H[r_{\shortparallel}\Delta\omega] \\ \times \exp\left[-\left((r_{\shortparallel} + \frac{I}{m r_{\shortparallel}})\Delta\omega + 2r_{\shortparallel}\omega'\right)^2 / \left(\pi v_{T_i}^2\right)\right]. \tag{3.3}$$

The contour integral $\oint dl_i$ is over the perimeter of the engine part in each reservoir, which can be of any convex shape. H represents the Heaviside function and we have introduced the tangential component of the position vector $\vec{r}$ along the perimeter, $r_{\shortparallel} = \vec{r}\cdot\vec{e}_{\shortparallel} = -x\sin\varphi + y\cos\varphi$ cf. Fig. 3.1(b), the thermal speed of the gas particles $v_{T_i} = \sqrt{8kT_i/\pi m}$, and the angular velocity increment $\Delta\omega = \omega - \omega'$.

In equilibrium, $T_i = T$, one easily verifies that the Boltzmann distribution $P^{eq}(\omega) = \sqrt{I/(2\pi kT)}\exp[-I\omega^2/(2kT)]$ is the unique steady state solution of Eq. (3.1). As required by statistical mechanics, this solution satisfies detailed balance: $W_{\omega|\omega'}P^{eq}(\omega') = W_{-\omega'|-\omega}P^{eq}(-\omega)$.

A general solution away from equilibrium is not available, hence we resort to a perturbational technique. For small values of the parameter

$\varepsilon = \sqrt{m/M} = r_0\sqrt{m/I}$, where $r_0 = \sqrt{I/M}$ is the radius of gyration of the device, the change in angular velocity upon collision with a gas particle is small and we can apply a Kramers-Moyal type of expansion. We only present the final results of this procedure, for more details see [50].

Up to third order in ε the average angular speed of the motor obeys the following equation:

$$\frac{\partial\langle\omega\rangle}{\partial t} = \frac{m}{M}\sum_i \rho_i \Bigg[-v_{T_i}\langle\omega\rangle \oint dl_i \left(\frac{r_{\shortparallel}}{r_0}\right)^2 + \varepsilon\left(\sqrt{\frac{I}{m}}\langle\omega^2\rangle - \frac{kT_i}{\sqrt{mI}}\right)\oint dl_i \left(\frac{r_{\shortparallel}}{r_0}\right)^3 + O(\varepsilon^2)\Bigg]. \quad (3.4)$$

To lowest order in ε we recognize a linear drag law, $I\partial_t\langle\omega\rangle = -\gamma\langle\omega\rangle$, featuring a frictional torque which is proportional to the average rotational speed. The proportionality factor $\gamma = \sum_i \gamma_i$ is equal to the sum of the friction coefficients γ_i contributed by each of the engine parts. From Eq. (3.4), one finds the following explicit expression for these friction coefficients:

$$\gamma_i = m\rho_i v_{T_i} \oint dl_i r_{\shortparallel}^2. \quad (3.5)$$

Note that at this order of the perturbation, no systematic steady state motion appears $\langle\omega\rangle^{st} = 0$. This indicates that the "rectification of the fluctuations" leading to systematic motion appears at the level of nonlinear and non-Gaussian effects.

At the next order in ε, the equation for the first moment is coupled to the second moment, whose evaluation is thus needed to close the equation. Restricting ourselves to the steady state, one finds, not surprisingly, that (to lowest order) the average kinetic energy of the motor is given by the usual expression for equipartition, $\frac{1}{2}I\langle\omega^2\rangle = \frac{1}{2}kT_{\text{eff}}$, but at an effective temperature T_{eff}. The latter is found to be equal to the weighted geometric mean of the temperatures in the reservoirs: $T_{\text{eff}} = (\sum_i \gamma_i T_i)/(\sum_i \gamma_i)$.

Combined with Eq. (3.4) we conclude that (up to first order ε), the engine will develop an average steady state angular velocity given by

$$\langle\omega\rangle = \frac{\sum_i \rho_i k(T_{\text{eff}} - T_i)\oint dl_i r_{\shortparallel}^3}{I\sum_i \rho_i v_{T_i}\oint dl_i r_{\shortparallel}^2}. \quad (3.6)$$

Table 3.1: Properties of the 3-d device with a shape optimized for maximum rotational frequency and cooling power, respectively (see Fig. 3.1). Each unit of the device is cylindrical with parallel surfaces of area πR^2, $R = 3\,\mathrm{nm}$, height $h = 3\,\mathrm{nm}$. We assume following values of the parameters: density $1350\,\mathrm{kg/m^3}$ (typical for proteins); total mass $M = 2.29 \times 10^{-22}\,\mathrm{kg}$; mass ratio $m/M = 1.3 \times 10^{-4}$ (m being the mass of a water molecule); $T = 300\,\mathrm{K}$; temperature gradient for the motor: $\Delta T = 0.1\,\mathrm{K}$.

	$\langle\omega\rangle$ (Hz)	γ (10^{-28} Nms)	I ($10^{-39}\,\mathrm{kg\,m^2}$)
Motor	2180	0.90	1.26
Heat pump	1470	4.55	2.22

	$\dot{Q}_{1\to2}/\Gamma$ (10^6 J/(Nms))	Γ_{lim} (10^{-21} Nm)	$\dot{Q}^{\mathrm{max}}_{\mathrm{net}}$ (10^{-15} J/s)
Motor	6.53	1.17	1.92
Heat pump	4.41	4.01	4.42

We proceed to discuss this first central result of our paper. The angular velocity is obviously zero at equilibrium, $T_i = T_{\mathrm{eff}}$, and also when $\oint dl_i r_{\shortparallel}^3 = 0$, in agreement with the fact that the object then loses its chirality. As far as maximizing rotational frequency is concerned, a numerical procedure was employed to identify the optimum configuration (shape plus axis implantation) by deforming the contours in both compartments. This resulted in the spiral shape depicted in Fig. 3.1(b), with one engine part the enantiomorph of the other one. The same shape remains optimal, but appearing as the basis of a cylindrical object as depicted in Fig. 3.1(a), when turning to the case of dimension 3. The dependence of the rotational speed on the shape and axis implantation is very intricate. In fact even the direction of the net rotation is not at all obvious. In Fig. 3.2 we reproduce, for a specific triangular motor element (and its enantiomorph), the lines of equal amplitude for the rotational frequency as a function of the implantation of the rotation axis. The rotation is clockwise/counterclockwise in the dark/light shaded areas respectively. In view of the technological interest of this result, we include the corresponding properties of such engine calculated under physically realistic conditions, in Table 3.1. Rotational frequencies in the kHz regime are

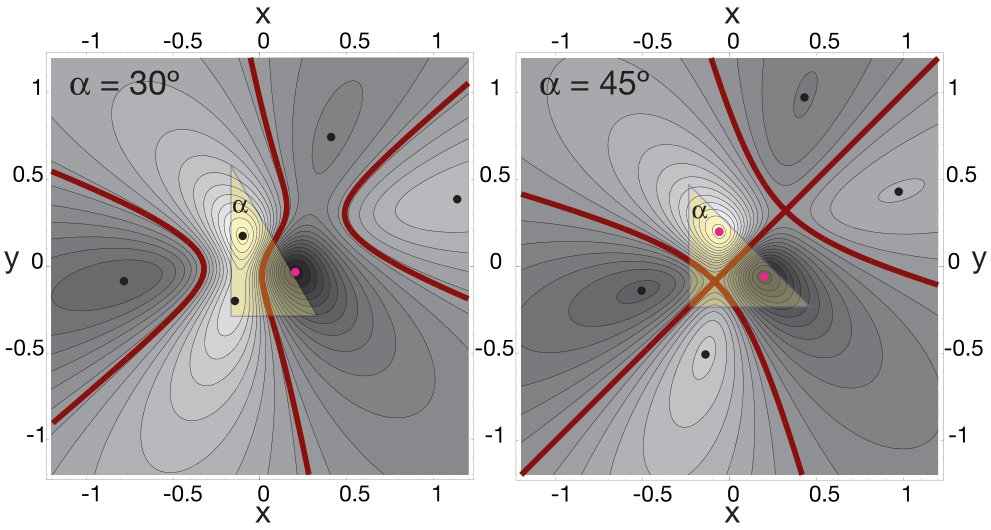

Figure 3.2: Equal-amplitude lines of the rotational frequency $\langle\omega\rangle$ as a function of the location of the rotational axis, for two triangular shapes (apex angle 30° and 45°). The (x, y) coordinates represent the location of the axis with respect to the center of mass of the unit. Thick lines correspond to $\langle\omega\rangle = 0$, and dots to maximum frequency.

obtained for a temperature gradient of .1 K. Such a sustained average rotation will dominate over the thermal Brownian motion, with typical frequency $\sqrt{kT_{\text{eff}}/I} = 1.81 \times 10^9\,\text{Hz}$, on a time scale of seconds or more.

We next turn to the analysis of the heat pump function. In the following, we will focus only on the linear response property, which can directly be obtained by invoking Onsager symmetry. To do so, one needs to write the result Eq. (3.6) in the framework of linear irreversible thermodynamics [49]. One identifies the flux $J_1 = \langle\omega\rangle$ and the thermodynamic force $X_2 = 1/T_2 - 1/T_1$. For a small temperature difference ΔT, $T_1 = T + \Delta T/2$, $T_2 = T - \Delta T/2$, a linear relation between flux J_1 and force $X_2 = \Delta T/T^2$ is observed, namely: $J_1 = L_{12}X_2$. The value of the coefficient L_{12} is found from Eq. (3.6) (for simplicity considering again enantiomorphs):

$$L_{12} = \frac{2kT^2}{Iv_T}\frac{\rho_1\rho_2}{(\rho_1+\rho_2)^2}\frac{\oint dl\, r_{\shortparallel}^3}{\oint dl\, r_{\shortparallel}^2}. \tag{3.7}$$

Following Onsager symmetry [37], there is a mirror relation $J_2 = L_{21}X_1$ with an identical proportionality coefficient $L_{21} = L_{12}$, while J_2 is the flux associated to the temperature gradient X_2, i.e., it is a heat flux $\dot{Q}_{1\to 2}$ (from reservoir 1 to reservoir 2), and X_1 is the thermodynamic force associated with the rotation, namely a mechanical torque divided by the temperature of the system, $X_1 = \Gamma/T$. The relation $J_2 = L_{21}X_1$, with Eq. (3.7), implies that the heat flux $\dot{Q}_{1\to 2}$ is given by

$$\dot{Q}_{1\to 2} = \frac{2kT}{Iv_T}\frac{\rho_1\rho_2}{(\rho_1+\rho_2)^2}\frac{\oint dl\, r_{\shortparallel}^3}{\oint dl\, r_{\shortparallel}^2}\,\Gamma. \tag{3.8}$$

This is the second basic result of this letter. Note that the direction of heat transfer depends on the direction of the torque, in such a way that it activates an opposing Brownian motor in agreement with Le Chatelier's principle [49]. For example, considering $\oint dl\, r_{\shortparallel}^3 > 0$, the motor rotates clockwise $\langle\omega\rangle < 0$ for $\Delta T < 0$ ($T_1 < T_2$). The application of a positive torque $\Gamma > 0$, inducing counterclockwise rotation, produces an energy flux $\dot{Q}_{1\to 2} > 0$, tending to activate the clockwise Brownian motor.

The Onsager coefficients L_{21} and L_{12} are the off-diagonal elements of the 2×2 linear response matrix:

$$\begin{aligned} J_1 &= L_{11}X_1 + L_{12}X_2, & L_{11} &= T/\gamma, \\ J_2 &= L_{21}X_1 + L_{22}X_2, & L_{22} &= \gamma_1\gamma_2 kT^2/(\gamma I). \end{aligned} \tag{3.9}$$

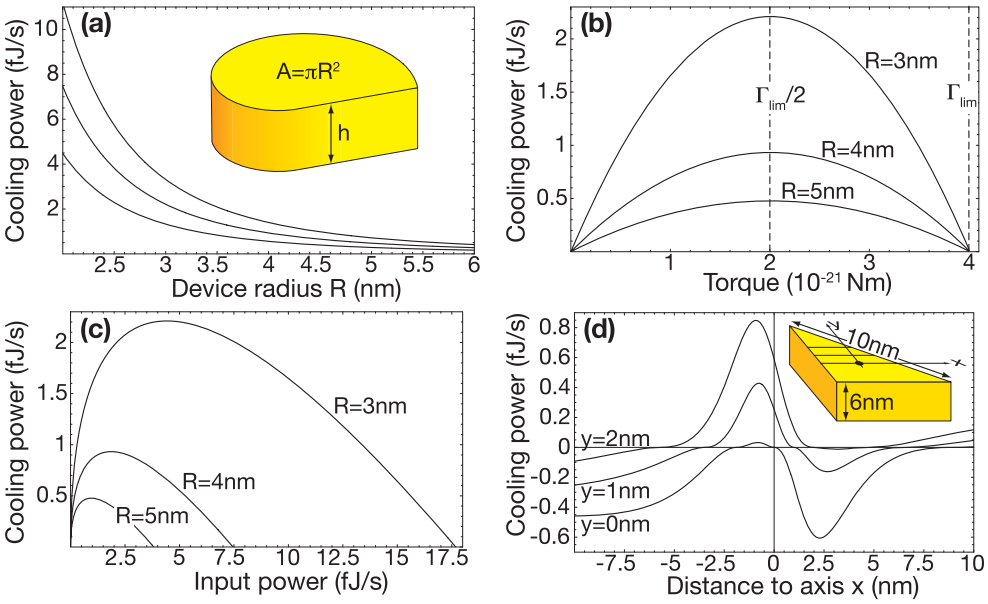

Figure 3.3: The cooling power as a function of (a) the radius of the device for heights $h = 4, 6, 10\,\mathrm{nm}$ (half limiting torque, higher curve corresponds with lower h), (b) the applied torque Γ for height $h = 6\,\mathrm{nm}$ and given radius R, (c) the input power P_{in} for the same dimensions, and (d) the location of the rotation axis with respect to the center of mass. The shape of the device is optimal for (a,b,c), while for (d) it corresponds with the 45° configuration of Fig. 3.2. Other properties as for Table 3.1.

The diagonal elements L_{11}, the rotational mobility, and L_{22}, the thermal conductivity, can again be calculated from the above perturbational method [50], or from general arguments based on Langevin theory [12, 45, 46, 30]. As we proceed to show, these terms, associated with Joule heating and heat conduction, specify the domain in which the heat pump can operate as a cooling device.

An external torque can induce a cooling flux, by pumping heat out of one reservoir (into the other). This effect is offset by a dissipative contribution in both reservoirs, resulting from frictional heating. The linear response term $L_{11}X_1$ expresses that work is performed on the pump upon application of an external torque Γ, which leads to a power input $\Gamma^2\gamma_i/\gamma^2$ in each reservoir i. The Γ^2 dependency ensures that the cooling flux, which is proportional to Γ, will dominate for torques below a certain $\Gamma_{\rm lim}$. For a concrete realization of the device this is shown in Fig. 3.3(b), where the net cooling, $\dot{Q}_{\rm net} = \dot{Q}_{1\to 2} - \Gamma^2\gamma_1/\gamma^2$, is calculated as a function of Γ. The formal condition $|L_{21}X_1| > \Gamma^2\gamma_1/\gamma^2$ enables us to quantify the limiting torque as $\Gamma_{\rm lim} = \gamma^2|L_{12}|/(\gamma_1 T)$, which is remarkably scale-independent. The net cooling $\dot{Q}_{\rm net}$ is maximum for half the limiting torque $\Gamma_{\rm lim}/2$. Under this condition, a device of a few nanometer thickness is capable of a net rate of femtojoules per second, cf. Fig. 3.3(a) and Table 3.1. We also note that under this condition, half of the input power, $P_{\rm in} = \sum_i \Gamma^2\gamma_i/\gamma^2 = \Gamma^2/\gamma$, is used for cooling, yielding a coefficient of performance $\eta = \dot{Q}_{\rm net}/P_{\rm in} = 0.5$. For lower values of the torque, $\Gamma < \Gamma_{\rm lim}/2$, a higher performance η is feasible even though, as explained above, the net cooling flux is no longer maximal [see also Fig. 3.3(c)].

We finally turn to the issue of thermal conductivity. Suppose that a temperature gradient develops under the application of an external torque, cooling one reservoir and heating the other. The heat pump, being in contact with reservoirs of unequal temperature, will then conduct heat against the cooling flow. Eq. (3.9) tells us that this heat flow, $J_2 = L_{22}X_2$, has the form of a Fourier law, $\kappa\Delta T$, with conductivity $\kappa = L_{22}/T^2$. An upper limit for the relative gradient $\Delta T/T$ emerges when the conductive flow $L_{22}X_2$ equals the cooling power $|L_{21}X_1|$. In explicit terms and at maximum performance, $\Gamma = \Gamma_{\rm lim}/2$, the temperature

gradient is bounded by

$$\frac{\Delta T}{T} = \frac{\pi}{8}\frac{m}{I}\frac{\rho_2}{\rho_1+\rho_2}\frac{\left(\oint dl\, r_{\shortparallel}^3\right)^2}{\left(\oint dl\, r_{\shortparallel}^2\right)^2}. \tag{3.10}$$

The fact that this term is proportional with m/M indicates that the device may be better suited to transfer heat than to create a direct temperature difference.

In conclusion, we believe that our study of the chiral molecular device, operating as a heat engine or heat pump, is of potential technological interest. In a nanobiological context, we note that 1 femtojoule per second corresponds to the hydrolysis of 12,000 ATPs per second. It remains to be seen whether the simplifications assumed in this exact theoretical analysis (ideal gas reservoirs, frictionless rotation axis and lowest order approximation in m/M) lead to a realistic estimation of the performance, and whether alternative constructions (non-rigid coupling between units, vibrational instead of rotational units) offer an even better perspective.

—4—

Intrinsic Ratchets

Submitted: M. van den Broek, R. Eichhorn, and C. Van den Broeck, Europhys. Lett. (2008).

–Abstract–

We present a generic formalism to describe Brownian motion of particles with intrinsic asymmetry and give predictions for the drift behavior in unbiased time-dependent force fields. Our findings are supported by molecular dynamics simulations.

4.1 Introduction

In view of their potential applications in bio- and nanotechnology, Brownian motors have in recent years been the object of intensive research [20, 21, 22, 4]. As is well known, the rectification of the thermal motion of Brownian particles involves the breaking of underlying symmetries. On the one hand, the system has to operate under nonequilibrium conditions to break the microscopic equilibrium symmetry of detailed balance. Spatial symmetry on the other hand is usually broken by applying asymmetric external forcing. The two most cited paradigms in this context are the flashing and rocking ratchets (see, *e.g.*, [23]), in which an external space-periodic but space-asymmetric forcing using a ratchet-like potential is applied. Somewhat surprisingly, the case in which an inherent asymmetry of the Brownian particle itself provides the spatial asymmetry has not been discussed in the context of periodic forcing. We will refer to such Brownian motors as intrinsic ratchets. In this letter, we will introduce and solve the equations of motion that generically describe this type of thermal rectification.

4.2 Generic equations of motion

The motion of a Brownian particle (speed v and mass M) is usually described by the following Langevin-Newton equation:

$$M\frac{dv}{dt} = -\gamma v + F + \xi. \tag{4.1}$$

Here γ is the friction coefficient, F is an applied external force and ξ a Gaussian white noise, whose intensity is determined by the fluctuation-dissipation relation. The above equation can be derived from a microscopic description by assuming that the mass of the Brownian particle is

much larger than that of surrounding particles. They form the starting point for deriving the properties of flashing or rocking ratchets. In fact, since one needs to apply spatially asymmetric forcing in these systems, the analysis is typically carried out at the simpler level of overdamped motion. The latter provides a closed description in terms of the position variable only and is known to be a very good approximation in most situations. As we will see below, we however do not need spatially dependent forcing for the rectification in intrinsic ratchets. This greatly simplifies the analysis, even at the underdamped level. Indeed, when the forcing F is position independent, the stochastic variable v is Gaussian, and it suffices to study the equations of motion for the first two moments of the velocity. By choosing as units of time, velocity and force the relaxation time $\tau_r = M/\gamma$, the thermal speed $v_T = \sqrt{k_B T/M}$ and γv_T, the following equations are obtained for the moments $v_1 = \langle v \rangle$ and $v_2 = \langle v^2 \rangle - 1$:

$$\begin{aligned} \frac{dv_1}{dt} &= -v_1 + f, \\ \frac{dv_2}{dt} &= -2v_2 + 2fv_1. \end{aligned} \tag{4.2}$$

We now argue that a minor modification of these equations describes the case of intrinsic ratchets. We first note that the possible asymmetry of the Brownian particle does not appear in the above equations, basically because the relaxation is described by linear response. As a result, the equation for the first moment, which is the central object of interest, is not coupled to the second moment. The asymmetry of the particle will appear at a next order of perturbation, at the level of nonlinear relaxation. Furthermore, the resulting correction appearing in the equation for v_1 still has to vanish when operating under equilibrium conditions, *i.e.*, when $v_2 = 0$. The simplest analytical correction is thus a term of the form αv_2, where the constant α quantifies the strength of the asymmetry. Since this term acts like a perturbation on the first moment we can dismiss, to lowest order, the correction that will appear in the equation for v_2. The intrinsic ratchet is thus described at lowest order (with α effectively playing the role of a small dimensionless parameter) by the

following generic set of equations:

$$\begin{aligned} \frac{dv_1}{dt} &= -v_1 + \alpha v_2 + f, \\ \frac{dv_2}{dt} &= -2v_2 + 2fv_1. \end{aligned} \tag{4.3}$$

In addition to the above handwaving arguments, we note that the equations of motion given in Eq. (4.3) can be derived from microscopic theory of a Brownian particle moving in a bath of an ideal gas, by an expansion in the ratio of the mass of the gas particles (m) over the mass of the Brownian particle (M) [33, 35, 51]. Such a derivation also provides explicit expressions for the open parameters α and γ (or τ_r) behind Eq. (4.3) in terms of microscopic quantities. Concrete examples for the cases of translational and rotational motion of an asymmetric object suspended in a thermalized gas will be given below.

In the remainder of this letter, we focus on the rectification, *i.e.*, the appearance of a non-zero average drift velocity, when the particle is subjected to an unbiased time-periodic force $f(t)$. This scenario is the analogue of the rocking ratchet for particles with intrinsic asymmetry.

4.3 Piecewise constant forcing

Eq. (4.3) with time-periodic forcing $f(t)$ has a mathematical structure similar to the Newton equation of motion for a parametric oscillator. It is therefore out of the question to find a general analytical solution. Instead we turn to the case of piecewise constant forcing (square wave profile), *viz.*,

$$\begin{aligned} 0 \leq t < \tau/2: &\quad f(t) = f_0, \\ t \leq \tau/2 < \tau: &\quad f(t) = -f_0. \end{aligned} \tag{4.4}$$

Introducing the vector notation

$$V(t) = \begin{bmatrix} v_1 \\ v_2 \end{bmatrix}(t), \tag{4.5}$$

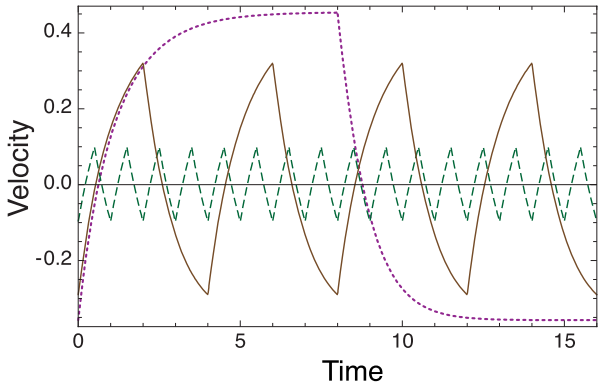

Figure 4.1: Time evolution of the first moment of the velocity v_1 (in thermal speed v_T units) subject to a modulating square force with periods 1, 4, and 16 (dashed, solid, dotted curve). The relaxation time τ_r of the particle is the time unit. The particle's asymmetry is $\alpha = 0.3$ and force amplitude is $f_0 = 0.4$ (in units Mv_T/τ_r, with M the particle's mass).

one readily finds the solutions in the separate time regimes, with $f = f_0$ and $f = -f_0$ respectively:

$$V_+(t) = A_+(t)C_+ + B_+, \tag{4.6}$$
$$V_-(t) = A_-(t)C_- + B_-. \tag{4.7}$$

The time-propagators $A_\pm$ are given by:

$$A_\pm(t) = \begin{bmatrix} \pm\frac{1-d_\pm}{4f_0}e^{-(3+d_\pm)t/2} & \pm\frac{1+d_\pm}{4f_0}e^{-(3-d_\pm)t/2} \\ e^{-(3+d_\pm)t/2} & e^{-(3-d_\pm)t/2} \end{bmatrix}, \tag{4.8}$$

with $d_\pm = \sqrt{1 \pm 8\alpha f_0}$. $B_\pm$ are the steady state solutions:

$$B_\pm = \begin{bmatrix} \pm f_0/(1 \mp \alpha f_0) \\ f_0^2/(1 \mp \alpha f_0) \end{bmatrix}. \tag{4.9}$$

The vector constants $C_\pm$ are specified by the assumption that we operate in the steady state regime, hence the velocity moments in Eqs.

(4.6) and (4.7) satisfy time-periodic boundary conditions, $V_+(0) = V_-(\tau)$. This, together with continuity at $t = \tau/2$, $V_+(\tau/2) = V_-(\tau/2)$, leads to a solution,

$$C_+ = (A_2^{-1}A_1 - A_4^{-1}A_3)^{-1}(A_2^{-1} - A_4^{-1})(B_- - B_+), \tag{4.10}$$
$$C_- = (A_1^{-1}A_2 - A_3^{-1}A_4)^{-1}(A_1^{-1} - A_3^{-1})(B_+ - B_-), \tag{4.11}$$

with $A_1 = A_+(\tau/2), A_2 = A_-(\tau/2), A_3 = A_+(0), A_4 = A_-(\tau)$. We will not reproduce here the resulting expression for the time-dependent average speed v_1. It is extremely cumbersome, and, strictly speaking, only valid to lowest order in the asymmetry contribution α. For an illustration of the typical time dependence of v_1 we refer to Fig. 4.3. We remark that our theory yields accurate results when $\alpha f_0 \ll 1$. Under the described ratchet operation, the speed v_1 and second moment v_2 are then of order f_0 and f_0^2 respectively. This means that the nonlinear correction term αv_2 in the equations of motion [Eq. (4.3)] is a factor αf_0 smaller than the linear v_1 term.

The quantity of central interest is the resulting time-average net speed, being the average net displacement over a period τ divided by this period:

$$v_{\text{net}} = \tau^{-1} \int_0^\tau v_1(t)\, dt. \tag{4.12}$$

Again, the exact expression for v_{net} is extremely long. In any case, our approach is limited to small α, so it suffices to reproduce the lowest order term in α:

$$v_{\text{net}} \simeq \alpha f_0^2 \left(1 - \frac{4}{\tau} \tanh \frac{\tau}{4}\right). \tag{4.13}$$

We note that the next term in the expansion in α is an order of magnitude $(\alpha f_0)^2$ smaller.

We make the following observations. First, there is no directed motion, $v_{\text{net}} = 0$, in the absence of forcing, $f_0 = 0$, or when the particle has intrinsic symmetry, $\alpha = 0$. Second, v_{net} is an uneven function of α, hence an inversion of the asymmetry, $\alpha \to -\alpha$, results in an inversion of the speed of net motion. We represent v_{net} as a function of the asymmetry, α, the amplitude of the force, f_0, and the period, τ, in Fig. 4.3 (solid curves). In all three cases, the lowest order approximation, Eq. (4.13), is in fact indistinguishable from the exact result for the chosen range of

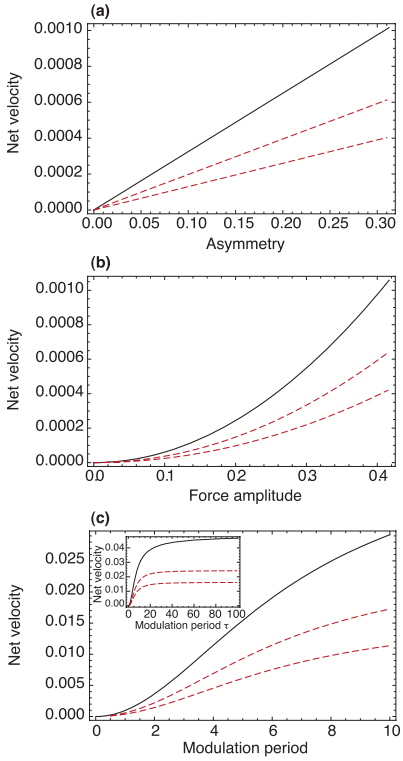

Figure 4.2: Time-average net velocity v_{net} as a function of **(a)** the asymmetry α of the Brownian particle, **(b)** the amplitude f_0 of the modulating force, and **(c)** the modulation period τ. Exact analytical solutions for square modulation – solid curves – coincide, for the presented parameter range, with the first order approximation [Eq. (4.13)]. Dashed curves represent results for harmonic modulation (upper curves) and sawtooth modulation (lower curves), Eqs. (4.21) and (4.23), obtained from first order perturbation theory. Numerical integration results can not be distinguished from the analytical solutions in the shown graphs. If not in the abscissa, parameter values are $\alpha = 0.3$, $f_0 = 0.4$, $\tau = 1$. Units for velocity, time and force are the particle's thermal speed v_T, relaxation time τ_r and Mv_T/τ_r (mass M) respectively; α is dimensionless.

values of α and f_0. Finally we note that the maximum speed $v_{\rm net}^{\rm lim} \simeq \alpha f_0^2$ is reached in the limit of very slow modulation, $\tau \to \infty$. Since this speed is expressed in units of thermal velocity, we conclude that one can reach high net drift speeds, comparable to thermal speeds, by applying unbiased periodic forcing of small to moderate intensity to intrinsic ratchets.

4.4 Other periodic forcings

To investigate the effect of other types of periodic forcing, such as harmonic or symmetric sawtooth [*cf.* Fig. 4.4(b)], we resort to a perturbational solution of Eq. (4.3). As the contribution due to the intrinsic asymmetry α is considered small, we can make the following first-order ansatz for the velocity moments:

$$v_1 = v_{1,0} + \alpha v_{1,1}\,, \tag{4.14}$$

$$v_2 = v_{2,0} + \alpha v_{2,1}\,. \tag{4.15}$$

With this ansatz, Eq. (4.3) can be solved to first order in α for arbitrary periodic force fields $f(t)$, yielding the steady state solutions

$$v_{1,0}(t) = \int_{-\infty}^{t} dt'\, e^{-(t-t')} f(t')\,, \tag{4.16}$$

$$v_{2,0}(t) = \int_{-\infty}^{t} dt'\, e^{-2(t-t')} 2 f(t') v_{1,0}(t')\,, \tag{4.17}$$

$$v_{1,1}(t) = \int_{-\infty}^{t} dt'\, e^{-(t-t')} v_{2,0}(t')\,, \tag{4.18}$$

$$v_{2,1}(t) = \int_{-\infty}^{t} dt'\, e^{-2(t-t')} 2 f(t') v_{1,1}(t')\,. \tag{4.19}$$

Using $f(t+\tau) = f(t)$ it is easy to show that these expressions are indeed periodic with periodicity τ. The results for the time evolution of the first moment v_1 under harmonic or sawtooth forcing are reproduced in Fig. 4.4(a); they are indistinguishable from numerically integrated solutions of the original Eq. (4.3). For comparison, the results for the square wave profile are also included.

With regard to the net velocity $v_{\rm net}$ as defined in Eq. (4.12), we observe that for unbiased symmetric forcings $f(t+\tau/2) = -f(t)$, and thus $\int_0^\tau dt'\, v_{1,0}(t') = 0$ [see Eq. (4.16)], so that $v_{\rm net}$ is given by

$$v_{\rm net} = \alpha\tau^{-1} \int_0^\tau {\rm d}t'\, v_{1,1}(t')\,. \tag{4.20}$$

Again, $v_{\rm net}$ is zero when $\alpha = 0$, consistent with the notion that no directed motion occurs for symmetrical particles.

It is straightforward to recover the net velocity for square forcing to lowest order in α, Eq. (4.13), from (4.20). Similarly, for harmonic driving, $f(t) = f_0 \sin(2\pi t/\tau)$, we find a time-average net velocity

$$v_{\rm net} = \frac{\alpha f_0^2}{2} \frac{\tau^2}{4\pi^2+\tau^2}\,. \tag{4.21}$$

For sawtooth forcing,

$$\begin{aligned} 0 \le t < \tau/2: &\quad f(t) = f_0\,(t-\tau/4)/(\tau/4)\,, \\ t \le \tau/2 < \tau: &\quad f(t) = f_0\,(3\tau/4-t)/(\tau/4)\,, \end{aligned} \tag{4.22}$$

a net speed

$$v_{\rm net} = \frac{\alpha f_0^2}{3}\left[1 - 3\left(\frac{4}{\tau}\right)^2 + 3\left(\frac{4}{\tau}\right)^3 \tanh\frac{\tau}{4}\right] \tag{4.23}$$

is obtained. These first order results for the net velocity $v_{\rm net}$ are compared with the analytical solution for square forcing in Fig. 4.3 (dashed curves). We conclude that the resulting drift behavior is very similar in all three cases. In fact, comparing Eqs. (4.13), (4.21) and (4.23), we see that the differences become very small, and even vanish for slow forcing $\tau \to \infty$, if, instead of using the same amplitude for the three modulations, one considers the same average quadratic amplitude, *i.e.*, if one replaces $f_0/\sqrt{2} \to f_0$ in Eq. (4.21) and $f_0/\sqrt{3} \to f_0$ in Eq. (4.23).

4.5 Microscopic models

As already mentioned, the structure of Eq. (4.3) can be obtained from kinetic theory of microscopic models, that describe a small, non-trivially

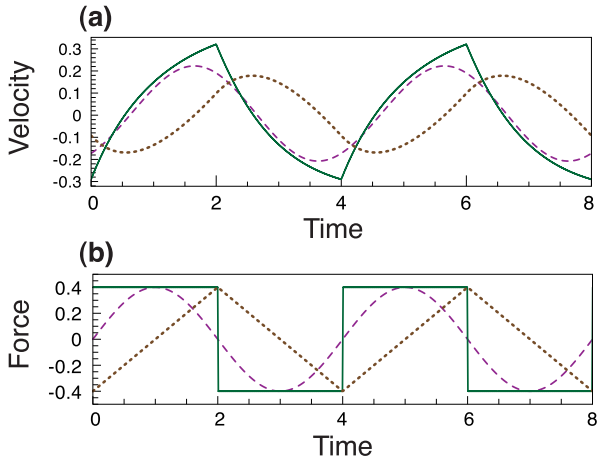

Figure 4.3: Time evolution of **(a)** the first moment of the velocity v_1 (in thermal speed v_T units) for the periodic forcings in **(b)** (correspondence by line style). For harmonic and symmetric sawtooth profiles the first order approximation [Eq. (4.14)] is used, for square modulation the full analytical solution is shown. In all three cases, a numerical solution of the dynamic equation is indistinguishable from the analytical results in the graph. Parameter values are period $\tau = 4$, force amplitude $f_0 = 0.4$ and asymmetry $\alpha = 0.3$. Unit of time is the particle's relaxation time τ_r, unit of force is Mv_T/τ_r, with M the particle's mass.

shaped object (mass M) moving under the influence of collisions with a surrounding bath of gas particles (mass m), by an expansion in the mass ratio $\varepsilon = \sqrt{m/M}$ [33, 35, 51]. Such a procedure also provides explicit expressions for the parameters τ_r and α of the intrinsic ratchet.

For a three-dimensional asymmetric object of arbitrary convex shape, that is confined to move along a fixed z-axis (translational motion), one obtains [51]

$$\tau_r = \varepsilon^{-2}\sigma_2^{-1}, \tag{4.24}$$

$$\alpha = \sqrt{\pi/8}\,\varepsilon^3\tau_r\sigma_3, \tag{4.25}$$

where the geometry dependent moments σ_n are given by

$$\sigma_n = \rho\sqrt{\frac{8k_BT}{\pi m}}\int_{\mathrm{S}} dS\,(-\vec{e}_\perp|_z)^n\,, \tag{4.26}$$

with ρ being the particle density of the gas, and where the integral is over the surface of the asymmetric object. $\vec{e}_\perp|_z$ is the component in the free direction of motion (z) of the outward unit normal vector $\vec{e}_\perp$ at its surface.

To get an idea of the actual net velocity a realistic setup of an intrinsic ratchet can attain, we use Eqs. (4.13), (4.24)-(4.26) to calculate the speed for a cone-shaped silica (SiO_2) Brownian particle with half opening angle 30° and 10 nm base diameter [see Fig. 4.5(a) for a schematic representation]. The cone's axis is along the free direction of motion. In air, the ratio M/m is about 10 000 and the asymmetry parameter is $\alpha = 0.003$. At temperature $T = 300\,\mathrm{K}$ the relaxation time is $\tau_r = 7.5\,\mathrm{ns}$. An amplitude $f_0 = 10$ of unbiased square forcing then corresponds to 1.9 pN in real units and is well within the accuracy range of our theory: $\alpha f_0 = 0.03$. These conditions produce a maximum speed of $v_{\mathrm{net}}^{\mathrm{lim}} = 0.88\,\mathrm{m/s}$ or 30% of the thermal speed of the particle. Note that the direction of the particle's motion is towards the apex of the cone.

4.6 Rotational Brownian motion

For simplicity of presentation, we started with the generic equations of motion for one-dimensional translational Brownian motion of an asymmetric particle. In practice, this supposes that the particle is constrained

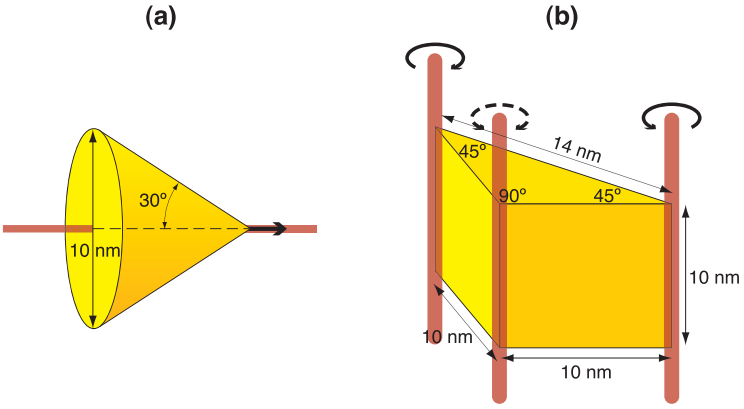

Figure 4.4: Idealized realizations of the intrinsic ratchet. **(a)** For translational motion: a conical shape with axis along the free direction of motion. Indicated is the resulting sense of net motion under unbiased forcing. **(b)** For rotational motion: a right triangular prism, with three suggested locations for the rotation axis. The resulting net rotation sense under unbiased forcing is indicated.

to move on a track. The so-far presented discussion of the intrinsic ratchet can however be repeated, with minor modifications, for the *rotational* Brownian motion of chiral objects, with angular velocity ω and moment of inertia I. With an adaptation of the expressions for the relaxation time $\tau_r = I/\gamma$ and the thermal velocity $v_T = \sqrt{k_B T/I}$ as units of time and angular velocity, and f now signifying a torque, this leads to the same generic equations of motion [Eq. (4.3)] for the moments $v_1 = \langle\omega\rangle$ and $v_2 = \langle\omega^2\rangle - 1$. Microscopic theory [31, 50] yields the same expressions for the relaxation time τ_r [Eq. (4.24)] and asymmetry coefficient [Eq. (4.25)], but now with geometrical moments given by

$$\sigma_n = \rho\sqrt{\frac{8k_BT}{\pi m}}\int_{\mathrm{S}} dS\,[(\vec{e}_\perp \times \vec{e}_r)|_z]^n \ , \tag{4.27}$$

where the axis of rotation is taken to be parallel to the z-axis. Again, the integral is over the surface of the object and $\vec{e}_\perp$ is the outward unit normal vector on the surface. $\vec{e}_r$ is given by $\vec{r}/r_0$, with $\vec{r}$ denoting the position of a surface element measured from the axis of rotation (the z-component in $\vec{r}$ is irrelevant), and $r_0 = \sqrt{I/M}$ being the radius of gyration of the object. Due to the chosen orientation of the rotation axis, only the z-component of $\vec{e}_\perp \times \vec{e}_r$ appears in the expression for σ_n. With these new notations and units, the previous results, in particular the expressions for the time-average net velocity [Eqs. (4.13), (4.21), (4.23)], remain valid.

In view of the technological potential of the rotational setup, and in order to get an idea of the order of magnitudes involved, we again consider a realistic physical realization. A silica triangular prism of height 10 nm and with right triangular top and bottom surfaces (sides: 10 nm, 10 nm, 14 nm) is connected with a rotation axis at one of its vertical edges, *cf.* Fig. 4.5(b). Operating in air, the ratio M/m is about 23 000. If the axis is connected to the 90° corner edge, $\alpha = 0$ and no rectification or net rotation will occur. Connected to the 45° corner edges, $\alpha = \pm 0.0016$ and relaxation time is $\tau_r = 8.1$ ns, at air temperature $T = 300$ K. A torque amplitude (for square forcing) of $f_0 = 10$ corresponds to 2.2×10^{-20} Nm and produces a maximum net rotation frequency of 6 MHz, 16% of the thermal frequency.

4.7 Molecular dynamics simulations

In the following we verify our generic theory for the intrinsic ratchet with molecular dynamics simulations. As concrete microscopic system, we consider the prism from Fig. 4.5(b) surrounded by a thermalized bath of ideal gas particles, and perform event-driven simulations of its rotational Brownian motion. The rotation axis is chosen to be located slightly [4 nm in the units of Fig. 4.5(b)] outside the prism in the plane given by one of the prism surfaces merging at the 90° edge, and is oriented parallel to this edge.

Exploiting the homogeneity of the prism along the direction of the rotation axis, the simulations are carried out in a (projected) two-dimensional space, where the ratchet object is given by the right triangular top (or bottom) surface of the prism, and where the rotation axis is reduced to a point-like center of rotation. The rotation center is positioned at the center of a quadratic box, containing an ideal gas of point particles (mass m). The box walls 'absorb' gas particles upon collision, but also randomly 'emit' new particles (into the box' interior) such that the gas properties, in particular density ρ and Maxwellian equilibrium distribution, are preserved. In this way, an infinitely large reservoir of gas particles is realized.

Collisions between gas particles and the triangle are detected by numerically solving the exact equations of motion for the point in time of the impact. At each collision, the speed of the gas particle and the rotational velocity of the triangle are changed according to the rules for elastic collisions, neglecting tangential forces [31]. In between collisions the triangle is accelerated by an external constant or periodically switching torque (square profile).

In Fig. 4.7 the net rotational speed of the triangle under the action of a periodically switching torque is shown for different values of the modulation period τ. The agreement between simulation results for the time-average net velocity v_{net} and theory, Eq. (4.13), is excellent. We also compared the asymptotic rotation of the triangle under constant but opposite torques ('infinite' driving period τ) with the theoretical result, Eq. (4.9), and again found excellent agreement.

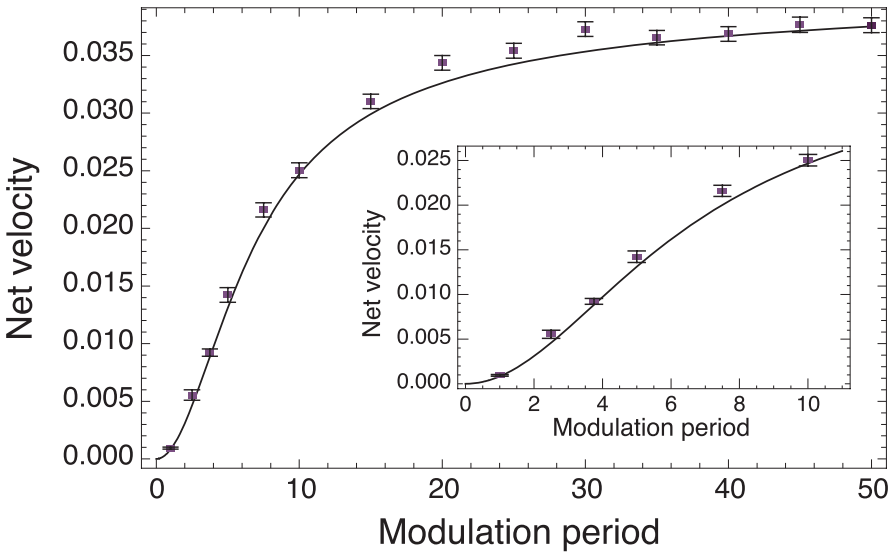

Figure 4.5: Molecular dynamics simulation results (dots with error bars) compared with theory (curves) for the rotational intrinsic ratchet. Time-average net velocity v_{net} is shown as a function of the modulation period τ of zero-average square forcing. The simulation results are obtained from averaging over typically 5000 realizations (20 000 for the smallest driving periods) with about 17 000 collisions performed per realization, corresponding to a simulation time of 1000 periods for the fastest and 20 periods for the slowest modulation; the error bars characterize the remaining statistical uncertainty. Simulation parameters are $\rho = 0.25$, $M = 50$, $m = 1$, side lengths $(1, 1, \sqrt{2})$ of the right triangle, and amplitude 0.15 of the external square torque (see also main text), resulting in $\alpha = 0.0233$ and $f_0 = 1.32$. Units are relaxation time τ_r (time), thermal angular velocity $v_T = \sqrt{k_B T/I}$ (angular velocity) and $I v_T/\tau_r$ (torque), with I the inertial moment.

4.8 Stop-and-go motor

We finally discuss an alternative approach to intrinsic ratchets, anticipated in [52] and further worked out in more detail in [53]. The so-called stop-and-go motor consists of an asymmetric particle which is periodically stopped, for example by an array of traps or binding sites that can be activated or deactivated at will. The basic assumption is that the (thermal) energy of the Brownian particle is changed when it is subjected to the trapping mechanism. This energy exchange results in a specific value of the second velocity moment at the stopping sites, $v_{2,s}$. For $v_{2,s} \neq 0$ the energy exchange in the traps induces a deviation from thermal equilibrium conditions, and this process will result in sustained directed motion with an average net speed $v_{\rm net}$, being the average distance traveled by the particle in a time interval τ_s between the stopping events, divided by τ_s. A simple analytical calculation, starting from Eq. (4.3) with $f = 0$, gives an exact expression:

$$v_{\rm net} = \frac{\alpha v_{2,s}}{2\tau_s} \left(1 - e^{-\tau_s}\right)^2 . \tag{4.28}$$

The sense of motion is determined by the sign of α and of $v_{2,s}$, which is negative (positive) when the particle's thermal motion is reduced (enhanced) by the trapping mechanism. A stopping interval $\tau_s^o \simeq 1.26$, given by the solution of $e^{\tau_s} = 2\tau_s + 1$, yields a maximum net velocity ($v_{\rm net}^{\rm max} \simeq 0.204\,\alpha v_{2,s}$) and an optimal distance between binding sites ($\simeq 0.256\,\alpha v_{2,s}$, expressed in units $v_T \tau_r$).

These theoretical predictions are confirmed in a molecular dynamics simulation of the stop-and-go mechanism applied to a rotating (chiral) object, using the setup based on the prism in Fig. 4.5(b), as in the previous section. In Fig. 4.8 the resulting average net velocity $v_{\rm net}$ as a function of different stop intervals τ_s, for the values $v_{2,s} = -1$ and 1 is shown. In the insets of Fig. 4.8 we include the molecular dynamics results for $v_{\rm net}$ at the optimal stopping interval as a function of $v_{2,s}$. The linear relation ($v_{\rm net}^{\rm max} \simeq 0.204\,\alpha v_{2,s}$) holds, even for large $v_{2,s}$.

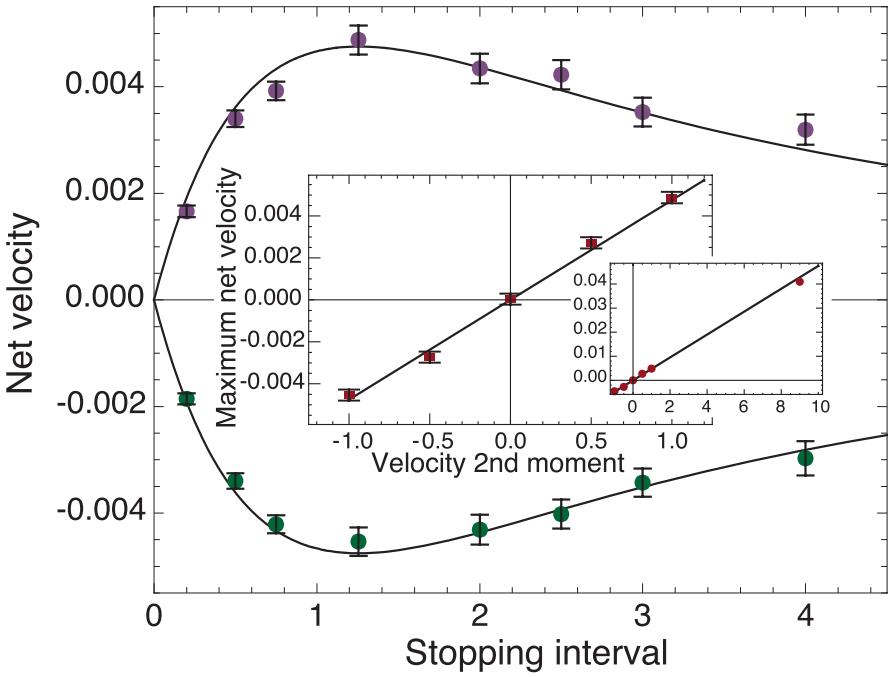

Figure 4.6: Main figure: average (angular) net velocity v_{net} of the rotating stop-and-go ratchet as a function of the time interval τ_s between stopping events. In the trapping mechanism the second moment is set to $v_{2,s} = 1$ (upper curve), $v_{2,s} = -1$ (lower curve), with $v_2 = \langle \omega^2 \rangle - 1$. Insets: maximal average net velocity v_{net} (for optimal τ_s) as a function of the second moment of the velocity $v_{2,s}$ in the trap. Lines correspond to theory, dots represent results from molecular dynamics simulations, using the same setup as for Fig. 4.7 (but without external torque). The net speed is obtained from simulating 1000 independent stopping intervals τ_s per realization and averaging over 10 000 realizations for the three smallest stopping intervals and over 5000 realizations otherwise. Shown angular velocity is in units of thermal speed $v_T = \sqrt{k_B T/I}$ and time in units of relaxation time τ_r. The asymmetry parameter is $\alpha = 0.0233$.

4.9 Conclusion

Intrinsic ratchets are characterized by an inherent asymmetry of the Brownian particle itself breaking the spatial symmetry. A generic formalism for the dynamical behavior enables us to quantify the net particle velocity under unbiased periodic forcing. Molecular dynamics simulations of a rotational setup confirm the validity of this formalism. We predict drift speeds comparable to thermal speeds for nanosized asymmetric Brownian particles under ratchet operation. The relative simplicity of the setup (one heat bath, external symmetric forcing) could open avenues to experimentally test the nonlinear contribution of intrinsic asymmetry crucial in this and other work [33, 35, 51, 31, 50, 52, 53, 54, 55, 56].

—5—

Chiral Brownian rotor and heat pump: theory and verification with molecular dynamics simulations

Excerpts to be submitted: M. van den Broek, R. Eichhorn, J. Liesenborgs, and C. Van den Broeck, Phys. Rev. E.

–Abstract–

We derive in detail the theory of the chiral Brownian rotor and heat pump introduced in Chapter 3 and compare the results with molecular dynamics simulations.

5.1 Brownian motors

The Brownian motors suggested in Chapter 2 move linearly, which obviously poses difficulties when comparing with real systems, or suggesting a technological implementation of a Brownian motor. In Chapter 3 (see also [31]) we introduced a Brownian motor, driven by thermal fluctuations, that is free to rotate around a fixed axis. Rotational motion typically encounters less friction than purely translational movement and a rotating force is easier to apply than a linear force. We propose a device that exploits the random nature of the perturbations from its environment maximally to produce a net directed motion.

Molecular motors operating within biological cells, although chemically driven, are also subject to random motion. F_1-ATPase is a well-known rotating motor (see Fig. 5.1 for a diagram). A direct observation of its rotation, driven by the hydrolysis of adenosine triphosphate (ATP), was first reported in [2, 3]. Later experiments [57] revealed the direction in which the ATP motor spins. It is about 10 nm in size and typically rotates with a frequency of 100 Hz. The observed rotary torque reaches more than 40 pN nm. The relation between the geometry of our rotating object, specifically its chirality, and its kinetic properties, such as the average motion and friction, can be of interest to microbiology. One might also imagine artificial devices inspired by the existing biological examples. Proteins could be used as the building blocks of mechanical devices and artificial biological membranes as means to separate reservoirs and keep them at different temperature. Small moving parts in the area of micro-electronics are also subject to random fluctuations.

As a side note we remark that the rotational three-dimensional model we will present, can be used to describe the essence of the device R. Feynman presented in his Lectures on Physics [11] [for a sketch of the ratchet and pawl mechanism, see Fig. 5.2(a)] to illustrate the impos-

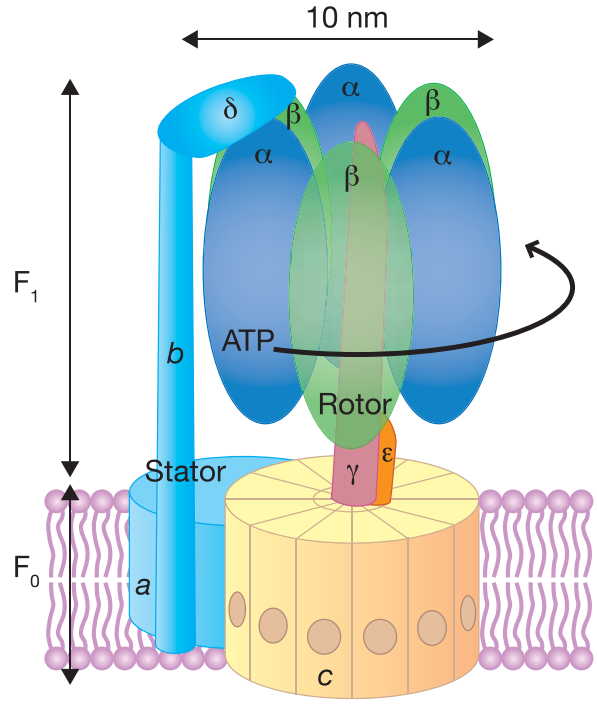

Figure 5.1: F_1-ATPase is a naturally occurring rotating molecular motor. It works as a pump for ions through a membrane. Its driving force is chemical, through the hydrolysis of ATP. Our interest in this molecular motor lies in its environment (in the cytoplasm, subject to fluctuations), its construction (rotational, and through a biological membrane), its physical characteristics (size of the order of 10 nm) and dynamical properties (rotational frequency of the order of 100 Hz).

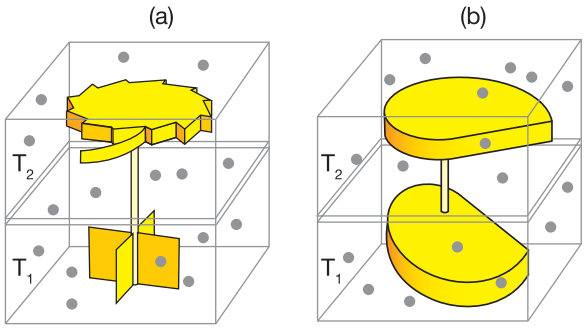

Figure 5.2: (a) The ratchet and pawl mechanism used by R. Feynman to illustrate the impossibility to extract work from a system in equilibrium. An axle with vanes in it (in the bottom reservoir) is bombarded by gas molecules at temperature T_1. The pawl in the top reservoir (surrounded by a gas at temperature T_2) *seems* to allow only one rotation sense of the ratchet, that is connected with the axle. The fluctuations of the paddle in the bottom reservoir *would* then be rectified. Via a comparison of the probability to move forward and backward, Feynman showed in his Lectures on Physics [11] that at temperature equilibrium, $T_1 = T_2$, no average motion occurs and the device cannot be used to do work, such as to lift a weight. For $T_1 > T_2$ however, average motion does take place and the ratchet works as an engine. Feynman noted that for $T_1 < T_2$, the ratchet goes backward. Note that the rectification manifested by the device originates from the asymmetry of the ratchet and pawl mechanism. Our model remains close to Feynman's system, as it can be applied to rotating three-dimensional objects of any shape, while it simplifies the asymmetry requirements to the geometrical properties of the device. (b) A rotating Brownian motor where two parts in isolated thermal reservoirs (temperatures T_1 and T_2, particle densities ρ_1 and ρ_2) are connected through the axis of rotation. Collisions with particles in the reservoirs will cause fluctuating rotational movement of the heavier motor, which, under appropriate conditions, will propel the motor with a nonzero average angular velocity.

sibility of a Maxwell Demon, that would be able to extract work from a system in equilibrium. It was also shown that the same device can lift a weight (do work) at temperature disequilibrium.

These reasons motivate us to study a chiral Brownian motor in detail. The constituting parts of the motor are in different thermal reservoirs. In an analytical analysis we will derive expressions for the kinetic properties of the motor as a function of the external parameters of the system. It will be made clear that temperature equilibrium between the different reservoirs results in zero average motion and hence prohibits the creation of a Maxwell Demon. On the other hand we will demonstrate the importance of the configuration of the building blocks of the motor and their actual shape, as well as their position relative to the rotation axis. Some emphasis is put on finding optimum operation, yielding maximum average angular velocity. The chiral Brownian motor presented now is a precursor for the chiral Brownian refrigerator presented later in this text. The exact relationship derived here between the angular velocity and the temperature gradient will be a crucial step in the investigation of the cooling potential.

The concrete model we propose consists of at least two parts, each residing in a thermal reservoir $i = 1, 2, \ldots$, that are rigidly connected with each other through a rotation axis. In Fig. 5.2(b) we show the construction of two parts in reservoirs of temperature T_1 and T_2, and particle densities ρ_1 and ρ_2. We expect that the fluctuations from collisions with particles in the thermal reservoirs will under certain conditions be rectified, resulting in an average rotational motion, clockwise or counterclockwise. As we will demonstrate, these conditions are (1) thermal disequilibrium, $T_1 \neq T_2$, and (2) asymmetry (or chirality) through the shape of the motor parts.

5.2 From fluctuations to the angular velocity

Our analysis is based on an exact calculation of the probability for the motor to change its rotating speed by a certain amount when subject to thermal fluctuations. We will show that an exact solution can be reached when the fluctuations are in the form of collisions of particles of

an ideal gas at temperature equilibrium with the surface of the motor. A master equation for the probability density to observe an angular velocity $P(\omega, t)$ at a certain time t can be proposed if the particles are presumed to collide not more than once, and only with the motor. This condition implies that the gas is in the high Knudsen number regime. Limiting the parts of the motor to convex and closed shapes will reduce but not prohibit recollisions in the case of rotational motion. The justification for neglecting recollisions ultimately rests on a comparison with molecular dynamics simulations, of which the results are given at the end of this text. We are interested in the case where the motor, with total mass M, has no translational degree of freedom and a single rotational degree of freedom. Parts of the motor reside in different thermal reservoirs but are considered rigidly linked. Choosing the z-axis as the axis of rotation, we can write for the angular velocity $\vec{\omega} = (0, 0, \omega)$. The inertial moment I_z of the motor with respect to the rotation axis is simply denoted as I.

Under these conditions the probability density $P(\omega, t)$ obeys a master equation,

$$\partial_t P(\omega, t) = \int d\omega' \left[W(\omega|\omega') P(\omega', t) - W(\omega'|\omega) P(\omega, t) \right], \tag{5.1}$$

where $W(\omega|\omega')$ is the transition probability per unit time for the motor to change its angular velocity from ω' to ω. The solution is based on the van Kampen $1/\Omega$-method [32]. A Taylor expansion of the first term of the integrand in the angular velocity change, $\upsilon = \omega - \omega'$, leads to

$$\partial_t P(\omega, t) = \sum_{n=1}^{\infty} \frac{(-1)^n}{n!} \left(\frac{d}{d\omega} \right)^n \{ a_n(\omega) P(\omega, t) \}. \tag{5.2}$$

In this expression the so-called *jump moments* appear, given by

$$a_n(\omega) = \int \upsilon^n W(\omega; \upsilon) d\upsilon. \tag{5.3}$$

A notation $W(\omega'; \upsilon) = W(\omega|\omega')$ is used. With the time evolution of the probability density known [(Eq. (5.2)], it is possible to derive a coupled set of equations for the moments of the angular velocity $\langle \omega^n \rangle$:

$$\partial_t \langle \omega^n \rangle = \sum_{k=1}^{n} \binom{n}{k} \langle \omega^{n-k} a_k(\omega) \rangle, \tag{5.4}$$

with $\binom{n}{k}$ the binomial coefficients. Our strategy is now clear: first find an expression for the transition probability $W(\omega|\omega')$, then calculate the jump moments $a_n(\omega)$, and finally the moments of the angular velocity $\langle\omega^n\rangle$.

However, the coupled set of equations Eq. (5.4) cannot be solved unless we expand each equation into powers of a small variable, and ignore terms after a certain order. For the expansion variable we will use $\varepsilon = r_0\sqrt{m/I}$, with $r_0 = \sqrt{I/M}$ the radius of gyration of the motor. We also introduce an effective temperature T_{eff}, so that to first significant order, in the regime of stationary motion, the average kinetic energy of the motor is given by

$$\frac{1}{2}I\langle\omega^2\rangle = \frac{1}{2}k_B T_{\text{eff}}. \tag{5.5}$$

In the calculation it is convenient to make a transformation to dimensionless variables, by scaling the angular velocity ω and the jump moments a_n as follows:

$$\begin{aligned} \xi &= \omega\sqrt{I/k_B T_{\text{eff}}}, \\ A_n(\xi) &= (\sqrt{I/k_B T_{\text{eff}}})^n a_n(\xi). \end{aligned} \tag{5.6}$$

Our selfconsistent definition of the effective temperature T_{eff} then leads to $\langle\xi^2\rangle = 1$ for the stationary state to first order in ε. The set of coupled equations for the moments $\langle\xi^n\rangle = \int \xi^n P(\xi,t)d\xi$ remains

$$\partial_t\langle\xi^n\rangle = \sum_{k=1}^{n}\binom{n}{k}\langle\xi^{n-k}A_k(\xi)\rangle. \tag{5.7}$$

5.3 Two-dimensional model of the motor

The motor consists of parts with hard surfaces of arbitrary (but convex) shape, each described by their boundary and inner mass distribution. Many of the important features already appear in a simpler two-dimensional system, which we present first. Here the motor consists of two-dimensional shapes, each in two-dimensional reservoirs. We choose a cartesian coordinate system as follows: the z-axis coincides with the rotation axis, while the xy-plane is parallel to the reservoirs. In each reservoir i, the shape of the motor (part) is defined by its boundary $\vec{r}_i(x,y)$, given

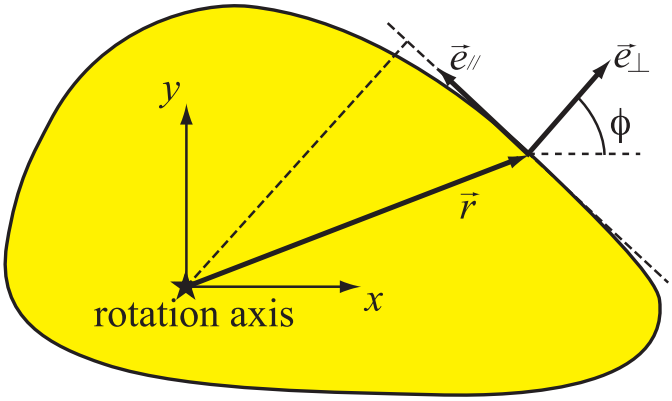

Figure 5.3: The coordinate system used for the two-dimensional model. In each reservoir, the motor part can be described by the boundary $\vec{r}(x, y)$, where the rotation axis is at the origin of the reference frame. It is convenient to also know explicitly the orientation of the boundary at any point. This is given by the polar angle φ of the normal outward vector $\vec{e}_{\perp}$ on the surface at this point. The unit vector $\vec{e}_{\shortparallel}$ is tangential to the boundary.

as a vector with the rotation axis as its origin (see Fig. 5.3). The perimeter of the boundary is denoted L_i. Henceforth we will just write $\vec{r}(x, y)$ for $\vec{r}_i(x, y)$ as no confusion can arise in subsequent expressions. It is convenient in the further derivation to explicitly know the inclination of the boundary at $\vec{r}(x, y)$, for which we use the orientation of the normal outward unit vector $\vec{e}_{\perp} = (\cos\varphi, \sin\varphi)$ on the boundary, determined by the polar coordinate φ from the x-axis.

5.3.1 Conservation rules

Fluctuations of the angular velocity ω of the motor arise from collisions on the surface with gas particles of mass m. Such a collision – presumed instantaneous and perfectly elastic – changes the velocity of the gas particle $\vec{v}' = (v'_x, v'_y)$ into $\vec{v} = (v_x, v_y)$ after the collision, while the motor changes angular speed from ω' to ω. The inertial moment of the mo-

tor about the rotation axis (z-axis) is denoted I, while its mass is M. Conservation of the total energy requires that

$$\frac{1}{2}I\omega'^2 + \frac{1}{2}m{v'_x}^2 + \frac{1}{2}m{v'_y}^2 = \frac{1}{2}I\omega^2 + \frac{1}{2}mv_x^2 + \frac{1}{2}mv_y^2, \tag{5.8a}$$

while conservation of the angular momentum in the z-direction yields

$$m(xv'_y - yv'_x) + I\omega' = m(xv_y - yv_x) + I\omega. \tag{5.8b}$$

Also we suppose the interaction force is short-ranged and central, implying that the tangent component of the momentum of the gas particle on the boundary is conserved. Choosing the tangent unit vector $\vec{e}_{\shortparallel} = (-\sin\varphi, \cos\varphi)$, so that $(\vec{e}_{\perp}, \vec{e}_{\shortparallel})$ forms a positive orthonormal base, we write

$$\vec{v'} \cdot \vec{e}_{\shortparallel} = \vec{v} \cdot \vec{e}_{\shortparallel}. \tag{5.8c}$$

The conservation laws [Eqs. (5.8)] produce a solution for the postcollisional angular velocity ω,

$$\omega = \omega' + \frac{2(\omega' y + v'_x)\cos\varphi - 2(\omega' x - v'_y)\sin\varphi}{x\sin\varphi - y\cos\varphi + \frac{I}{m}\left(x\sin\varphi - y\cos\varphi\right)^{-1}}, \tag{5.9}$$

Introducing

$$r_{\shortparallel} = \vec{r} \cdot \vec{e}_{\shortparallel} = -x\sin\varphi + y\cos\varphi, \tag{5.10}$$

and the precollisional speed of the boundary at position $\vec{r}$,

$$\vec{V'} = \vec{\omega'} \times \vec{r} = (-\omega' y, \omega' x), \tag{5.11}$$

so that we can write

$$V'_{\perp} = \vec{V'} \cdot \vec{e}_{\perp} = -\omega' y\cos\varphi + \omega' x\sin\varphi, \tag{5.12}$$

and

$$\Delta V'_{\perp} = (\vec{V'} - \vec{v'}) \cdot \vec{e}_{\perp} = -(\omega' y + v'_x)\cos\varphi + (\omega' x - v'_y)\sin\varphi, \tag{5.13}$$

the transition in ω can also be written as

$$\omega = \omega' + 2\frac{\Delta V'_{\perp}}{r_{\shortparallel} + \frac{I}{mr_{\shortparallel}}}. \tag{5.14}$$

5.3.2 Transition probability

Next, we set out to find the crucial transition probability $W(\omega|\omega')$ for the motor to change its angular velocity from ω' to ω in a unit of time. Every reservoir i contains a gas with particle density ρ_i and velocity distribution ϕ_i. The contribution dW_i to the total transition probability $W(\omega|\omega')$ from all possible collisions of particles in gas i in a time interval dt on a boundary section of length dl_i, at position $\vec{r}(x,y)$ and with orientation φ, can be expressed as

$$\begin{aligned} dW_i(\omega|\omega') = dl_i \int_{-\infty}^{+\infty} dv'_x \int_{-\infty}^{+\infty} dv'_y \\ \times H[(\vec{V'} - \vec{v'}) \cdot \vec{e}_\perp] |(\vec{V'} - \vec{v'}) \cdot \vec{e}_\perp| \rho_i \phi_i(v'_x, v'_y) \\ \times \delta \left[\omega - \omega' - \frac{2(\omega' y + v'_x)\cos\varphi - 2(\omega' x - v'_y)\sin\varphi}{x\sin\varphi - y\cos\varphi + \frac{I}{m}\left(x\sin\varphi - y\cos\varphi\right)^{-1}} \right], \end{aligned} \tag{5.15}$$

with H the Heaviside step function and δ Dirac's distribution. We multiplied the particle density ρ_i with the volume of the gas that is passed by the boundary element dl_i in a time unit, considering only those gas particles that comply with the collision rules. This can be written in short form as

$$\begin{aligned} dW_i(\omega|\omega') = dl_i \int_{-\infty}^{+\infty} dv'_x \int_{-\infty}^{+\infty} dv'_y H[\Delta V'_\perp] |\Delta V'_\perp| \\ \times \rho_i \phi_i(v'_x, v'_y) \delta \left[\omega - \omega' - 2\frac{\Delta V'_\perp}{r_{_{\shortparallel}} + \frac{I}{m r_{_{\shortparallel}}}} \right]. \end{aligned} \tag{5.16}$$

The *total* transition probability is then found by integrating over all boundary elements dl_i and summing over all reservoirs:

$$W(\omega|\omega') = \sum_i \oint_{\text{boundary}} dW_i(\omega|\omega'). \tag{5.17}$$

Henceforth we will simply write $\oint$ when we imply the line integral over all boundary elements.

For a Maxwellian velocity distribution at temperature T_i,

$$\phi_i(v_x, v_y) = \frac{m}{2\pi k_B T_i} \exp\left(\frac{-m(v_x^2 + v_y^2)}{2k_B T_i} \right), \tag{5.18}$$

the integrals over the speed of the colliding particles can be performed explicitly, resulting in

$$W(\omega|\omega') = \frac{1}{4}\sum_i \oint dl_i \rho_i \sqrt{\frac{m}{2\pi k_B T_i}} \times (r_{\shortparallel} + \frac{I}{m r_{\shortparallel}})^2 H[(\omega-\omega')r_{\shortparallel}]|\omega-\omega'| \times \exp\left[-\frac{m}{2k_BT_i}\left((r_{\shortparallel}+\frac{I}{mr_{\shortparallel}})\frac{\omega'-\omega}{2} - r_{\shortparallel}\omega'\right)^2\right]. \quad (5.19)$$

5.3.3 Moments of the angular velocity

Now that we have obtained an exact expression for the transition probability $W(\omega|\omega')$, we turn our attention to the jump moments,

$$a_n(\omega) = \int \upsilon^n W(\omega;\upsilon) d\upsilon, \quad (5.20)$$

and then the moments of the angular velocity. Careful consideration of the sign of $r_{\shortparallel} + I/mr_{\shortparallel}$ in

$$W(\omega;\upsilon) = \frac{1}{4}\sum_i \rho_i \sqrt{\frac{m}{2\pi k_B T_i}} \times \left(H[\upsilon]\int_{r_{\shortparallel}\geq 0} dl_i + H[-\upsilon]\int_{r_{\shortparallel}<0} dl_i\right)|\upsilon|(r_{\shortparallel}+\frac{I}{mr_{\shortparallel}})^2 \times \exp\left[-\frac{m}{2k_BT_i}\left((r_{\shortparallel}+\frac{I}{mr_{\shortparallel}})\frac{\upsilon}{2} + r_{\shortparallel}\omega\right)^2\right], \quad (5.21)$$

where $\upsilon = \omega - \omega'$ is the change in angular velocity, leads to an exact expression for the jump moments. In terms of parabolic cylinder functions, $\mathrm{D}_n(z) = (\exp[-z^2/4]/\Gamma[-n])\int_0^\infty \exp[-zx - x^2/2]x^{-n-1}dx$ (for $n<0$) the results are

$$a_n(\omega) = \frac{2^n}{\sqrt{2\pi}}\Gamma[n+2]\sum_i \rho_i \left(\frac{m}{k_BT_i}\right)^{-\frac{n+1}{2}} \oint dl_i \left(r_{\shortparallel}+\frac{I}{mr_{\shortparallel}}\right)^{-n} \times \exp\left[-\frac{m}{4k_BT_i}r_{\shortparallel}^2\omega^2\right] \mathrm{D}_{-n-2}\left[\sqrt{\frac{m}{4k_BT_i}}r_{\shortparallel}\omega\right]. \quad (5.22)$$

Rescaling the jump moments using dimensionless variables $\xi = \omega\sqrt{I/k_B T_{\text{eff}}}$ allows us to introduce the parameter $\varepsilon = r_0\sqrt{m/I}$, where $r_0^2 = I/M$:

$$A_n(\xi) = \frac{2^n}{\sqrt{2\pi}}\Gamma[n+2]\sum_i \rho_i \sqrt{\frac{k_B T_i}{m}}\left(\frac{T_i}{T_{\text{eff}}}\right)^{n/2}\oint dl_i \left(\frac{\varepsilon r_{\shortparallel}/r_0}{1+\varepsilon^2\left(r_{\shortparallel}/r_0\right)^2}\right)^n \times \exp\left[-\frac{1}{4}\varepsilon^2\frac{T_{\text{eff}}}{T_i}\left(\frac{r_{\shortparallel}}{r_0}\right)^2\xi^2\right] \mathrm{D}_{-n-2}\left[\varepsilon\sqrt{\frac{T_{\text{eff}}}{T_i}}\frac{r_{\shortparallel}}{r_0}\xi\right]. \quad (5.23)$$

We can express both the exponential function and the parabolic cylinder functions in a power series,

$$\exp[z] = 1 + \frac{z}{1!} + \frac{z^2}{2!} + \frac{z^3}{3!} + \cdots, \quad (5.24)$$

$$2^{-n/2}\Gamma[n+2]\,\mathrm{D}_{-n-2}(z) = \Gamma[\frac{n+2}{2}] - \sqrt{2}\Gamma[\frac{n+3}{2}]z + \frac{2n+3}{4}\Gamma[\frac{n+2}{3}]z^2 - \frac{2n+3}{6\sqrt{2}}\Gamma[\frac{n+3}{2}]z^3 + \frac{4n^2+12n+11}{96}\Gamma[(2+n)/2]z^4 + O(z^5). \quad (5.25)$$

Considering that the parameter $\varepsilon = \sqrt{m/M}$ is small for gas particles much lighter than the motor, we arrive at a series expansion for the jump moments in ε. We substitute this expansion in the set of equations [(Eq. (5.23)] coupling the jump moments $A_n(\xi)$ with the moments of the

angular velocity $\langle \xi^n \rangle$. For $n = 1$, with $\tau = \varepsilon^2 t$, this results in

$$\begin{aligned}
\partial_\tau \langle \xi \rangle = \varepsilon^{-2} \langle A_1(\xi) \rangle = \sum_i \rho_i \sqrt{\frac{k_B T_i}{m}} \\
\times \Bigg[\varepsilon^{-1} \sqrt{\frac{T_i}{T_{\text{eff}}}} \oint dl_i \left(\frac{r_{\shortparallel}}{r_0} \right) - 2\sqrt{\frac{2}{\pi}} \langle \xi \rangle \oint dl_i \left(\frac{r_{\shortparallel}}{r_0} \right)^2 \\
+ \varepsilon \left(\sqrt{\frac{T_{\text{eff}}}{T_i}} \langle \xi^2 \rangle - \sqrt{\frac{T_i}{T_{\text{eff}}}} \right) \oint dl_i \left(\frac{r_{\shortparallel}}{r_0} \right)^3 \\
+ \frac{\varepsilon^2}{3} \sqrt{\frac{2}{\pi}} \left(6\langle \xi \rangle - \frac{T_{\text{eff}}}{T_i} \langle \xi^3 \rangle \right) \oint dl_i \left(\frac{r_{\shortparallel}}{r_0} \right)^4 \\
+ \varepsilon^3 \left(\sqrt{\frac{T_i}{T_{\text{eff}}}} - \sqrt{\frac{T_{\text{eff}}}{T_i}} \langle \xi^2 \rangle \right) \oint dl_i \left(\frac{r_{\shortparallel}}{r_0} \right)^5 \Bigg] + O(\varepsilon^4). \qquad (5.26)
\end{aligned}$$

The term in ε^{-1} disappears because

$$\oint dl_i r_{\shortparallel} = \oint \vec{dl}_i \cdot \vec{r} = \int_{A_i} (\nabla \times \vec{r}) \cdot \vec{e_z} dA_i = 0. \qquad (5.27)$$

Similarly for $n = 2$,

$$\begin{aligned}
\partial_\tau \langle \xi^2 \rangle = \sum_i \rho_i \sqrt{\frac{k_B T_i}{m}} \\
\times \Bigg[-4\sqrt{\frac{2}{\pi}} \left(-\frac{T_i}{T_{\text{eff}}} + \langle \xi^2 \rangle \right) \oint dl_i \left(\frac{r_{\shortparallel}}{r_0} \right)^2 \\
-2\varepsilon \left(4\sqrt{\frac{T_i}{T_{\text{eff}}}} \langle \xi \rangle - \sqrt{\frac{T_{\text{eff}}}{T_i}} \langle \xi^3 \rangle \right) \oint dl_i \left(\frac{r_{\shortparallel}}{r_0} \right)^3 \\
+2\varepsilon^2 \sqrt{\frac{2}{\pi}} \left(-4\frac{T_i}{T_{\text{eff}}} + 5\langle \xi^2 \rangle - \frac{1}{3} \frac{T_{\text{eff}}}{T_i} \langle \xi^4 \rangle \right) \oint dl_i \left(\frac{r_{\shortparallel}}{r_0} \right)^4 \\
+2\varepsilon^3 \left(7\sqrt{\frac{T_i}{T_{\text{eff}}}} \langle \xi \rangle - 2\sqrt{\frac{T_{\text{eff}}}{T_i}} \langle \xi^3 \rangle \right) \oint dl_i \left(\frac{r_{\shortparallel}}{r_0} \right)^5 \Bigg] \\
+O(\varepsilon^4). \qquad (5.28)
\end{aligned}$$

To lowest order in ε we can extract from Eq. (5.26) a linear relaxation law for rotational movement, $I \partial_t \langle \omega \rangle = \tau_f$, describing a net frictional

torque τ_f exerted on the motor as a result of all collisions .With $\tau_f = -\gamma\langle\omega\rangle$ and $\gamma = \sum_i \gamma_i$ we derive a microscopic expression for the friction coefficient γ_i of each part of the object:

$$\gamma_i = 4\rho_i\sqrt{\frac{k_B T_i m}{2\pi}} \oint dl_i r_{\shortparallel}^2. \tag{5.29}$$

To order ε^2 the average angular velocity in a stationary state appears from Eq. (5.26) as

$$\begin{aligned}\langle\omega\rangle &= \frac{\sqrt{2\pi k_B m}}{4I}\frac{\sum_i \rho_i(T_{\text{eff}} - T_i)\oint dl_i r_{\shortparallel}^3}{\sum_i \rho_i\sqrt{T_i}\oint dl_i r_{\shortparallel}^2} \\ &= \frac{k_B m}{\gamma I}\sum_i \rho_i(T_{\text{eff}} - T_i)\oint dl_i r_{\shortparallel}^3.\end{aligned} \tag{5.30}$$

Here, we substituted the expression for the second moment from Eq. (5.28) to order ε. To this order the second moment is given by

$$\langle\omega^2\rangle = \frac{k_B T_{\text{eff}}}{I}, \tag{5.31}$$

while the effective temperature is found according to its definition,

$$T_{\text{eff}} = (\sum_i \gamma_i T_i)/(\sum_i \gamma_i). \tag{5.32}$$

Using higher order terms in the expansions for $\langle\xi^n\rangle$ results in correction terms to the expressions for $\langle\omega\rangle$ and $\langle\omega^2\rangle$. The correction terms are in both a factor m/M smaller than the presented first terms. Later in this text [Eq. (5.107)] we use a higher order expression for $\langle\omega\rangle$; these expressions become very elaborate.

5.4 Three-dimensional model of the motor

The results of a fully three-dimensional analysis are very similar to those derived in the previous two-dimensional case. We will clarify the principal differences here.

The motor parts are now determined by their surface S_i (i is the reservoir in which the part resides), to be described by a vector $\vec{r}(x, y, z)$

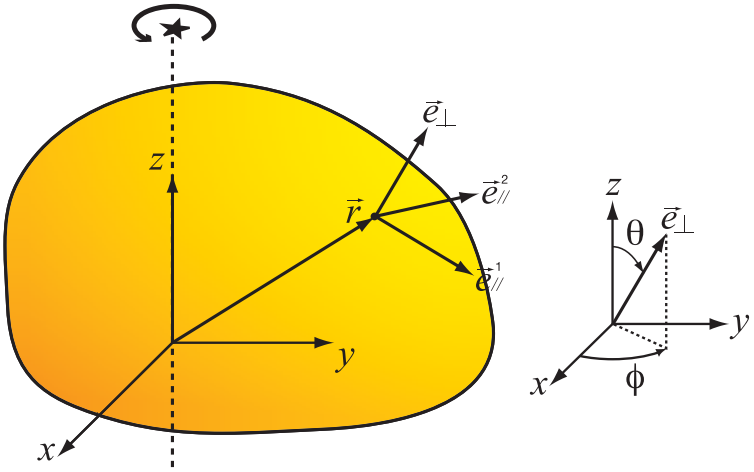

Figure 5.4: The coordinate system used for the three-dimensional model. In each reservoir, the surface of a motor part can be described by $\vec{r}(x, y, z)$, where the rotation axis is chosen as the z-axis of a cartesian coordinate system. The orientation of the surface at any point is given by the polar angle θ and the azimuthal angle φ of the normal outward vector $\vec{e}_\perp$ on the surface at this point, with the polar axis parallel to the rotation axis. The orthogonal unit vectors $\vec{e}_{1,\shortparallel}$ and $\vec{e}_{2,\shortparallel}$ are tangential to the surface.

from the origin. Again we choose the rotation axis to be the z-axis. See Fig. 5.4 for a depiction of the coordinate system used. The orientation of the surface at a certain location (x, y, z) is uniquely determined by the normal outward unit vector, $\vec{e}_\perp = (\sin\theta\cos\varphi, \sin\theta\sin\varphi, \cos\theta)$, described by two angles θ and φ, polar and azimuthal angles in a spherical coordinate system.

The assumption that there is only a central force during an interaction with a gas particle, entails that there is conservation of momentum of a gas particle along any tangential direction. So for the speed of the gas particle before $[\vec{v'} = (v'_x, v'_y, v'_z)]$ and after $[\vec{v} = (v_x, v_y, v_z)]$ the collision, we can write this condition formally as

$$\vec{v'} \cdot \vec{e}_{k,\shortparallel} = \vec{v} \cdot \vec{e}_{k,\shortparallel}, \quad k = 1, 2, \tag{5.33}$$

where $\vec{e}_{1,\shortparallel}$ and $\vec{e}_{2,\shortparallel}$ are two distinct unit vectors perpendicular to $\vec{e}_\perp$. It is convenient to use $\vec{e}_{1,\shortparallel} = (\cos\theta\cos\varphi, \cos\theta\sin\varphi, -\sin\theta)$ and $\vec{e}_{2,\shortparallel} = (-\sin\varphi, \cos\varphi, 0)$. Together with conservation of total energy and angular momentum in the z-direction [the three-dimensional expressions are straightforward extensions of the two-dimensional versions, Eqs. (5.8a), (5.8b)] we find a relation for the change of angular velocity induced by one collision:

$$\begin{aligned}\omega &= \omega' + 2\frac{(v'_x + \omega' y)\cos\varphi + (v'_y - \omega' x)\sin\varphi + v'_z \cot\theta}{\frac{1}{\sin^2\theta(x\sin\varphi - y\cos\varphi)}\frac{I}{m} + x\sin\varphi - y\cos\varphi} \\ &= \omega' + 2\frac{(\vec{V'} - \vec{v'}) \cdot \vec{e}_\perp}{r_{\shortparallel} + \frac{I}{m r_{\shortparallel}}}.\end{aligned} \tag{5.34}$$

$(\vec{V'} - \vec{v'}) \cdot \vec{e}_\perp$ is the component of the velocity difference between motor and gas particle perpendicular to the surface at the place of impact. $r_{\shortparallel}$ is now defined as

$$r_{\shortparallel} = -x\sin\theta\sin\varphi + y\sin\theta\cos\varphi = (\vec{e}_\perp \times \vec{r})|_z. \tag{5.35}$$

The latter expression signifies the z-component of the vector product of $\vec{e}_\perp$ and $\vec{r}$. $r_{\shortparallel}$ is zero in locations where the surface is perpendicular to $\vec{r}$, these coincide with zero momentum transfer. Maximal momentum transfer and $r_{\shortparallel}$ occur when the rotation axis intersects the plane tangential to the surface at this location.

The transition probability $dW(\omega|\omega')$ caused by all possible collisions with a surface element dS_i of the motor, is then found by integrating over all velocities that obey the collision rules,

$$\begin{aligned} dW_i(\omega|\omega') = dS_i \int_{-\infty}^{+\infty} dv'_x \int_{-\infty}^{+\infty} dv'_y \int_{-\infty}^{+\infty} dv'_z \\ \times H[(\vec{V}' - \vec{v}') \cdot \vec{e}_\perp] |(\vec{V}' - \vec{v}') \cdot \vec{e}_\perp| \\ \times \rho_i \phi_i(v'_x, v'_y, v'_z) \delta \left[\omega - \omega' - 2 \frac{(\vec{V}' - \vec{v}') \cdot \vec{e}_\perp}{r_{\shortparallel} + \frac{I}{m r_{\shortparallel}}} \right]. \end{aligned} \quad (5.36)$$

Adding the contributions of all surface elements dS_i in all reservoirs i, gives us the total transition probability,

$$W(\omega|\omega') = \sum_i \int_{\text{surface}} dW_i(\omega|\omega'). \quad (5.37)$$

Again, for a Maxwellian velocity distribution,

$$\phi_i(v_x, v_y, v_z) = \left(\frac{m}{2\pi k_B T_i} \right)^{3/2} \exp\left(\frac{-m(v_x^2 + v_y^2 + v_z^2)}{2 k_B T_i} \right), \quad (5.38)$$

we can do the integration over v_x, v_y, v_z analytically and find

$$\begin{aligned} W(\omega|\omega') = \frac{1}{4} \sum_i \int dS_i \rho_i \sqrt{\frac{m}{2\pi k_B T_i}} \\ \times (r_{\shortparallel} + \frac{I}{m r_{\shortparallel}})^2 H[(\omega - \omega') r_{\shortparallel}] |\omega - \omega'| \\ \times \exp\left[-\frac{m}{2 k_B T_i} \left((r_{\shortparallel} + \frac{I}{m r_{\shortparallel}}) \frac{\omega' - \omega}{2} - r_{\shortparallel} \omega' \right)^2 \right]. \end{aligned} \quad (5.39)$$

This expression is identical to its two-dimensional equivalent [Eq. (5.19)], apart from the different definition of $r_{\shortparallel}$, and obviously an integration over the surface instead of the boundary. The previous algebraic technique can then be applied to derive results for a general shape of the motor, such as for the average angular velocity in a steady state,

$$\langle \omega \rangle = \frac{\sqrt{2\pi k_B m}}{4I} \frac{\sum_i \rho_i (T_{\text{eff}} - T_i) \int dS_i r_{\shortparallel}^3}{\sum_i \rho_i \sqrt{T_i} \int dS_i r_{\shortparallel}^2}, \quad (5.40)$$

and the friction coefficient,

$$\gamma = \sum_i \gamma_i = \sum_i 4\rho_i \sqrt{\frac{k_B T_i m}{2\pi}} \int dS_i r_{\shortparallel}^2. \tag{5.41}$$

where T_{eff} is still defined as

$$T_{\text{eff}} = (\sum_i \gamma_i T_i)/(\sum_i \gamma_i). \tag{5.42}$$

5.4.1 Cylindrical shapes

For cylindrical three-dimensional shapes of the motor parts, our analysis can be reduced to two spatial dimensions, via an appropriate scaling of the densities involved. The three-dimensional shapes then consist of two equal, flat (two-dimensional) shapes as top and bottom surfaces separated by a distance H, with the rotation axis perpendicular to the flat surfaces, and an edge surface parallel to the rotation axis. We consider again the parameter $r_{\shortparallel}$ defined in three dimensions as

$$r_{\shortparallel,3D} = -x \sin\theta \sin\varphi + y \sin\theta \cos\varphi. \tag{5.43}$$

For the top (bottom) surface, $\theta = 0$ ($\theta = \pi$), hence $r_{\shortparallel,3D} = 0$ and we can conclude that these surfaces play no part in the rotational dynamics. For the edge surface, $\theta = \pi/2$ and $\sin\theta = 1$, so that we recover the two-dimensional expression for $r_{\shortparallel,2D}$, defined in Eq. (5.10). Thus, for cylindrical three-dimensional geometries, the factors depending on the shape occurring in Eq. (5.40) can be written as

$$\int dS\, r_{\shortparallel,3D}^2 = H \oint dl\, r_{\shortparallel,2D}^2, \tag{5.44}$$

$$\int dS\, r_{\shortparallel,3D}^3 = H \oint dl\, r_{\shortparallel,2D}^3. \tag{5.45}$$

If we assume homogeneous interiors for the device's parts (constant density ϱ^{3D}), the inertial moment I can be written as

$$I = \varrho^{3D} \int r_{\perp}^2 dV = \varrho^{3D} H \int r^2 dA. \tag{5.46}$$

The first integral is over the interior volume of $r_\perp^2$, with $r_\perp$ the orthogonal distance to the rotation axis. The second integral is over a top (or bottom) surface, where we have omitted the now superfluous subscript in $r_\perp$. The transition from a three-dimensional to a two-dimensional analysis for homogeneous cylindrical shapes is then completed by an appropriate scaling of the involved densities:

$$\varrho^{2D} = H\varrho^{3D}, \tag{5.47}$$

$$\rho_i^{2D} = H\rho_i^{3D}. \tag{5.48}$$

This way, the two-dimensional expression of Eq. (5.30) is retrieved from Eq. (5.40). We will start our analysis of the results with a study of two-dimensional shapes (or, equivalently, three-dimensional cylindrical shapes), as the two-dimensional expressions are easier to examine.

5.5 Analysis and discussion

Now that we derived analytical results for any shape and any number of reservoirs, we are ready to analyze concrete systems. We are interested in the role of external parameters, such as the temperature and the density of the gas, and in the construction and shape of the motor itself.

5.5.1 Temperature gradient

When the thermal reservoirs are at equilibrium with each other, we immediately see from Eq. (5.32) that $T_1 = T_2 = \cdots = T_i = T_{\text{eff}}$, independently of the construction we propose. The average angular velocity

$$\langle\omega\rangle = \frac{k_B m}{\gamma I} \sum_i \rho_i (T_{\text{eff}} - T_i) \oint dl_i r_{\shortparallel}^3, \tag{5.49}$$

becomes zero. It is impossible to extract net motion from a system in equilibrium.

5.5.2 Chirality

The next element we want to discuss is the factor $\oint dl_i r_{\shortparallel}^3$ in Eq. (5.49). Consider a motor shape in one reservoir i that is symmetrical with respect

to a plane through the rotation axis. A simple argument reveals that $\oint dl_i r_{\shortparallel}^3 = 0$: for every point (x, y) on the boundary of the shape with value $r_{\shortparallel}$ there can be found a point (x', y') for which $r'_{\shortparallel} = -r_{\shortparallel}$. The contour integral of $r_{\shortparallel}$ is therefore zero, considering that the line element dl_i is positive.

A construction that consists entirely of symmetric shapes will yield zero average rotation. Such a construction in its most simple form could consist of flat blades through the rotation axis in every reservoir. To find a net angular velocity, the motor must have at least one chiral part. The factor $\oint dl_i r_{\shortparallel}^3$ will be analyzed in more detail in a later section.

5.5.3 Friction and propulsion

In the full expression

$$\langle \omega \rangle = \frac{\sqrt{2\pi k_B m}}{4I} \frac{\sum_i \rho_i (T_{\text{eff}} - T_i) \oint dl_i r_{\shortparallel}^3}{\sum_i \rho_i \sqrt{T_i} \oint dl_i r_{\shortparallel}^2}, \tag{5.50}$$

the factor $\oint dl_i r_{\shortparallel}^2$ in the denominator stems from the friction each motor part encounters while rotating in the gas. If we are intent on optimizing the motor, the first idea would be to minimize this factor. A surface where $r_{\shortparallel}$ is zero at every point corresponds to a sphere (circle), but $\oint dl_i r_{\shortparallel}^3$ will be zero as well, resulting in zero net motion. Large average angular velocities will be obtained then by a compromise between a small $\oint dl_i r_{\shortparallel}^2$, and a large $\oint dl_i r_{\shortparallel}^3$. The 'propulsion' of the motor originates in the factor $\oint dl_i r_{\shortparallel}^3$. The largest friction will be experienced by a shape for which $r_{\shortparallel}$ is maximal. This corresponds to a (flat) surface, or blade, through the rotation axis.

5.5.4 Motor configurations

We turn to the question of how to configure the motor. Leaving the exact choice of the shape for later, we tackle the following question: if we have a certain part of the motor in one reservoir, how will the placement of the part in the other reservoir effect the motion of the motor? We start by proposing three simple constructions (see Fig. 5.5):

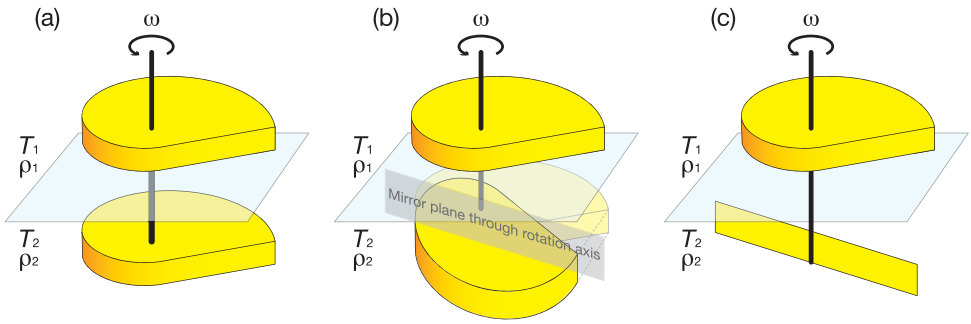

Figure 5.5: Three possible configurations of the motor parts in a two-reservoir system. (a) The part in the first reservoir is copied exactly to the other reservoir. Not only the shapes are identical, also their position relative to the rotation axis. (b) The motor part in one reservoir is reflected in the other reservoir. The reflecting plane passes through the rotation axis. (c) A general shape is combined with a blade: a plane of length L (and height H in three dimensions). Note that the system is rotationally invariant in each reservoir separately.

1. The shapes are identical in both reservoirs (Fig. 5.5a). This includes the location of the rotation axis with respect to the shape. The exact shape can be determined afterwards. With

$$\oint dl_1 r_{\shortparallel}^2 = \oint dl_2 r_{\shortparallel}^2 = \oint dl r_{\shortparallel}^2, \tag{5.51}$$

$$\oint dl_1 r_{\shortparallel}^3 = \oint dl_2 r_{\shortparallel}^3 = \oint dl r_{\shortparallel}^3, \tag{5.52}$$

   Eq. (5.50) simplifies to

$$\langle \omega \rangle = \frac{\sqrt{2\pi k_B m}}{4I} \frac{\rho_1 \rho_2 (T_2^{1/2} - T_1^{1/2})(T_2 - T_1)}{(\rho_1 T_1^{1/2} + \rho_2 T_2^{1/2})^2} \frac{\oint dl\, r_{\shortparallel}^3}{\oint dl\, r_{\shortparallel}^2}. \tag{5.53}$$

2. The shapes are still general but they are exact mirror images of each other in both reservoirs (Fig. 5.5b). Also the location of the

rotation axis with respect to the shape is mirrored. The mirror axis (plane) is through the rotation axis, but its orientation is of no importance, as our system is rotationally invariant. Writing

$$\oint dl_1 r_{\shortparallel}^2 = \oint dl_2 r_{\shortparallel}^2 \quad = \oint dl r_{\shortparallel}^2, \tag{5.54}$$

$$\oint dl_1 r_{\shortparallel}^3 = -\oint dl_2 r_{\shortparallel}^3 = \oint dl r_{\shortparallel}^3, \tag{5.55}$$

Eq. (5.50) now becomes

$$\langle\omega\rangle = \frac{\sqrt{2\pi k_B m}}{4I} \frac{\rho_1\rho_2(T_2^{1/2} + T_1^{1/2})(T_2 - T_1)}{(\rho_1 T_1^{1/2} + \rho_2 T_2^{1/2})^2} \frac{\oint dl\, r_{\shortparallel}^3}{\oint dl\, r_{\shortparallel}^2}. \tag{5.56}$$

3. We use a general (yet unknown) shape in the first reservoir, while in the second reservoir we put a blade of length L, rotating about one end (Fig. 5.5c). Omitting the index $i = 1$, and identifying

$$\oint dl_2 r_{\shortparallel}^2 = 2L^3/3, \tag{5.57}$$

$$\oint dl_2 r_{\shortparallel}^3 = 0, \tag{5.58}$$

we obtain

$$\langle\omega\rangle = \frac{\sqrt{2\pi k_B m}}{4I} \frac{\rho_1\rho_2 T_2^{1/2}(T_2 - T_1)(2L^3/3) \oint dl\, r_{\shortparallel}^3}{(\rho_1 T_1^{1/2} \oint dl\, r_{\shortparallel}^2 + \rho_2 T_2^{1/2}(2L^3/3))^2}. \tag{5.59}$$

Comparing the three suggested configurations, we see configuration (1) is even when the temperature difference $\Delta T = T_1 - T_2$ is inverted, while (2) and (3) are odd. For small temperature differences, $\langle\omega\rangle$ is approximately parabolic in ΔT, while (2) and (3) are linear. For small ΔT therefore, (1) yields much lower angular speeds than (2) and (3).

For a small temperature difference a rather technical calculation indicates that the average angular velocity for configuration (2) is at least twice that of construction (3) for the same general shape with similar linear dimensions as the blade.

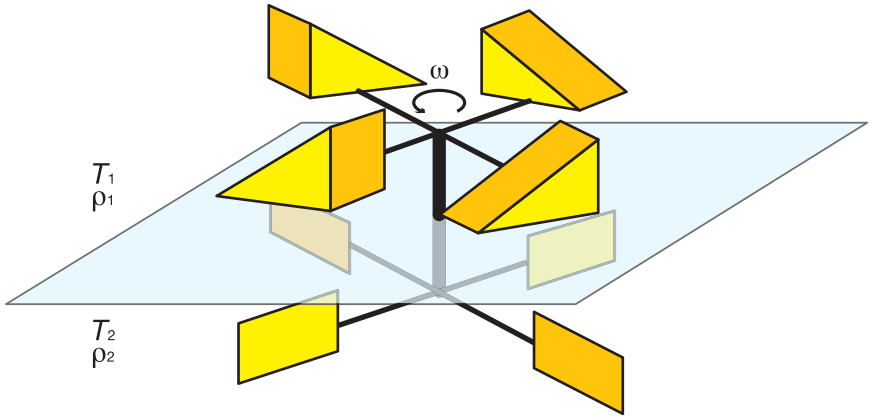

Figure 5.6: A motor with multiple identical shapes in each reservoir. For the depicted configuration with equal multiples, $n = m = 4$, we show that the resulting average angular velocity is the same as that for only one shape in each reservoir.

In a numerical procedure described later, we discovered that the configuration of two mirror shapes in the two reservoirs produces the maximal average angular velocity. In other words, given a certain part in one reservoir, the highest average angular velocity is obtained by using the reflected shape in the other reservoir.

One could think of multiple but identical structures (blades) in each reservoir, as illustrated in Fig. 5.6. Ignoring the increased probability of multiple collisions of gas particles with the motor, our theory leads to an average angular velocity

$$\langle\omega\rangle = \frac{\sqrt{2\pi k_B m}}{4I} \frac{\rho_1\rho_2(T_2 - T_1)\left(T_2^{1/2}\oint dl_1\, r_{\shortparallel}^3 \oint dl_2\, r_{\shortparallel}^2 - T_1^{1/2}\oint dl_2\, r_{\shortparallel}^3 \oint dl_1\, r_{\shortparallel}^2\right)}{\left(\sqrt{\frac{n}{m}}\rho_1 T_1^{1/2}\oint dl_1\, r_{\shortparallel}^2 + \sqrt{\frac{m}{n}}\rho_2 T_2^{1/2}\oint dl_2\, r_{\shortparallel}^2\right)^2}, \tag{5.60}$$

for a system with n identical shapes in reservoir 1 and m identical shapes in reservoir 2. The appearing contour integrals are over *one* shape of the set of identical shapes. For the same number of shapes in both reservoirs,

$n = m$, the average angular velocity is the same as with only one blade in each reservoir. The result also indicates that it is beneficial to have the highest number of blades in the reservoir with the highest $\rho T^{1/2} \oint dl\, r_{\shortparallel}^2$ factor, or simply the highest $\rho T^{1/2}$ factor if the blades have the same shape in both reservoirs.

5.5.5 Globular proteins

Looking for real-world candidates to fill the role of our Brownian motor, we turn our attention to biological systems. In the further analysis we want to use physical values for the dimensions, masses and so on. A possibility is to apply our model to globular proteins, substituting one for each motor part. The two parts would reside in a water environment, separated by a lipid membrane.

To obtain orders of magnitude for our results we will often refer to the values in Table 5.1.

Mass of one part	$M/2$	1.66×10^{-22}kg
Density of the motor	ϱ	1380 kg m^{-3}
Volume of one part	V	120 nm^3
Radius of one part (if assumed spherical)	R	3 nm
Particle mass (H_2O)	m	2.992×10^{-26}kg
Reservoir temperature	T_1, T_2	$\pm$300 K
Reservoir particle density	ρ_1, ρ_2	$\pm 3.3 \times 10^{28}$m^{-3}

Table 5.1: Typical parameters used for the motor and environment. The values of the individual parts correspond to those of globular proteins.

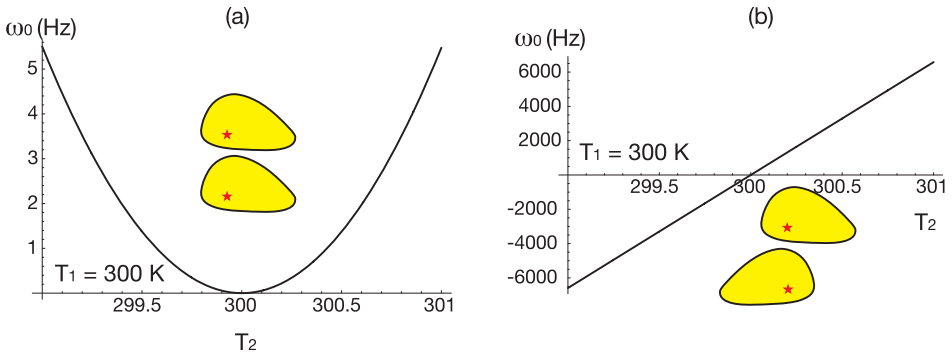

Figure 5.7: The temperature dependency of ω_0 for a configuration of (a) identical shapes and of (b) mirror shapes in the two reservoirs. One reservoir is kept at a fixed temperature $T_1 = 300$K, while the temperature T_2 in the other reservoir changes in a range of 300 ± 1K. For (a) we see a nearly parabolic dependency on $T_2 - T_1$. The sense of rotation remains the same if we switch part 1 and part 2 of the motor, and the angular velocity is rather small. For (b) we see a much larger effect, a nearly linear dependency on $T_2 - T_1$, and the sense of rotation is inverted by switching part 1 and part 2 of the motor. The densities are taken the same in both reservoirs.

5.5.6 External parameters

In the cases of identical shapes and mirror shapes [Eqs. (5.53), (5.56)] we can separate from the expressions for $\langle\omega\rangle$ a shape-dependent factor,

$$\mathcal{S} = \sqrt{A}\frac{M}{I}\frac{\oint dl\, r_{\shortparallel}^3}{\oint dl\, r_{\shortparallel}^2}. \tag{5.61}$$

A factor $\sqrt{A}$ (or $V^{1/3}$ if we prefer to work in three dimensions), which stands for the typical dimensions of a motor part, is multiplied to make $\mathcal{S}$ scale-invariant. $\mathcal{S}$ will be discussed in detail in the next section. Eqs. [5.53, 5.56] can then be written as

$$\langle\omega\rangle = \omega_0\mathcal{S}. \tag{5.62}$$

What remains is a factor ω_0 that depends on the specific configuration, the reservoir temperatures and densities, and the masses of the motor and particles:

$$\omega_0 = \omega_0^{\pm} = \frac{\sqrt{2\pi k_B m}}{4M\sqrt{A}}\frac{\rho_1\rho_2(T_2^{1/2} \mp T_1^{1/2})(T_2 - T_1)}{(\rho_1 T_1^{1/2} + \rho_2 T_2^{1/2})^2}. \tag{5.63}$$

We have used the notation ω_0^+ for the configuration with two identical shapes in the two reservoirs and ω_0^- for the configuration where the shapes are mirror images.

ω_0 is also dependent of the size of the motor. Because the mass M of the motor is also size-dependent, the full dependency could be written as $M\sqrt{A} = 2\varrho A^{3/2}$ in two dimensions, or $MV^{1/3} = 2\varrho V^{4/3}$ in three dimensions, if the density ϱ of the motor interior is considered constant. Therefore $\omega_0 \propto M^{-3/2}$ in two dimensions and $\omega_0 \propto M^{-4/3}$ in three dimensions.

In Fig. 5.7 we show the temperature dependency of ω_0, calculated with the physical values of Table 5.1 and equal reservoir densities. As mentioned before ω_0^- is linear in $T_2 - T_1$, while ω_0^+ is quadratic.

5.5.7 Shape factor

Next, we consider the size-independent geometrical factor,

$$\mathcal{S} = \sqrt{A}\frac{M}{I}\frac{\oint dl\, r_{\shortparallel}^3}{\oint dl\, r_{\shortparallel}^2}, \tag{5.64}$$

which is comprised of an interior factor M/I, and an exterior (boundary) factor $\oint dl\, r_{\shortparallel}^3 / \oint dl\, r_{\shortparallel}^2$

The factor M/I is actually independent of the mass of the motor because the inertial moment I is proportional to the mass M. It only describes the spatial distribution of mass. For a homogeneous motor interior it is given by

$$\frac{M}{I} = \frac{\sum_i A_i}{\sum_i \int r^2 dA_i}. \tag{5.65}$$

The integral is over the entire interior of the motor, and r is the distance of an interior point to the rotation axis.

Finally the factor $\oint dl\, r_{\shortparallel}^3 / \oint dl\, r_{\shortparallel}^2$ depends on the exact form of the boundary of the motor parts, where $r_{\shortparallel}$ is to be measured from the location of the rotation axis. The integrals are over the entire boundary.

To enable us to get an understanding of the geometrical factor, we introduce three simple realizations (Fig. 5.8) (in two dimensions and with homogeneous mass distributions), of which the boundary can easily be described analytically. For these prototype shapes all factors can be expressed in closed form. The shape of the motor parts are respectively a right triangle (Motor 1), an isosceles triangle (Motor 2) and a disk sector (Motor 3). Both the dimensions of the motor parts (R) and the shape (α) are fixed with one parameter, making a comparative study easier. We would also like to specify the location of the motor part relative to the rotation axis with one representative point with coordinate (x, y). For motors 1 and 2 we choose the center of mass and for motor 3 the center of the disk sector [see Fig. (5.8)] as this representative point . For these simple motors we can calculate analytical expressions for $\oint dl\, r_{\shortparallel}^2$ and $\oint dl\, r_{\shortparallel}^3$. As an example consider the Motor 2 case:

$$\oint dl\, r_{\shortparallel}^2 = \frac{2R}{9}\Big(R^2 + 3Ry\cos 3\alpha + 9y^2 + 9x^2 \sin\alpha \\ + \sin^2\alpha \left(R^2(3\sin\alpha - 2\cos 2\alpha) + 9x^2 - 9y^2 \right) \Big), \tag{5.66}$$

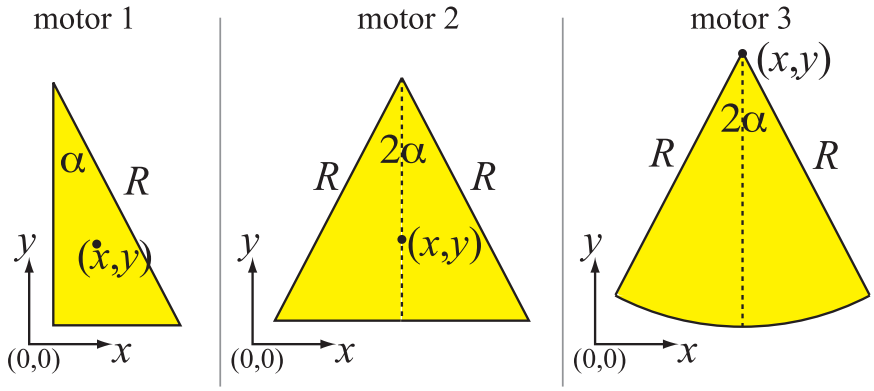

Figure 5.8: Three simple shapes for the motor parts. All are determined by a minimal number of parameters. The shape is determined by the angle α, the size by one side R, and the position with respect to the rotation axis (at the origin) by one coordinate (x, y). For the triangles (Motor 1: right triangle; Motor 2: isosceles triangle) (x, y) is the location of the center of mass, while for the disk sector (Motor 3) (x, y) corresponds to the center of the disk.

Motor 1	$I/M = R^2/18 + x^2 + y^2$
Motor 2	$I/M = R^2(2 - \cos 2\alpha)/18 + x^2 + y^2$
Motor 3	$I/M = \frac{R^2}{2} - \frac{4Ry \sin\alpha}{3\alpha} + x^2 + y^2$

Table 5.2: The ratio of the inertial moment I over the mass M of the motors in Fig. 5.8 given as a function of the location (x, y) (of the center of mass for Motors 1 and 2, and of the center of the disk for Motor 3) with respect to the rotation axis and the shape parameters, angle α and size R. The distribution of mass within the motors is assumed homogeneous.

and

$$\oint dl\, r_{\shortparallel}^3 = \frac{R}{3} x \sin 2\alpha \Big(R(3y + R\cos\alpha)(1 - 2\cos 2\alpha) + 3\left(x^2 - 3y^2\right)\cos\alpha \Big). \quad (5.67)$$

The inertial moments I for the three motors are given in Table 5.2. Some physical properties are immediately apparent from these expressions. For example $\oint dl\, r_{\shortparallel}^3$, and hence the angular velocity $\langle\omega\rangle$, is zero when

- $x = 0$: this is when the rotation axis is on the symmetry axis of the motor; there is no preferred sense of rotation,
- $\sin 2\alpha = 0$ or $\alpha = 0$ or $\alpha = \pi/2$: the motor is bar shaped, and loses its asymmetry (or chirality).

Note that $\oint dl\, r_{\shortparallel}^2$, which also appears as a factor in the expression for the friction coefficient, is *not* zero if the shape is bar shaped (or symmetrical in general).

In general the $\oint dl\, r_{\shortparallel}^3$ factor [Eq. (5.67) for Motor 2] describes the asymmetry of the motor. It also determines the sense of rotation. For example for Motor 2, the rotation sense is inverted when the rotation axis is placed on opposite sides of the symmetry axis, $x = x_0$ and $x = -x_0$.

More features can be seen from plots of the angular velocity of the motors as a function of their shape and configuration, see Figs. 5.9 (Motor

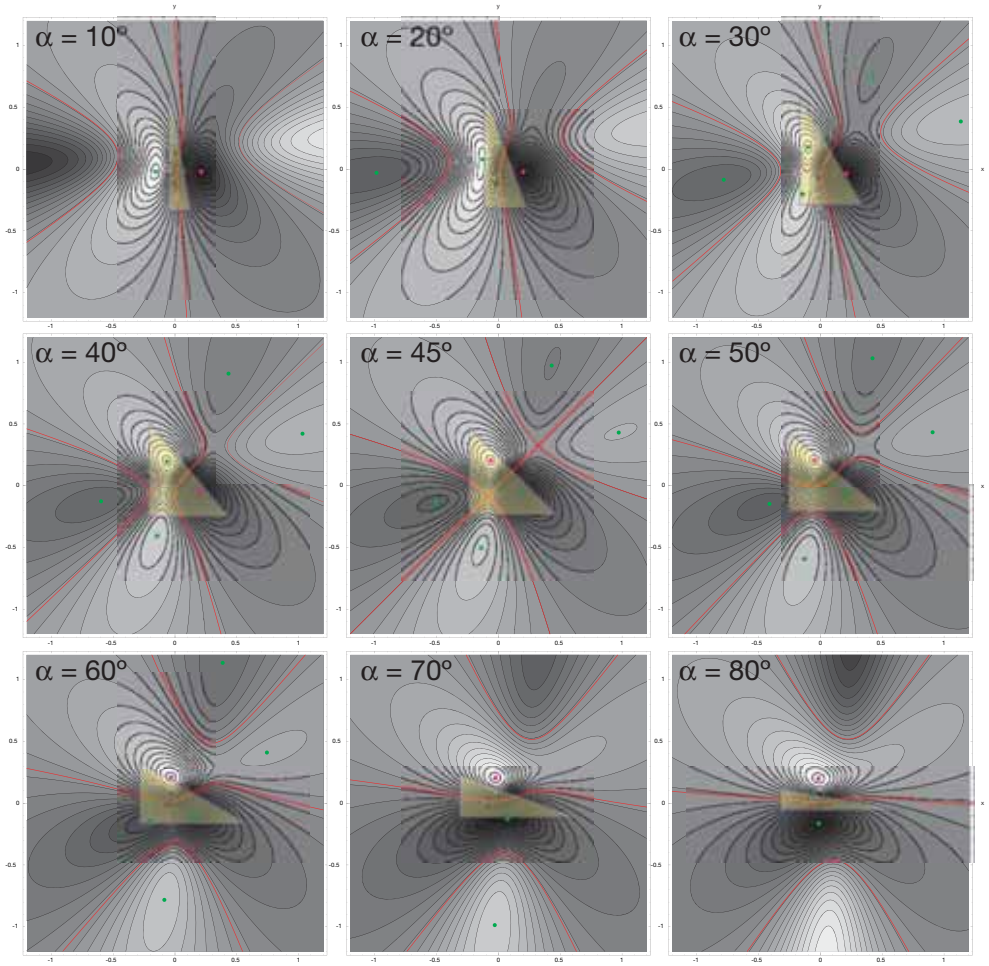

Figure 5.9: Contour plots of the average angular velocity $\langle\omega\rangle(x, y)$ of Motor 1 as a function of the location of the rotation axis (x, y), for several values of the angle α. The center of mass of the motor is in the origin $(0, 0)$. Regions in black (and white) correspond to locations for the rotation axis that yield the highest $\langle\omega\rangle$ (but in opposite sense). If the rotation axis is put on a red curve there is zero average rotation. Maxima in $\langle\omega\rangle(x, y)$ are marked by dots, the purple dot reveals the optimal place for the rotation axis (the one that gives the highest angular velocity).

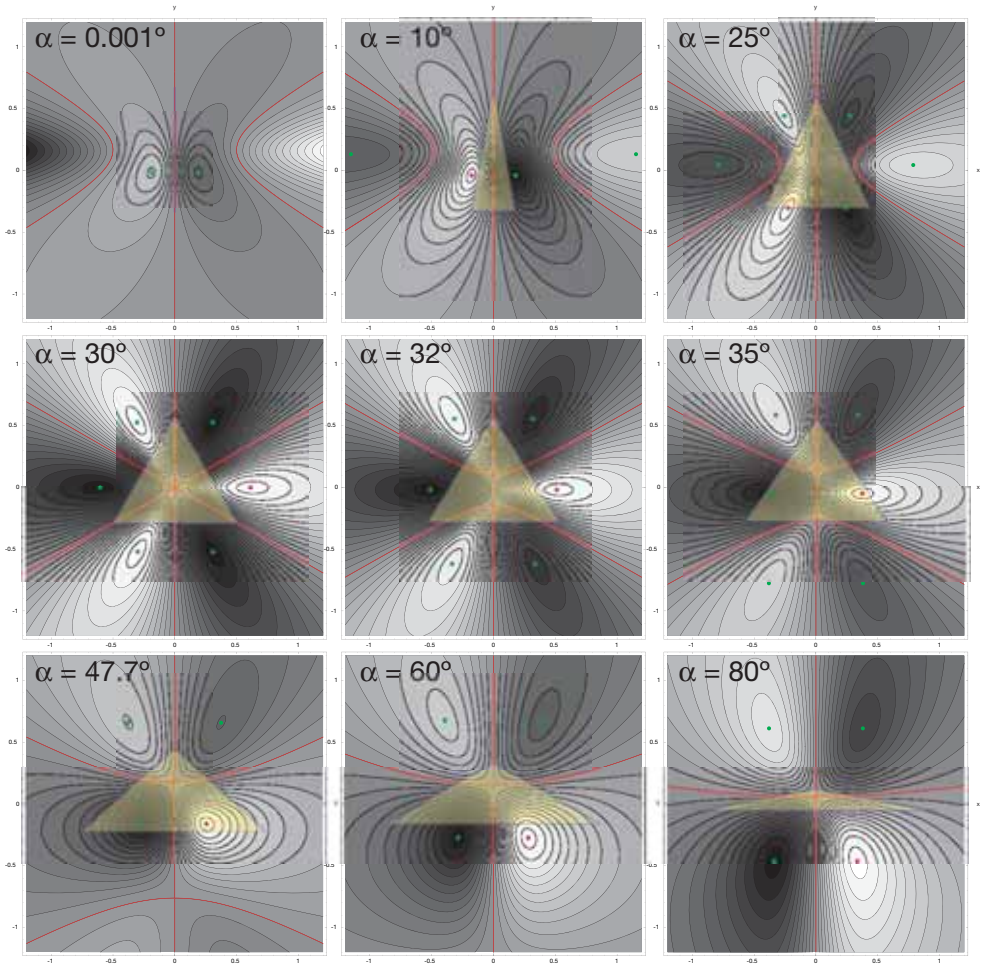

Figure 5.10: Contour plots of the average angular velocity $\langle\omega\rangle(x, y)$ of Motor 2 as a function of the location of the rotation axis (x, y), for several values of the angle α. For a technical explanation see Fig. 5.9. The symmetry of the shape is reflected in the $\langle\omega\rangle(x, y)$ plot, in particular in the locations for the rotation axis that correspond to zero average angular velocity (red curves): the y-axis for all the configurations and three symmetry axes for $\alpha = 30°$. Note that the rotation sense is opposite for locations on opposite sides of a symmetry axis.

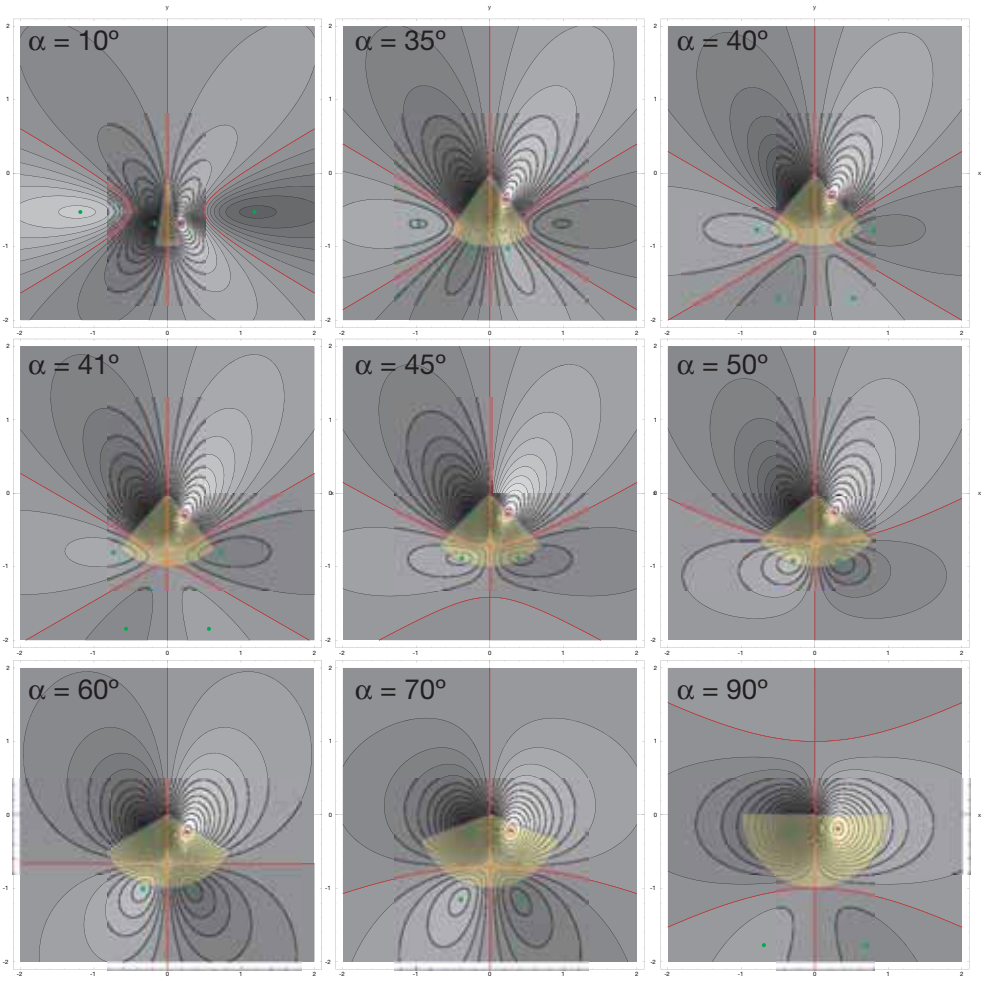

Figure 5.11: Contour plots of the average angular velocity $\langle\omega\rangle(x, y)$ of Motor 3 as a function of the location of the rotation axis (x, y), for several values of the angle α. For a technical explanation see Fig. 5.9.

1), 5.10 (Motor 2) and 5.11 (Motor 3). Note that a coordinate change was made, $x \to -x, y \to -y$. This means the coordinate (x, y) in the plot corresponds to the location of the *rotation axis* with respect to the representative point of the motor (center of mass or center of the disk), which is put in the origin of the plots. In Figs. 5.9, 5.10, 5.11 of $\langle\omega\rangle(x, y)$ we show lines of equal angular velocity (in black) and lines of zero average angular velocity (in red). Highest angular velocities are found in the black and white regions (but with opposite rotation sense). Local extrema of $\langle\omega\rangle(x, y)$ are represented by a green dot while a purple dot is the optimal location of the rotation axis. The shape of the motor is drawn in yellow.

We see that the red curves that signify zero average rotation can be straight lines when they correspond to a symmetry axis of the shape (the y-axis in Figs. 5.10, 5.11 for all shapes α, but also in Fig. 5.9 for $\alpha = 45°$ for example), but in general they follow a curved path. The regions of opposite rotation sense, separated from each other by the red curves, form not so trivial patterns.

Also interesting to note is that the location of the rotation axis that yields the highest rotation speed is always in the vicinity of the rotating Brownian motor and often in its interior. Remember that the geometrical results are scale-invariant, and the relative locations of the maxima (and zero lines) are independent of the dimensions of the motor.

For certain choices of the shape and especially of the location of the rotation axis the average rotation speed can become zero. It is therefore sensible to investigate which configurations yield the highest rotation speed. For the three simple motor realizations, we determine the location of the rotation axis that yields the highest shape factor $\mathcal{S}$ for every value of the shape parameter α, as shown in Fig. 5.12. The angle α that results in the highest $\mathcal{S}$ is listed in Table 5.3 for each of the motors. The corresponding shapes are depicted in Fig. 5.13. Considering the constraints put on the shape, Motor 1 and Motor 2 adopt very similar configurations, while the best (convex) shape for Motor 3 is a semi-disk.

5.5.8 Optimal shape

The analysis of the three motor realizations demonstrates that the angular velocity is sensitive to the precise shape of the motor. We are interested to know what happens if we relax the shape constraints while

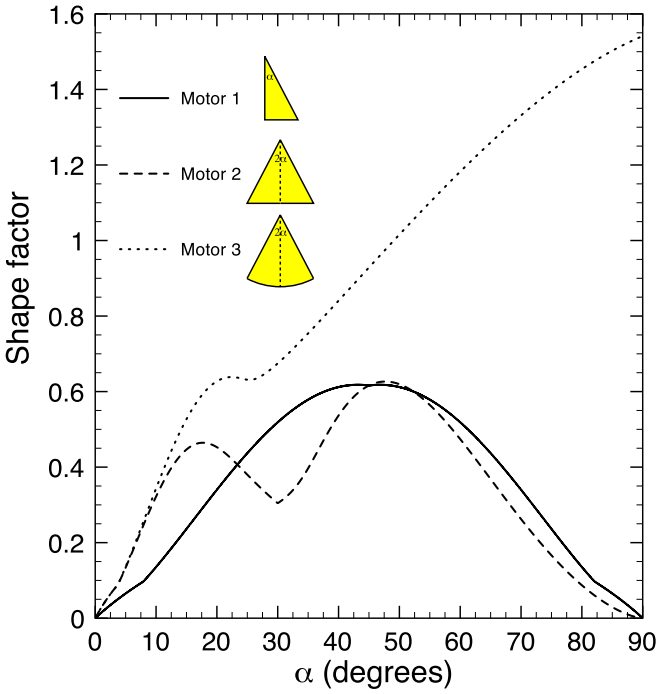

Figure 5.12: For the simple motor types (Fig. 5.8), we determined the position of the rotation axis that maximizes the average rotation speed for every shape, given by angle α. The values of α for which the shape factor $\mathcal{S}$ reaches a maximum are given in Table 5.3. It becomes clear that the shape is a key factor in the operation of the motor.

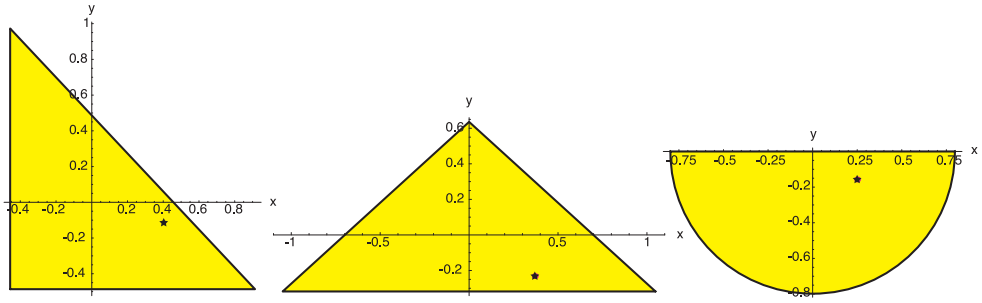

Figure 5.13: The choices for the shape and location of the rotation axis for each of the three motor realizations that result in the highest average angular velocity of the motor. The location of the rotation axis is marked by a star. Although the initial constraints for Motor 1 and 2 are different (respectively the shape of a right and isosceles triangle), in their optimal configuration they are very similar. Motor 3 is optimal in the shape of a semi-disk, while we excluded the possibility of a concave shape.

Motor	Angle α	shape factor $\mathcal{S}$
Motor 1	43.2°	- 0.618
	46.8°	0.618
Motor 2	17.7°	0.465
	47.7°	0.627
Motor 3	22.4°	0.638
	90.0°	1.54

Table 5.3: For each of the three simple motor prototypes, we shape factor $\mathcal{S}$ that corresponds to the optimal settings (shape and location of the rotation axis) is listed. The related shapes are shown in Fig. 5.13.

optimizing for maximum rotation speed. We solve this problem using a numerical procedure.

The boundary of the motor is modeled as piecewise linear. It is defined by the location of n vertices. The numerical procedure finds the optimum location of the n vertices, yielding maximum angular velocity, under the constraints that (1) the mass M remains constant, (2) the shape remains convex. The mass constraint for a homogeneous mass distribution translates into conservation of total area A. For low numbers $n = 3, 4, 5, 6$ the optimum location of the vertices is shown in Fig. 5.14. Note that the rotation axis is still fixed in the origin $(0, 0)$.

By increasing the number of vertices n, the piecewise linear shape approaches the smooth boundary that yields the highest angular velocity possible. In Fig. 5.15 the shape factor $\mathcal{S}$ is plot against the number of vertices n. We see a convergence for large n. For $n = 100$ the value of $\mathcal{S}$ is 2.29. This is a factor 3.65 higher than the best value for a triangular shape, $n = 3$, $\mathcal{S} = 0.63$. The corresponding shape (for $n = 100$) is shown in Fig. 5.16. A tentative explanation for the optimum spiral shape is that it combines a long curved section with small $r_{\shortparallel}$ (and hence small friction) with a short section that is linear, providing the necessary propulsion.

The chirality of the shape determines the rotation sense. A motor that consists of two identical optimum shapes as shown in the large figure of Fig. 5.16 actually has a negative $\mathcal{S}$. This means the motor rotates clockwise (from y-axis to x-axis). Its enantiomer (the small figure) has positive $\mathcal{S}$ and rotates counterclockwise (from x-axis to y-axis).

We initially applied the numerical procedure to identical shapes in the two reservoirs. We knew we would simultaneously find the optimum shape for the construction with mirrored shapes in both reservoirs as they share the same shape factor $\mathcal{S}$ (see Eqs. 5.53 and 5.56). Then we extended the numerical procedure so that the shapes in each reservoir could develop independently. For a small temperature difference ($\Delta T = 1$ K) the shapes become almost exactly each others mirror image (area difference $A_1/A_2 = 1.00045$). Even for a large temperature difference ($\Delta T = 100$ K) we find mirror shapes with only a small area discrepancy ($A_1/A_2 = 1.017$). The larger shape is in the reservoir with lower temperature. To obtain a positive rotation sense (from x-axis to y-axis) for a construction with mirror images, the shape with positive $\mathcal{S}$ needs to be placed in the cold reservoir , while its mirror shape with negative $\mathcal{S}$ (but equal in absolute

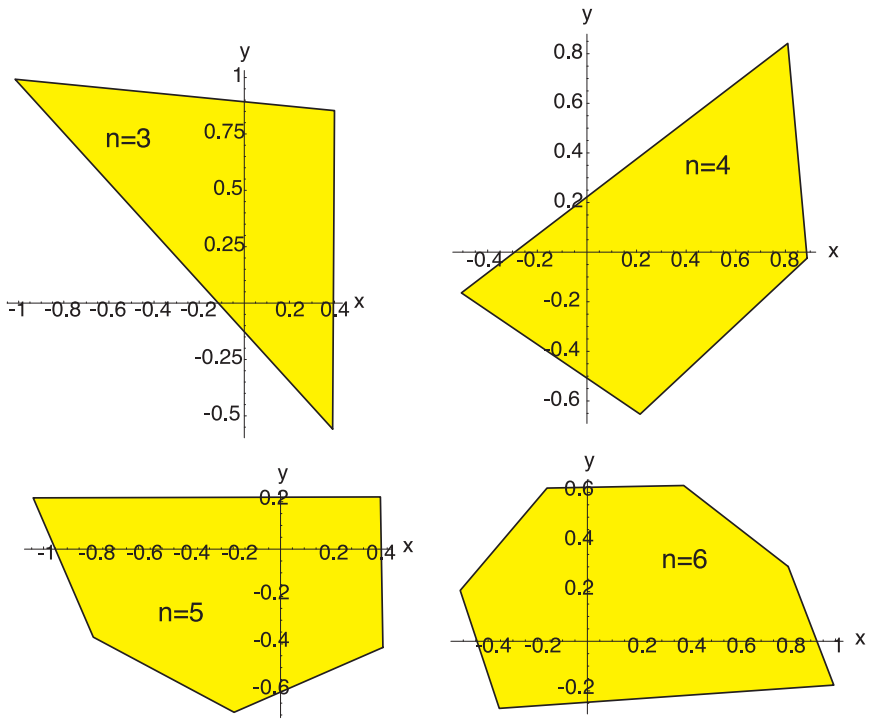

Figure 5.14: A numerical procedure was used to find optimum piecewise linear shapes, by determining the best location of each vertex. The results for a small number of vertices, $n = 3, 4, 5, 6$ are shown. Note that the results are invariant for rotations with respect the rotation axis, which is located in the origin $(0, 0)$ of the coordinate system.

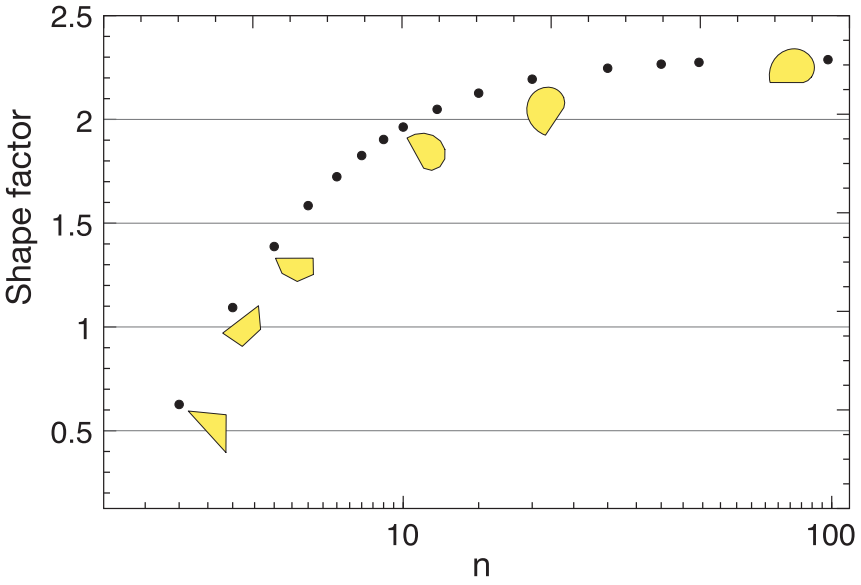

Figure 5.15: The shape factor $\mathcal{S}$ is a scale-invariant measure of the influence of the precise geometry of the motor. For $\mathcal{S} = 0$, the average angular velocity is zero. A numerical procedure was used to obtain the optimum shape (with highest $\mathcal{S}$) for a motor shape that is piecewise linear, i. e. consisting of n vertices connected by straight lines. For high n we find an approximation of the exact optimum shape and a lower limit of the maximal $\mathcal{S}$ that can be obtained. $\mathcal{S}$ converges to a value of about 2.29. A negative $\mathcal{S}$ is possible, but this corresponds to a shape that is the mirror image of the shape with opposite $\mathcal{S}$.

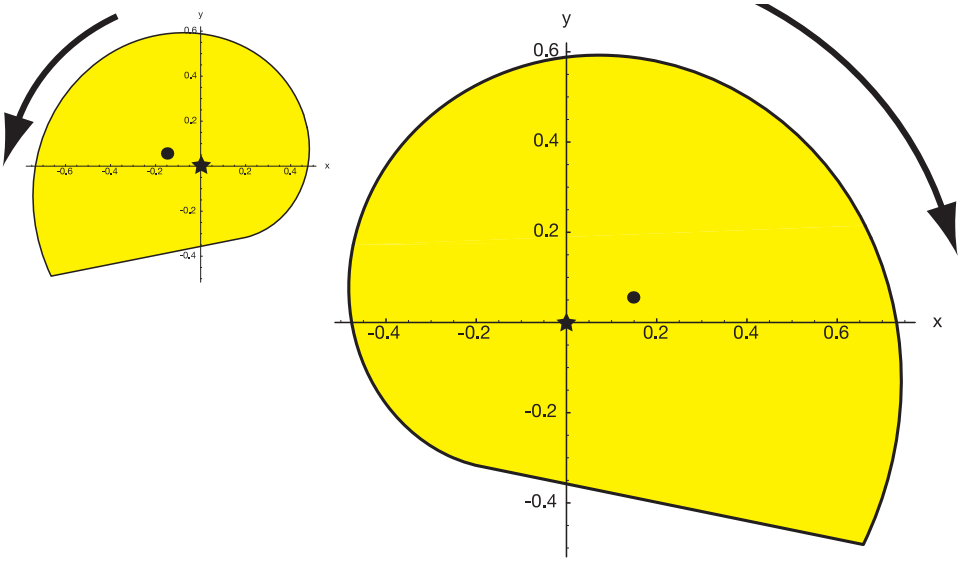

Figure 5.16: The (two-dimensional) shape of one motor part that produces the highest average angular velocity, found with a numerical procedure. The rotation axis is marked by a star [at $(0, 0)$], while the center of mass is marked by a dot. When two identical shapes are placed in both reservoirs (with equal position relative to the rotation axis), the shape in the larger figure rotates from the y-axis to the x-axis, while its mirror shape (enantiomer) in the smaller figure rotates in the opposite sense. The area of the shape is normalized to 1.

value) should be in the warm reservoir.

5.5.9 Physical estimates for the Brownian rotor

We have now collected all the necessary elements to estimate the physical properties of our motor. In a real world example of course many of the features discussed here will only be of qualitative use.

We learned that is is advantageous to use a configuration where the shape of the motor in one reservoir is the mirror image of the shape in the other reservoir (section 5.5.4). We also found the optimal individual shape (section 5.5.8). In the results we present here we assume these optimizations can be approached.

When we use the physical properties of small protein structures in an environment of water molecules (section 5.5.5) as the separate building blocks of our motors, we arrive at an average angular velocity of about 1500 Hz when driven by a temperature gradient of 0.1 K ($T_1 = 300$ K, $T_2 = 300.1$ K). This corresponds to about 230 rotations per second.

5.5.10 Three-dimensional optimal shapes

The previous optimization, when applied to three-dimensional geometries, was under the restriction of cylindrical shapes. In this section, the effect of lifting this restriction is investigated and higher 'shape factors' are shown to be feasible.

We start our analysis with the assumption of two equal or mirrored shapes for the parts in the two reservoirs. Separating the expression for the average angular velocity into shape-independent and shape-dependent factors,

$$\langle\omega\rangle = \omega_0 \mathcal{S}, \tag{5.68}$$

leads to

$$\omega_0 = \omega_0^{\pm} = \frac{1}{2\varrho V^{4/3}} \sqrt{\frac{\pi k_B m}{8}} \frac{\rho_1\rho_2(T_2^{1/2} \mp T_1^{1/2})(T_2 - T_1)}{(\rho_1 T_1^{1/2} + \rho_2 T_2^{1/2})^2}. \tag{5.69}$$

with ω_0^+ the angular velocity for two identical shapes in the two reservoirs and ω_0^- for the configuration where the shapes are mirror images. For simplicity we have assumed the density ϱ of the interior of the parts to be

constant. The volume V is that of one part, hence $M = 2\varrho V$. Note that the magnitude of the angular velocity is inversely proportional to the 4th power of the linear dimensions of the device. The remaining 'shape factor' is then dimensionless and only depends on the shape:

$$\mathcal{S} = \frac{2\varrho V^{4/3}}{I} \frac{\int dS\, r_{\shortparallel}^3}{\int dS\, r_{\shortparallel}^2} = \frac{V^{4/3}}{\int dV r_{\perp}^2} \frac{\int dS\, r_{\shortparallel}^3}{\int dS\, r_{\shortparallel}^2}. \tag{5.70}$$

In the latter expression we have used that $I = 2\varrho \int dV r_{\perp}^2$ for equal or mirror shapes.

We have employed a numerical method similar to that for the two-dimensional optimization, to find shapes that maximize $\mathcal{S}$. The shape is modeled as a convex polyhedron with triangular faces. The factors occurring in Eq. (5.70) can be calculated from the coordinates of its n vertices. The polyhedral shape is then allowed to transform randomly while only transformation steps that preserve convexity and that increase $\mathcal{S}$ are retained. Whereas for the two-dimensional optimization a restraint of fixed mass was sufficient to attain convergence to a nontrivial shape, for the three-dimensional case the absence of further restrictions leads to an infinitely high (and infinitely narrow) shape. Obviously, a distribution of mass closer to the axis of rotation, impossible in the two-dimensional case, trivially increases the inertial moment I and hence the shape factor $\mathcal{S}$. Therefore, we introduced an additional constraint, restricting the height H of the shape in the direction of the rotation axis. The obtained results for $H = 0.5$ ($n = 200$), $H = 1$ ($n = 400$) and $H = 1.5$ ($n = 200$) (with H in units $V^{1/3}$) are reproduced in Figs. 5.17, 5.18 and 5.19 respectively. Although conclusive rules are impossible to infer from a numerical procedure, we mention our observation that for shallow objects the optimal shape tends to a symmetrical configuration in the direction of the rotation axis, cf. Fig. 5.17, whereas for tall objects the tendency is towards an asymmetrical configuration in the direction of the rotation axis, with one large flat top (or bottom) surface, cf. Fig. 5.19. The distribution of profiles of numerically attained realizations, depicted in Fig. 5.20, further demonstrates this observation. The chirality of the shapes however is very clear and manifested by the appearance of a flat face in combination with a smooth rounded surface.

Table 5.4 lists the shape factors $\mathcal{S}$ corresponding with the shapes of

Height H (units $V^{1/3}$)	Shape factor $\mathcal{S}$
0.5	2.24
1	2.71
1.5	3.18

Table 5.4: Dimensionless shape factors $\mathcal{S}$ for three-dimensional optimal shapes of varying height H. To obtain actual angular velocities, $\mathcal{S}$ is multiplied by ω_0 of Eq. (5.69).

height $H = 0.5$, $H = 1$ and $H = 1.5$. Naturally, $\mathcal{S}$ increases with height as the inertial moment decreases.

So far, we have assumed the shapes in the two reservoirs to be either identical or exact mirror images. We have however also applied the described numerical algorithm to an explicit two-reservoir system with independent shapes in each reservoir. In Fig. 5.21 we show the result of an optimization of the shapes for reservoir temperatures $T_1 = 0.032$ and $T_2 = 0.045$. The two shapes resemble enantiomorphs, but close inspection reveals there is no exact correspondence in the z-direction. This can be attributed to a remaining freedom of the shape in the z-direction. We note that the resulting angular speed is 2.75% higher than when an exact mirror copy of either shape is placed in the other reservoir. This difference however can be accounted for by incomplete convergence of the shapes (each with $n = 200$ vertices). A view along the z-direction (Fig. 5.22) on the other hand seems to show that the cross sections of the two shapes in the xy-plane approach mirror images of each other. Note that the view is respectively from the top and the bottom of the rotor, hence enantiomorphs would appear as identical shapes in this projection.

5.6 Cross processes

We discussed a Brownian motor, and derived a relationship between its motion – the average angular velocity $\langle\omega\rangle$ – and the applied temperature difference ΔT. This relationship is an example of a *cross* process. The

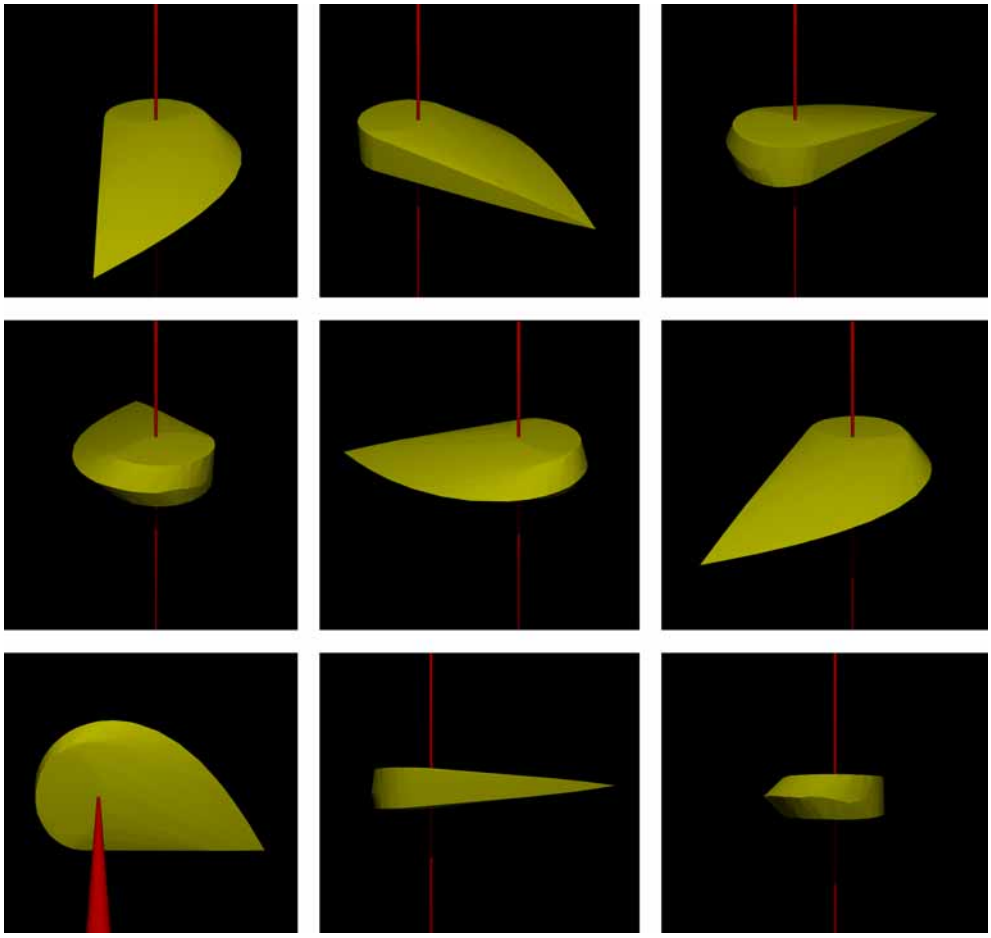

Figure 5.17: The optimal three-dimensional shape for height $H = 0.5\,V^{1/3}$ shown from different view angles. The rotation axis is colored red. This shape maximizes the net angular velocity of the Brownian rotor, when identical or mirrored shapes are placed in the two reservoirs. The shape is the result of a numerical technique employing a polyhedral structure with 200 vertices.

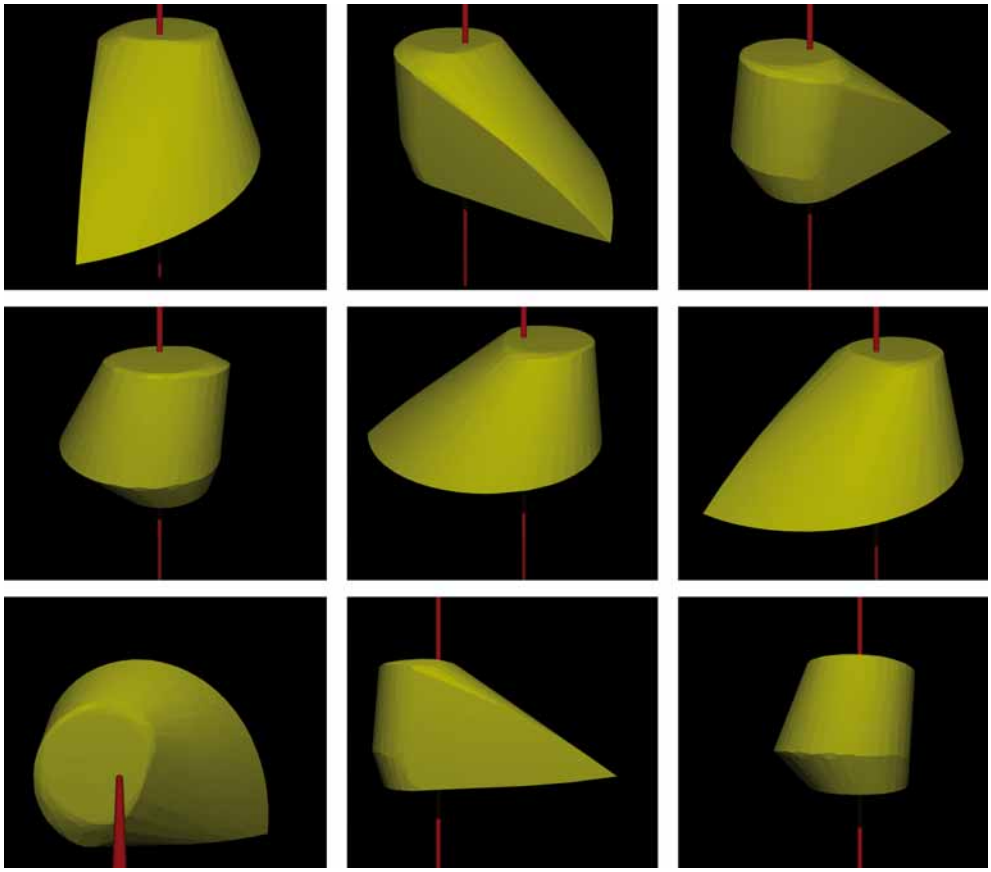

Figure 5.18: The optimal three-dimensional shape for height $H = V^{1/3}$ shown from different view angles. The rotation axis is colored red. This shape maximizes the net angular velocity of the Brownian rotor, when identical or mirrored shapes are placed in the two reservoirs. The shape is the result of a numerical technique employing a polyhedral structure with 400 vertices.

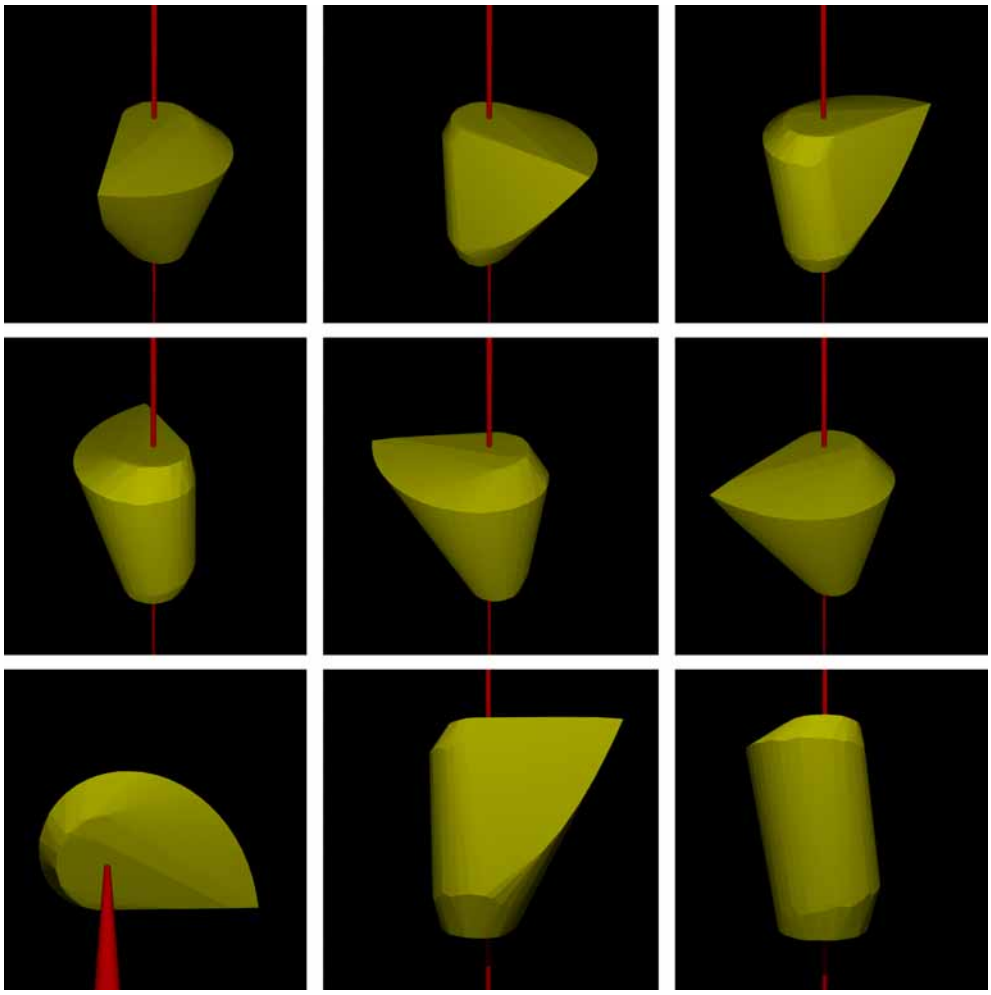

Figure 5.19: The optimal three-dimensional shape for height $H = 1.5\,V^{1/3}$ shown from different view angles. The rotation axis is colored red. This shape maximizes the net angular velocity of the Brownian rotor, when identical or mirrored shapes are placed in the two reservoirs. The shape is the result of a numerical technique employing a polyhedral structure with 200 vertices.

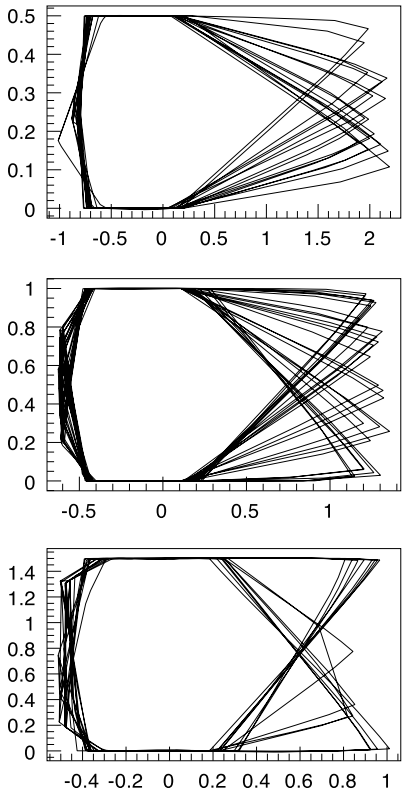

Figure 5.20: Profiles of several realizations of the three-dimensional shape as obtained from a numerical procedure. The vertical axis is in the z-direction (axis of rotation). Top figure (height $H = 0.5\,V^{1/3}$): a larger number of z-symmetric profiles occur. Bottom figure ($H = 1.5\,V^{1/3}$): a larger number of z-asymmetric profiles occur. Middle figure ($H = V^{1/3}$): no clear bias discernible. Volume $V = 1$ for all realizations.

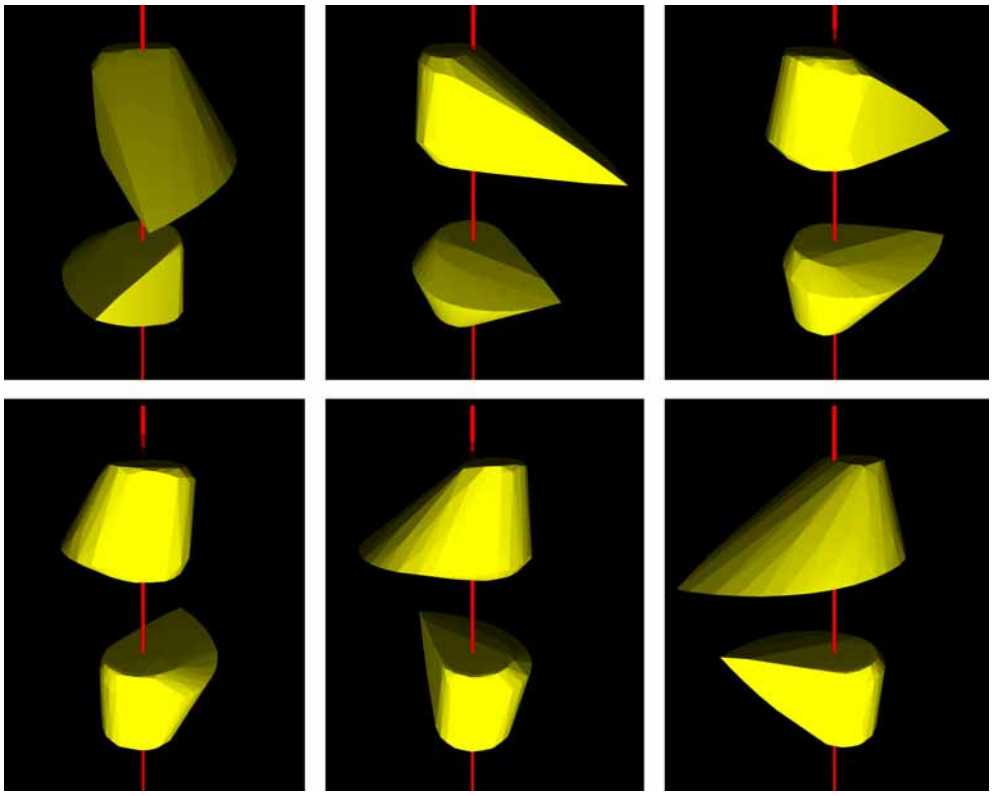

Figure 5.21: Optimal three-dimensional shapes, each in a separate reservoir (not shown), obtained from a a numerical technique when no preset relation between the two shapes is assumed. The rotation axis is colored red, views are the same shapes from different viewpoints. These shapes maximize the net angular velocity of the Brownian rotor for temperatures $T_1 = 0.032$ and $T_2 = 0.045$. Both shapes are modeled as polyhedral structures with 200 vertices, each with height restriction $H = 0.5\,V^{1/3}$.

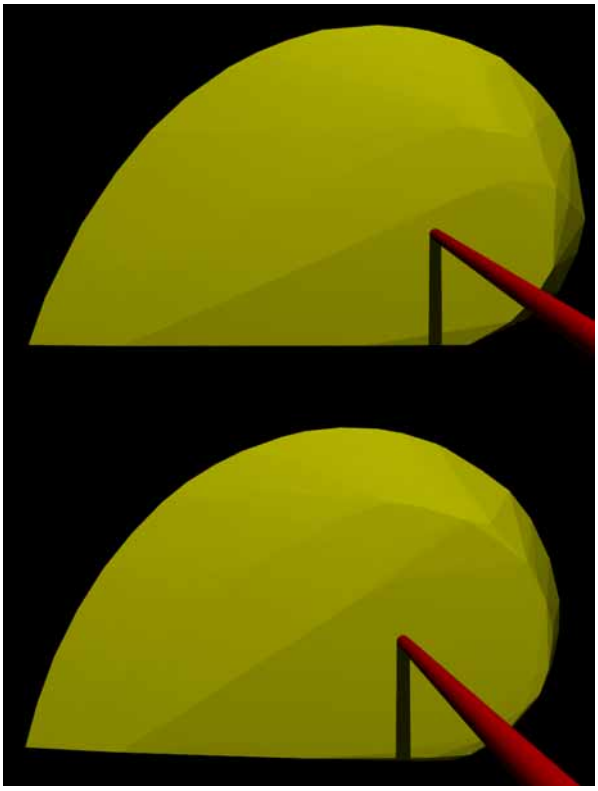

Figure 5.22: The two shapes (one in each reservoir) of Fig. 5.21 as seen from the top and the bottom.

normal process that would give rise to a motion $\langle\omega\rangle$ originates from a mechanical force. In our system with only a rotational degree of freedom this mechanical force would be in the form of a torque τ along the z-axis.

Cross processes are very common in physics. One well-known example is the Seebeck effect [49], where a temperature difference over an electric conductor causes an electric current. The Seebeck effect has a reverse or *mirror* cross process: the Peltier effect. Here, an applied electric current causes a temperature difference. Processes and their mirror processes are related through a general principle of stability. In the example of the Seebeck-Peltier effects, consider a system that is originally in equilibrium. If it is perturbed by the application of a temperature gradient, currents will start to flow (the Seebeck effect), which in turn will give rise to a counteracting temperature difference (the Peltier effect), attempting to cancel out the original cause of the disturbance. Another example is Lenz' law in electromagnetism. Moving a ferromagnetic core into a coil will induce currents in the coil. These currents are such that the resulting magnetic field will expel the core, hence counteracting the original disturbance.

Now that we established the existence of a cross process in the Brownian motor system and showed the relationship between a cross process and its mirror process, the question naturally arises: what is the mirror process in our system? It should be one that counteracts the original perturbation – a temperature difference between the reservoirs. A flow of heat $\dot{Q}_{1\to 2}$ from reservoir 1 to reservoir 2 would do exactly that. And we know the *normal* process (that causes rotational motion) is induced by a torque τ. The *mirror* cross process then is a heat flow caused by a torque. When we perturb our system in temperature equilibrium by applying a torque τ, the motor will of course rotate. How can the system react to counterbalance this motion? By creating a temperature gradient between the two reservoirs, that according to the theory of the Brownian motor will cause rotational motion. The sign of the temperature difference is such that the resulting rectified Brownian motion opposes the motion started by the torque.

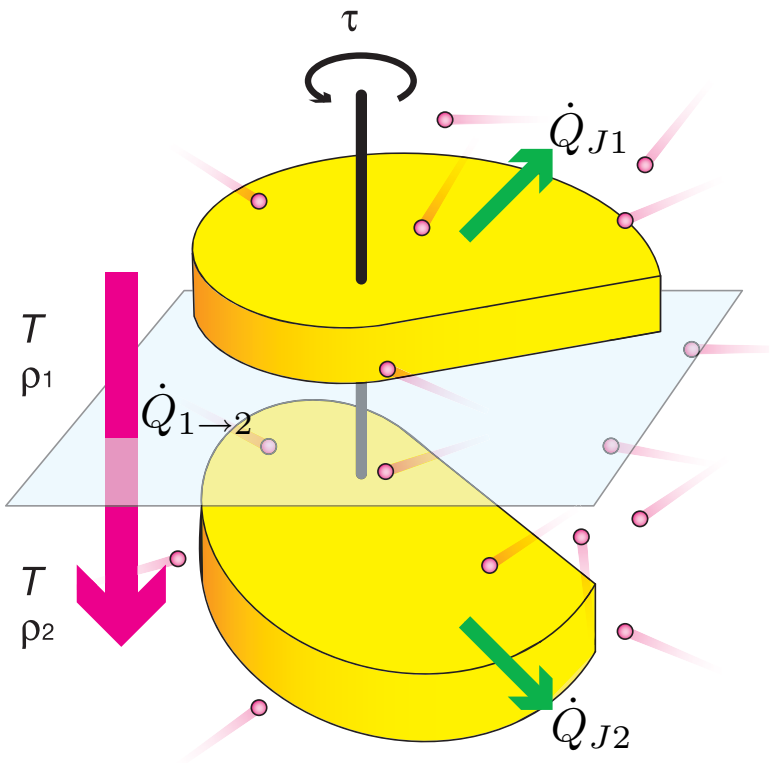

Figure 5.23: The Brownian refrigerator is a rotating device consisting of two connected bodies, each in a temperature reservoir. By applying a torque on the apparatus, a heat flow $\dot{Q}_{1\to 2}$ will arise that can cool down reservoir 1 at the expense of heating up reservoir 2. It is possible to obtain the conditions where this cooling power is larger than the dissipative heating $\dot{Q}_{J1}$.

5.7 Model of the Brownian Refrigerator

We propose a cooling apparatus or refrigerator based on the Brownian motor described before. Two reservoirs (see Fig. 5.23) are thermally isolated from each other and initially at temperature equilibrium, $T_1 = T_2 = T$. The refrigerator consists of a rotating device with a part in each reservoir. The parts are rigidly connected via a rotation axis and are subject to random collisions with particles in their reservoirs. These have mass m, considered much smaller than the total mass M of the rotating device. On applying a torque τ along the z-axis the system will develop a heat flow $\dot{Q}_{1\to 2}$, cooling reservoir 1 down at the expense of heating up reservoir 2. The following derivation of this heat flow is done for a construction where one part of the device is the reflected copy of the other (as in Fig. 5.5b) because it shows a linear response in small temperature differences $T_1 - T_2$ and it produces the highest rotating speeds and resulting heat flow.

5.8 Linear response and Onsager symmetry

Previously we derived a relation between the average angular velocity $\langle\omega\rangle$ of the rotating brownian motor and the temperatures of the two isolated reservoirs, T_1 and T_2, correct to order m/M:

$$\langle\omega\rangle = \frac{\sqrt{2\pi k_B m}}{4I}\frac{\rho_1\rho_2(T_2^{1/2}+T_1^{1/2})(T_2-T_1)}{(\rho_1 T_1^{1/2}+\rho_2 T_2^{1/2})^2}\frac{\oint dl\, r_{\shortparallel}^3}{\oint dl\, r_{\shortparallel}^2}. \tag{5.71}$$

Here I is the inertial moment of the motor with respect to its rotation axis and $\oint dl\, r_{\shortparallel}^3/\oint dl\, r_{\shortparallel}^2$ is a geometrical factor defined by the shape of the rotating motor parts. The geometrical factor is zero in a symmetrical configuration, hence the importance of choosing appropriate asymmetric or chiral elements. For a more detailed discussion of the geometrical factor we refer to Section 5.5.7. For a small temperature difference ΔT between the two reservoirs,

$$T_1 = T - \Delta T/2, \quad \Delta T = T_2 - T_1 \ll T, \tag{5.72}$$

$$T_2 = T + \Delta T/2, \qquad T = (T_1 + T_2)/2, \tag{5.73}$$

the mechanical response $\langle\omega\rangle$ is linear in ΔT to very good approximation:

$$\langle\omega\rangle \approx \frac{\sqrt{2\pi k_B m}}{2I}\frac{\rho_1\rho_2}{(\rho_1+\rho_2)^2}\frac{\oint dl\, r_{\shortparallel}^3}{\oint dl\, r_{\shortparallel}^2}\frac{\Delta T}{T^{1/2}}. \tag{5.74}$$

An elegant way to calculate the cooling potential of our system is by making use of Onsager's relations [37]. We will identify a *flow* and a *force* for the two cross processes involved. For the *mechanical* process we identify a flow $J_1 = \langle\omega\rangle$ and a thermodynamic force $X_2 = \Delta T/T^2$ in the linear relation of Eq. (5.74). The proportionality constant L_{12} of the first Onsager relation,

$$J_1 = L_{12}X_2, \tag{5.75}$$

is, for our particular system, given by

$$L_{12} = \frac{\sqrt{2\pi k_B m}}{2I}\frac{\rho_1\rho_2}{(\rho_1+\rho_2)^2}T^{3/2}\frac{\oint dl\, r_{\shortparallel}^3}{\oint dl\, r_{\shortparallel}^2}. \tag{5.76}$$

For the second cross process, the *cooling* process, we can identify a heat flow $J_2 = \dot{Q}_{1\to 2}$. The force X_1 is given by the chemical potential associated with the particle flow $J_1 = \langle\omega\rangle$ of the normal process, and is generated by the application of the torque τ. More precisely, $X_1 = \tau/T$. Again we expect a linear response

$$J_2 = L_{21}X_1. \tag{5.77}$$

Onsager symmetry now tells us that the two proportionality coefficients of the cross processes are identical,

$$L_{21} = L_{12}. \tag{5.78}$$

The heat flow from one reservoir to the other in the linear regime now becomes obvious,

$$\dot{Q}_{1\to 2} = \frac{\sqrt{2\pi k_B m T}}{2I}\frac{\rho_1\rho_2}{(\rho_1+\rho_2)^2}\frac{\oint dl\, r_{\shortparallel}^3}{\oint dl\, r_{\shortparallel}^2}\,\tau. \tag{5.79}$$

The complete Onsager relations, combining normal and cross processes, are given by:

$$J_1 = L_{11}X_1 + L_{12}X_2, \quad J_2 = L_{21}X_1 + L_{22}X_2. \tag{5.80}$$

The Onsager coefficients we have not identified yet are:

$$L_{11} = T/\gamma, \quad L_{22} = \frac{\gamma_1\gamma_2 k_B T^2}{\gamma I}, \tag{5.81}$$

while $J_1 = \langle\omega\rangle$, $J_2 = \dot{Q}_{1\to2}$, $X_1 = \tau/T$, and $X_2 = \Delta T/T^2$ as before. L_{11} can be associated to the direct mechanical response of the motor to the application of a torque, while L_{22} is related to heat conductivity, being the coefficient between the heat flow and the temperature gradient.

5.9 Results and discussion

Eq. (5.79) gives us a relation between the heat flow from reservoir 1 to reservoir 2 and the applied torque. Earlier we chose the parameters of the building blocks that constitute our motor and its environment to be comparable with globular proteins in water, see Table 5.1 for details. Using these variables again for the refrigerating device we obtain a heat flow $\dot{Q}_{1\to2}$ of 4.5 μJ/s for every pNm of torque applied. This result is for $T = 300$ K and a shape that is close to optimal. Note that in the ratio $\dot{Q}_{1\to2}/\tau$, the geometrical factor,

$$\frac{M}{I}\frac{\oint dl\, r_{\shortparallel}^3}{\oint dl\, r_{\shortparallel}^2}, \tag{5.82}$$

found earlier reappears so that the comprehensive discussion therein (sections 5.5.7 and 5.5.8) remains applicable for the various shapes the parts of the refrigerator can adopt.

In Fig. 5.24 we reproduce the dependency of the cooling power $\dot{Q}_{1\to2}/\tau$ on the densities ρ_1 and ρ_2 of the gas reservoirs for different gas temperatures T. Here we have set the cooling device in the membrane separating two gaseous environments (the values for nitrogen gas N_2 are used: $m = 5 \times 10^{-26}$kg, while for the refrigerator $M = 1.66 \times 10^{-22}$kg and typical radius 3 nm). The size of the effect is determined by the ratio of the gas densities ρ_1/ρ_2. For all temperatures maximal cooling power is found when the densities in the two reservoirs are equal, $\rho_1 = \rho_2$. Higher heat fluxes arise when the gas temperature T is higher.

The maximal torque that can be applied and the maximum obtainable temperature difference will be determined by increasing dissipative heat flows, which we discuss now.

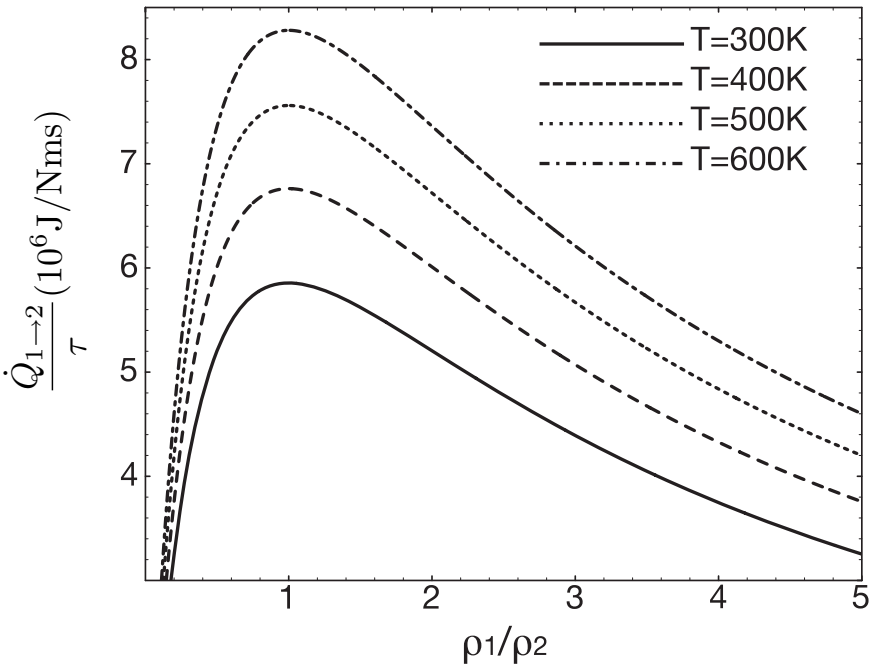

Figure 5.24: Physical values of the cooling power $\dot{Q}_{1\to 2}$ of the Brownian refrigerator in response to a torque τ are given for an environment of two nitrogen gas reservoirs for several choices of the temperature T of the gases. The device works best when the densities of the gases, ρ_1 and ρ_2, are equal. The mass of the gas particles is $m = 5 \times 10^{-26}$kg, while the mass of the device is $M = 1.66 \times 10^{-22}$kg.

5.9.1 Joule dissipation

We showed the occurrence of a heat flux $\dot{Q}_{1\to 2}$ that takes away heat from reservoir 1 to reservoir 2. Friction however will cause Joule heating in both reservoirs $i = 1, 2$ by an amount

$$\dot{Q}_{Ji} = \gamma_i \langle\omega\rangle^2 = \gamma_i \tau^2/\gamma^2. \tag{5.83}$$

If we want reservoir 1 to cool down, the heat $\dot{Q}_{1\to 2}$ transferred from reservoir 1 to 2 needs to be larger than the heat $\dot{Q}_{J1}$ dissipated by friction in reservoir 1,

$$\frac{\dot{Q}_{1\to 2}}{\dot{Q}_{J1}} = 2\frac{k_B T m}{I}\frac{\rho_2}{\tau}\oint dl\, r_{\shortparallel}^3 > 1. \tag{5.84}$$

This condition poses a limit on the applied torque:

$$\tau < \tau_{\lim} = 2\frac{k_B T m}{I}\rho_2 \oint dl\, r_{\shortparallel}^3. \tag{5.85}$$

A greater torque would cause the heat dissipation to annihilate the cooling effect. We are able to suggest a scale-invariant numerical limit for the torque. Note that both the inertial moment I and the shape factor $\oint dl\, r_{\shortparallel}^3$ scale with R^4 (R being the typical linear dimension of the refrigerator) in the case that the refrigerator parts have homogeneous density ϱ. If we assume optimum operation using the appropriate chiral shapes of the parts, as will be developed in detail later (section 5.9.2), we find

$$\varrho\frac{\oint dl\, r_{\shortparallel}^3}{I} = 1.30684. \tag{5.86}$$

This result depends only on the geometry and not on the dimensions of the parts. It will be lower for less favorable shapes and zero for a symmetric construction. The maximal torque than can be expressed as

$$\tau_{\lim} = 2k_B T\frac{\rho_2 m}{\varrho} \times 1.30684. \tag{5.87}$$

This maximal torque is proportional to the ratio of the mass density $\rho_2 m$ of gas that is heated and of the refrigerator ϱ. It does not depend on the size of cooling device. For $T = 300$ K and a system according to Table 5.1, assuming optimum shape,

$$\tau_{\lim} = 3.92 \times 10^{-21}\text{Nm}. \tag{5.88}$$

5.9.2 Maximal net cooling

The cooling power of the refrigerator is proportional to the applied torque τ [Eq. (5.79)], while the dissipative heat flux grows with τ^2 (Eq. 5.83). For large τ the cooling effect will be annihilated by dissipation and in the previous section we calculated a cut-off τ_{lim}, at which both effects cancel each other. We can also calculate the torque τ_{max} that maximizes the net cooling,

$$\dot{Q}_{\mathrm{net}} = \dot{Q}_{1\to 2} - \dot{Q}_{J1}. \tag{5.89}$$

A simple calculation leads to a maximum of $\dot{Q}_{\mathrm{net}} = A\tau - B\tau^2$ at $\tau_{\mathrm{max}} = \tau_{\mathrm{lim}}/2 = A/(2B)$, with $A = (\sqrt{2\pi k_B m T})/(2I)(\rho_1\rho_2)/((\rho_1 + \rho_2)^2)(\oint dl\, r_{\shortparallel}^3)/(\oint dl\, r_{\shortparallel}^2)$ and $B = \gamma_1/\gamma$. For the optimum torque then we find:

$$\tau_{\mathrm{max}} = \frac{k_B T m}{I}\rho_2 \oint dl\, r_{\shortparallel}^3. \tag{5.90}$$

This result, like τ_{lim}, is independent of the size of the refrigerator (assuming a homogeneous interior). It only depends on the density of the environment and the refrigerator, the environment temperature and the specific shape of the refrigerator. For an optimum shape (see later) and variables according to Table 5.1 we find:

$$\tau_{\mathrm{max}} = 1.96 \times 10^{-21}\mathrm{Nm}. \tag{5.91}$$

Substituting the explicit expression for τ_{max} into Eq. (5.89) yields the maximal net heat flow out of reservoir 1:

$$\dot{Q}_{\mathrm{net}}^{\mathrm{max}} = \frac{\sqrt{\pi}}{8}\frac{(k_B T m)^{3/2}}{I^2}\frac{\rho_1\rho_2^2}{(\rho_1+\rho_2)^2}\frac{\left(\oint dl\, r_{\shortparallel}^3\right)^2}{\oint dl\, r_{\shortparallel}^2}. \tag{5.92}$$

We see that when we also take into account the loss through friction, the refrigerator is most effective when the densities are the same in both reservoirs, $\rho_1 = \rho_2$. The net cooling is higher when the device works in higher gas densities. The reason may seem counterintuitive: the heat dissipation through friction is smaller in an environment with higher friction. With Eq. (5.83) we show that the dissipated heat is proportional to the square of the average angular velocity $\langle\omega\rangle$ that is obtained by applying a torque τ, and this velocity is lower when the friction γ is higher.

Before we can give numerical results, we need to investigate the role of the geometry of the refrigerator. We separate a scale-invariant shape factor from Eq. (5.92),

$$\mathcal{S} = \frac{1}{\sqrt{A}} \frac{M^2}{I^2} \frac{\left(\oint dl\, r_{\shortparallel}^3\right)^2}{\oint dl\, r_{\shortparallel}^2}, \tag{5.93}$$

where A is the area of one part of the construction. All the factors that depend on the shape, the contours and the inertial moment, are included in $\mathcal{S}$. We will begin straight away with optimizing this shape factor, and for most of the realizations of the refrigerator presented in this paper we assume the shape is (close to) optimum. The calculations however can also be done for other (less favorable) shapes; the elements of the calculation are comparable to those presented earlier, where we also discussed three simple model shapes that can be analyzed analytically. A similar numerical procedure as was used to find the optimal shape of the motor (see section 5.5.8), yields a value for $\mathcal{S}$, see Fig. 5.25. The procedure approximates the shape of the refrigerator parts as piecewise linear with n vertices. For sufficiently large n, $\mathcal{S}$ converges to a value slightly higher than 2. The corresponding optimum shape for the cooling function is then also found, see Fig. 5.26. The shape is that of a part of the refrigerator in one reservoir; placing the mirrored shape in the other reservoir gives the optimum configuration of the refrigerator. The axis of rotation is given by the z-axis. The numerical procedure expects the mass M of the motor to be homogeneously distributed, which reflects the reality of biological entities such as proteins that could function as parts of the device.

For a homogeneous mass distribution we write the mass of the refrigerator as $M = 2\varrho A$, with ϱ the constant density of the refrigerator parts. To find the maximum net heat flux the numerical factor $\mathcal{S}$ is multiplied by

$$\dot{Q}_0 = \frac{\sqrt{2\pi}}{16} \frac{(k_B T m)^{3/2}}{\varrho^2 A^{3/2}} \frac{\rho_1 \rho_2^2}{(\rho_1 + \rho_2)^2}, \tag{5.94}$$

so that $\dot{Q}_{\text{net}}^{\max} = \dot{Q}_0 \mathcal{S}$. Remember that our theory is two-dimensional. The result however depends on the absolute values of the gas densities ρ_1 and ρ_2, contrary to Eq. (5.79) where only their relative magnitudes play a

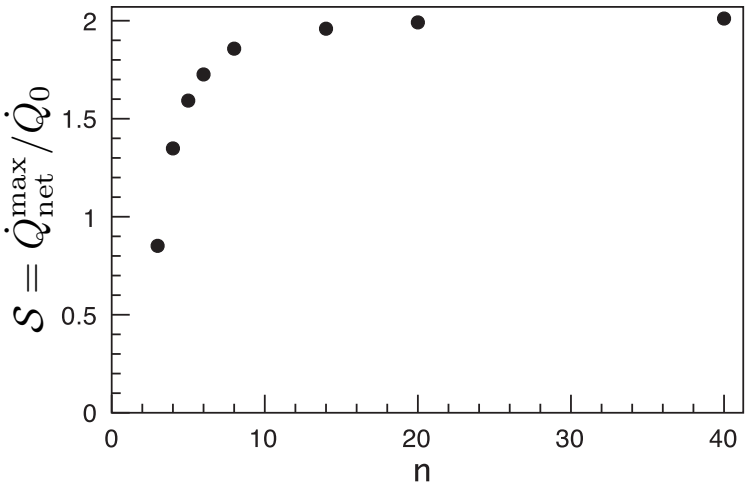

Figure 5.25: The effectiveness of the refrigerator is influenced by its (chiral) shape. $\mathcal{S}$ gives a size-independent measure of this geometrical factor. With a numerical procedure we can optimize this factor, by approximating the shape of the motor parts as piecewise linear, with n edges. For n sufficiently high we approach the highest obtainable factor $\mathcal{S}$, and the corresponding shape is represented in Fig. 5.26.

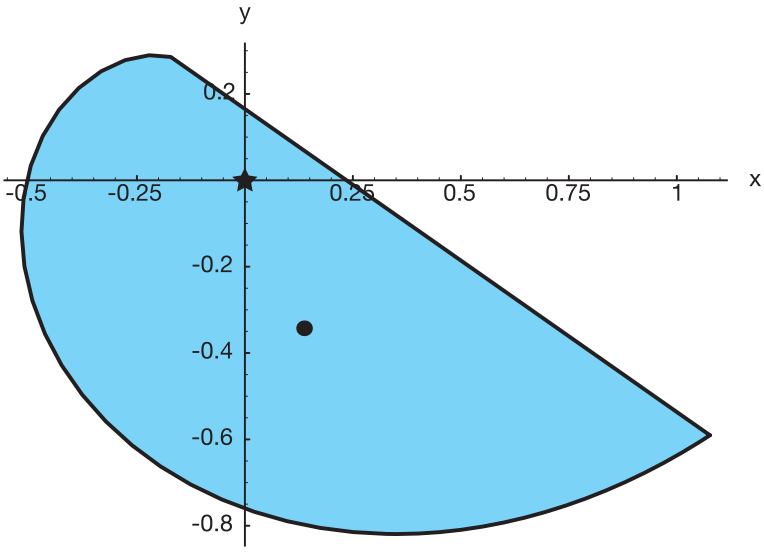

Figure 5.26: The shape of one part of the refrigerating device that maximizes the net cooling power, which also takes into account the frictional dissipation. The complete device consists of this shape in one reservoir and the *mirror* image of this shape in the other. The two parts are rigidly connected with each other by a rotation axis, marked by a star. The mass distribution in the interior of the parts is assumed homogeneous. The center of mass is represented by a dot.

part . We cannot simply insert values for three-dimensional gas densities. Therefore we make a small technical detour to describe the three-dimensional expressions and justify for which case the two-dimensional shape optimization remains valid.

5.9.3 Three-dimensional model

In a three-dimensional analysis the essential difference is the description of the geometrical factors. Instead of a contour integral $\oint dl$ there is an integral $\int dS$ over the surface of the refrigerator parts, while the vector $r_{\shortparallel}$ gets a new definition, see Section 5.4 for details. For the ratio of the cooling power over the applied torque we find

$$\frac{\dot{Q}_{1\to 2}}{\tau} = \frac{\sqrt{2\pi k_B m T}}{2I} \frac{\rho_1\rho_2}{(\rho_1+\rho_2)^2} \frac{\int dS\, r_{\shortparallel}^3}{\int dS\, r_{\shortparallel}^2}, \tag{5.95}$$

while the maximum net cooling power of reservoir 1 now becomes

$$\dot{Q}_{\text{net}}^{\max} = \frac{\sqrt{\pi}}{8} \frac{(k_B T m)^{3/2}}{I^2} \frac{\rho_1\rho_2^2}{(\rho_1+\rho_2)^2} \frac{\left(\int dS\, r_{\shortparallel}^3\right)^2}{\int dS\, r_{\shortparallel}^2}. \tag{5.96}$$

We again use a product of an external $\dot{Q}_0$ and a scale-invariant geometrical factor $\mathcal{S}$,

$$\dot{Q}_{\text{net}}^{\max} = \dot{Q}_0 \mathcal{S}. \tag{5.97}$$

The geometrical factor now needs to be scaled by a factor proportional to R^2, with R the typical linear dimension of the shape. For this we use $V^{2/3}$, with V the volume of a refrigerator part:

$$\mathcal{S} = \frac{1}{V^{2/3}} \frac{M^2}{I^2} \frac{\left(\int dS\, r_{\shortparallel}^3\right)^2}{\int dS\, r_{\shortparallel}^2}, \tag{5.98}$$

The shape factor can then be solved analytically or numerically, producing size-independent results. The remaining factor

$$\dot{Q}_0 = \frac{\sqrt{\pi}}{8} \frac{(k_B T m)^{3/2}}{M^2} \frac{\rho_1\rho_2^2}{(\rho_1+\rho_2)^2} V^{2/3} \tag{5.99}$$

$$= \frac{\sqrt{2\pi}}{16} \frac{(k_B T m)^{3/2}}{\varrho^2 V^{4/3}} \frac{\rho_1\rho_2^2}{(\rho_1+\rho_2)^2}, \tag{5.100}$$

then shows again the role of the various parameters. In the second expression for $\dot{Q}_0$ we substituted $M = 2\varrho V$ for the homogeneous case.

We now argue that we can recuperate the two-dimensional optimization of the shape factor $\mathcal{S}$ and corresponding two-dimensional shape. We propose a prismatic structure for each of the refrigerator parts, defined by two equal, flat (two-dimensional) surfaces separated by a distance H, as shown in the initial model of the device in Fig. 5.23. The rotation axis is perpendicular to the two surfaces. For this configuration it is easy to show that the surface integrals can be written as the product of the distance H and the contour integral of the top or bottom surface, exactly as in the two-dimensional description:

$$\int dS\, r_{\shortparallel}^2 = H \oint dl\, r_{\shortparallel,2D}^2, \tag{5.101}$$

$$\int dS\, r_{\shortparallel}^3 = H \oint dl\, r_{\shortparallel,2D}^3. \tag{5.102}$$

Also, for a homogeneous mass distribution,

$$\frac{M}{I} = \frac{V}{\int r_\perp^2 dV} = \frac{HA}{H\int r^2 dA}, \tag{5.103}$$

where we take the integral over the volume V of $r_\perp$, the distance to the rotation axis, and find it is equivalent to taking the surface integral over the top or bottom surface A of the prism times the thickness H. In conclusion we recover the two-dimensional shape factor [(Eq. (5.93)] by inserting the corresponding volume $V = (H\sqrt{A})^{3/2}$ in Eq. (5.98). The approach is then to use the three-dimensional expression for $\dot{Q}_0$ [Eq. (5.100)], and the numerical results for the two-dimensional case, as in Fig. 5.25.

Doing this for a temperature ($T = 300$K), reservoir densities ($\rho_1 = \rho_2 = 3.343 \times 10^{28}\mathrm{m}^{-3}$) and $m = 2.992 \times 10^{-26}$kg for an aquatic environment, and $\varrho = 1380\ \mathrm{kg\ m}^{-3}$, typical for proteins, $\dot{Q}_{\mathrm{net}}^{\max} = \dot{Q}_0\mathcal{S}$ can be expressed as a function of only the radius R of one refrigerator part. For a globular protein of typical dimension $R \approx 3$nm, we find a value of $\dot{Q}_{\mathrm{net}}^{\max} = 3.5 \times 10^{-15}$J/s. Note the strong size dependence: a refrigerator of 1 nm, would yield a cooling power of about 2.8×10^{-13}J/s. For comparison, it takes about 2.2×10^{-12}J to cool down a 1 μm small cell one Kelvin, which could be accomplished by one refrigerator of 1 nm radius in one minute.

5.9.4 Thermal conductivity

As mentioned earlier, the L_{22} Onsager coefficient can be related to heat conductivity between the reservoirs. In the linear response model, the heat conducted from one reservoir to the other can be quantified:

$$\dot{Q}_{\rm cond} = \frac{\gamma_1\gamma_2}{\gamma I} k_B \Delta T. \tag{5.104}$$

Here γ_1 and γ_2 are the friction coefficients of the separate parts of the refrigerator, and $\gamma = \gamma_1 + \gamma_2$ represents the total friction coefficient. The conductive heat flow is proportional to the temperature gradient ΔT and goes from the warm to the cold reservoir. Therefore it is directed against the cooling power of the device and for a temperature difference larger than $\Delta T_{\rm lim}$ the net cooling effect will vanish. The condition $\dot{Q}_{\rm cond} < \dot{Q}_{\rm net}^{\rm max}$ leads to

$$\frac{\Delta T}{T} < \frac{\pi}{8}\frac{m}{I}\frac{\rho_2}{\rho_1+\rho_2}\frac{\left(\oint dl\, r_{\shortparallel}^3\right)^2}{\left(\oint dl\, r_{\shortparallel}^2\right)^2}. \tag{5.105}$$

Note that the sustainable temperature gradient is proportional to m/M. In Fig. 5.27 we show $\Delta T_{\rm lim}$ for varying m/M as a function of the density ratio ρ_1/ρ_2. For our choice of the direction of the cooling effect (reservoir 1 cools down, reservoir 2 heats up), a higher relative density in reservoir 2 allows a larger $\Delta T_{\rm lim}$. In the limit of ρ_1 being much smaller than ρ_2, $\Delta T_{\rm lim}/T$ approaches $(\pi/8)(m/I)\left(\oint dl\, r_{\shortparallel}^3\right)^2 / \left(\oint dl\, r_{\shortparallel}^2\right)^2$. Earlier we found equal densities, $\rho_1 = \rho_2$, to correspond with maximum net cooling power, for which the maximum sustainable temperature gradient $\Delta T_{\rm lim}$ is half this value.

For the previously used example of globular proteins (see Table 5.1 for the parameters), $\Delta T_{\rm lim} = 4.3$ mK at $T = 300$ K and equal reservoir densities.

In all examples given, the shape is presumed to be (close to) optimal.

5.10 Molecular dynamics simulations

Two main theoretical results, the sustained rotational Brownian motion and the cooling power, are compared with molecular dynamics simulations. The simulated systems throughout this Section consist of two

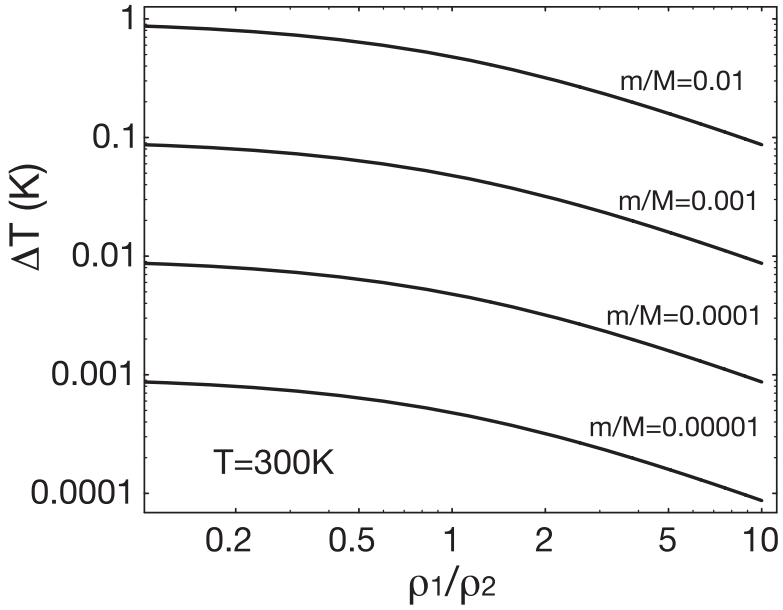

Figure 5.27: The temperature gradient ΔT for which the conductive heat flow cancels the cooling heat flow. For the device to cool down reservoir 1 (at the expense of reservoir 2), the temperature difference must remain under this limit. A small M (or large m) is beneficial. The sustainable temperature gradient is highest for high gas density ρ_2 in reservoir 2 (relative to ρ_1). For high gas density ρ_1 in reservoir 1 the obtainable temperature gradient becomes very small. The graph is for absolute temperature differences around $T = 300$ K.

reservoirs of non-interacting gas particles. To restrict the computation time, we carried out the simulations in two spatial dimensions. In each reservoir, a triangular rotor part is placed. Collisions between gas particles and the triangle are detected by numerically solving the exact equations of motion for the point in time of the impact. At each collision, the speed of the gas particle and the rotational velocity of the triangle are changed according to the rules for elastic collisions. The two gases are each confined within a 'box'. Depending on the requirements of the simulation we employed two types of boxes: closed and virtual. For both boxes the initial distribution of the speeds of the gas particles is Maxwellian. A virtual box was used when theory required a constant temperature of the gas. The walls of a virtual box 'absorb' gas particles upon collision, but also randomly 'emit' new particles (into the box' interior) such that the gas properties, in particular density ρ and Maxwellian equilibrium distribution, are preserved. In this way, an infinitely large reservoir of gas particles is simulated. A closed box was used when the effect of interest was the temperature change of the gas. The walls of a closed boxed are simply reflective. In all simulation we used a configuration with mirrored objects in the two reservoirs. The rotation axis is always centered in the box.

5.10.1 Rotor

Earlier, we derived an expression for the average sustained angular velocity of the Brownian rotor. The specific expression for mirrored shapes in the two reservoirs is

$$\langle\omega\rangle = \frac{\sqrt{2\pi k_B m}}{4I}\frac{\rho_1\rho_2(T_2^{1/2}+T_1^{1/2})(T_2-T_1)}{(\rho_1 T_1^{1/2}+\rho_2 T_2^{1/2})^2}\frac{\oint dl\, r_{\shortparallel}^3}{\oint dl\, r_{\shortparallel}^2}, \tag{5.106}$$

where the contour integrals are over the boundary of the shape in the first reservoir.

With molecular dynamics simulations we tested this prediction for a right triangle (and reflected shape in the other reservoir). In the dimensions of the simulation, the sides of the triangle were $1, 1, \sqrt{2}$. The total mass of the rotor was $M = 50$ and the mass of a single gas particle was $m = 1$. Virtual boxes of size 20×20 were used and gas temperatures

were $T_1 = 1, T_2 = 5$. The velocities of the gas particles were drawn from a Maxwellian distribution ($k_B = 1$ in the simulations). We performed simulations for different locations of the triangle with respect to the axis. In a coordinate system with the axis of rotation at the origin $(0, 0)$ and x-axis and y-axis parallel to the short sides of the triangle, the right corner of the triangle (x_c, y_c) was moved in the x-direction, such that $y_c = -1/3$. Note that the center of mass passes through the axis of origin when $(x_c, y_c) = (-1/3, -1/3)$. The simulation results for the average angular velocity $\langle\omega\rangle$ are reproduced as dots in Fig. 5.28. The error bars are given by the standard deviation of 10 000 realizations. The dashed curve represents the theoretical calculation, from Eq. (5.106). The correspondence is very satisfactory.

In the simulations however, the ratio $M/m = 50$ is much lower than in a physical realization of the rotor. The expression for $\langle\omega\rangle$ in Eq. (5.106) is correct to order $(m/M)^{3/2}$. An excellent agreement between theory and simulations is obtained when the expression for $\langle\omega\rangle$ is expanded to order $(m/M)^{5/2}$, represented in Fig. 5.28 by the solid curve, and explicitly

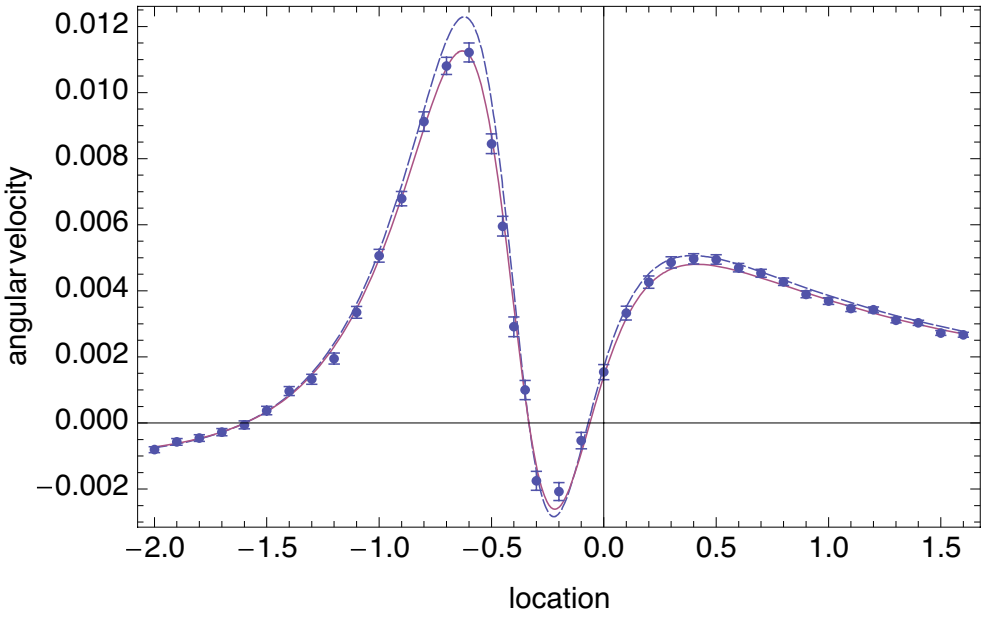

Figure 5.28: Molecular dynamics simulation results (dots and error bars) for the average angular velocity $\langle\omega\rangle$ of the Brownian rotor compared with theory to first significant order in m/M (dashed curve) and one order higher (solid curve). The shapes in both reservoirs are right triangular with sides $1, 1, \sqrt{2}$. In the abscissa is the x-coordinate (x_c) of the right corner of a triangle with respect to the rotation axis ($y_c = -1/3$). Mass of the rotor is $M = 50$ (gas particle mass $m = 1$). Gas densities are $\rho_1 = \rho_2 = 1$. The simulation results are averages over 10 000 realizations.

given (for a system with mirrored shapes) by

$$\begin{aligned}
\langle\omega\rangle =& \frac{\sqrt{2\pi k_B m T_{\text{eff}}}}{4I} \frac{\rho_1\left(1-\frac{T_1}{T_{\text{eff}}}\right)-\rho_2\left(1-\frac{T_2}{T_{\text{eff}}}\right)}{\rho_1\sqrt{\frac{T_1}{T_{\text{eff}}}}+\rho_2\sqrt{\frac{T_2}{T_{\text{eff}}}}} \frac{\oint dl\, r_{\shortparallel}^3}{\oint dl\, r_{\shortparallel}^2} \\
&+ \frac{m}{I}\frac{\sqrt{2\pi k_B m T_{\text{eff}}}}{4I}\Bigg\{ \frac{\rho_1\left(\frac{T_1}{T_{\text{eff}}}-1\right)-\rho_2\left(\frac{T_2}{T_{\text{eff}}}-1\right)}{\rho_1\sqrt{\frac{T_1}{T_{\text{eff}}}}+\rho_2\sqrt{\frac{T_2}{T_{\text{eff}}}}} \frac{\oint dl\, r_{\shortparallel}^5}{\oint dl\, r_{\shortparallel}^2} \\
&+ \frac{\rho_1\left(\frac{T_1}{T_{\text{eff}}}-\frac{7}{2}\right)-\rho_2\left(\frac{T_2}{T_{\text{eff}}}-\frac{7}{2}\right)}{\rho_1\sqrt{\frac{T_1}{T_{\text{eff}}}}+\rho_2\sqrt{\frac{T_2}{T_{\text{eff}}}}} \frac{-\oint dl\, r_{\shortparallel}^3 \oint dl\, r_{\shortparallel}^4}{\oint dl\, r_{\shortparallel}^2} \\
&- \frac{\rho_1-\rho_2}{\rho_1\sqrt{\frac{T_1}{T_{\text{eff}}}}+\rho_2\sqrt{\frac{T_2}{T_{\text{eff}}}}} \frac{\oint dl\, r_{\shortparallel}^3}{\oint dl\, r_{\shortparallel}^2} \\
&\times \Bigg[\frac{\rho_1\left(2\left(\frac{T_1}{T_{\text{eff}}}\right)^{3/2}+\frac{1}{2}\frac{T_{\text{eff}}}{T_1}\right)+\rho_2\left(2\left(\frac{T_2}{T_{\text{eff}}}\right)^{3/2}+\frac{1}{2}\frac{T_{\text{eff}}}{T_2}\right)}{\rho_1\sqrt{\frac{T_1}{T_{\text{eff}}}}+\rho_2\sqrt{\frac{T_2}{T_{\text{eff}}}}} \frac{\oint dl\, r_{\shortparallel}^4}{\oint dl\, r_{\shortparallel}^2} \\
&- \frac{\pi}{2}\frac{\left(\rho_1\frac{T1}{T_{\text{eff}}}-\rho_2\frac{T_2}{T_{\text{eff}}}\right)\left(\rho_1\left(\frac{T_1}{T_{\text{eff}}}-1\right)-\rho_2\left(\frac{T_2}{T_{\text{eff}}}-1\right)\right)}{\left(\rho_1\sqrt{\frac{T_1}{T_{\text{eff}}}}+\rho_2\sqrt{\frac{T_2}{T_{\text{eff}}}}\right)^2} \left(\frac{\oint dl\, r_{\shortparallel}^3}{\oint dl\, r_{\shortparallel}^2}\right)^2 \Bigg] \\
&+ \Bigg[\frac{\pi}{4}\left(\frac{\rho_1-\rho_2}{\rho_1\sqrt{\frac{T_1}{T_{\text{eff}}}}+\rho_2\sqrt{\frac{T_2}{T_{\text{eff}}}}} \frac{\oint dl\, r_{\shortparallel}^3}{\oint dl\, r_{\shortparallel}^2}\right)^2 - \frac{1}{3}\frac{\rho_1\sqrt{\frac{T_{\text{eff}}}{T_1}}+\rho_2\sqrt{\frac{T_{\text{eff}}}{T_2}}}{\rho_1\sqrt{\frac{T_1}{T_{\text{eff}}}}+\rho_2\sqrt{\frac{T_2}{T_{\text{eff}}}}} \frac{\oint dl\, r_{\shortparallel}^4}{\oint dl\, r_{\shortparallel}^2} \Bigg] \\
&\times \Bigg[\frac{\rho_1\left(2\left(\frac{T_1}{T_{\text{eff}}}\right)^2-\frac{9}{2}\frac{T_1}{T_{\text{eff}}}+\frac{5}{2}\right)-\rho_2\left(2\left(\frac{T_2}{T_{\text{eff}}}\right)^2-\frac{9}{2}\frac{T_2}{T_{\text{eff}}}+\frac{5}{2}\right)}{\rho_1\sqrt{\frac{T_1}{T_{\text{eff}}}}+\rho_2\sqrt{\frac{T_2}{T_{\text{eff}}}}} \frac{\oint dl\, r_{\shortparallel}^3}{\oint dl\, r_{\shortparallel}^2} \Bigg] \Bigg\}.
\end{aligned} \tag{5.107}$$

As before,

$$T_{\text{eff}} = \frac{\rho_1 T_1^{3/2}+\rho_2 T_2^{3/2}}{\rho_1 T_1^{1/2}+\rho_2 T_2^{1/2}}. \tag{5.108}$$

For the particular right triangle under consideration, the appearing contour integrals can be written as functions of the coordinates of the right

corner point (x_c, y_c), with $L = 1$:

$$\oint dl\, r_{\shortparallel}^2 = \frac{1}{6}L\Big(4L^2 + 6x_cL + 6y_cL + 6x_c^2 + 6y_c^2 \tag{5.109}$$

$$+ \sqrt{2}\left(L^2 + 3(x_c - y_c)^2\right)\Big), \tag{5.110}$$

$$\oint dl\, r_{\shortparallel}^3 = \frac{1}{2}L(x_c - y_c)\left(L^2 + 3(x_c + y_c)L + x_c^2 + y_c^2 + 4x_cy_c\right), \tag{5.111}$$

$$\oint dl\, r_{\shortparallel}^4 = \frac{1}{40}\Big(8\left((L + x_c)^5 - x_c^5\right) + 8\left(y_c^5 - (L + y_c)^5\right) \tag{5.112}$$

$$+ \sqrt{2}\left((L + x_c - y_c)^5 + (L - x_c + y_c)^5\right)\Big), \tag{5.113}$$

$$\oint dl\, r_{\shortparallel}^5 = \frac{1}{48}\Big(-(L + x_c - y_c)^6 + (L - x_c + y_c)^6 \tag{5.114}$$

$$+ 8\left((L + x_c)^6 - x_c^6\right) + 8\left(y_c^6 - (L + y_c)^6\right)\Big). \tag{5.115}$$

The moment of inertia finally, is given by

$$I/\varrho = \frac{1}{6}L^2\left(L^2 + 2(x_c + y_c)L + 3\left(x_c^2 + y_c^2\right)\right), \tag{5.116}$$

with $\varrho = M/(2A)$ and A the area of a triangle.

5.10.2 Refrigerator

We also tested the cooling function of the device with molecular dynamics simulations. If we assume ideal gases in both reservoirs, at temperatures T_1 and T_2 and with particle numbers n_1 and n_2, the change in time t of internal energy can be described by the following coupled set of equations:

$$\begin{aligned} n_1 k_B \dot{T}_1 &= \dot{Q}_J^1 - \dot{Q}_c + k(T_2 - T_1), \\ n_2 k_B \dot{T}_2 &= \dot{Q}_J^2 + \dot{Q}_c + k(T_1 - T_2). \end{aligned} \tag{5.117}$$

On the right hand sides we included three heat currents: the Joule dissipation ($\dot{Q}_J^i$), the cooling flow ($\dot{Q}_c$) and the heat conduction between the reservoirs $[k(T_j - T_i)]$. Earlier [cf. Eqs. (5.83), (5.79) and (5.104)] we described microscopic expressions for these terms. With notations γ_i for

the friction coefficient of each part, $\gamma = \gamma_1 + \gamma_2$, τ for the applied torque, I the inertial moment and ρ_i the particle densities, these were

$$\dot{Q}_J^i = \gamma_i \tau^2/\gamma^2, \tag{5.118}$$

$$\dot{Q}_c = \frac{\sqrt{2\pi k_B m T}}{2I} \frac{\rho_1\rho_2}{(\rho_1+\rho_2)^2} \frac{\oint dl\, r_{\shortparallel}^3}{\oint dl\, r_{\shortparallel}^2}\, \tau, \tag{5.119}$$

$$k = k_B \frac{\gamma_1\gamma_2}{\gamma I}. \tag{5.120}$$

The cooling flow $\dot{Q}_c$ was derived in the linear response regime, with $T = (T_1 + T_2)/2$.

We seek a solution of Eq. (5.117) with initial equilibrium conditions $T_1(0) = T_2(0) = T_0$. The dependence on T_i in Eq. (5.117) is rather involved, as the friction coefficients also depend on the temperature:

$$\gamma_i = 4\rho_i \sqrt{\frac{k_B T_i m}{2\pi}} \oint dl\, r_{\shortparallel}^2. \tag{5.121}$$

Therefore, an exact solution is only attainable numerically. Earlier, we established however that the generated relative temperature difference $|T_1 - T_2|/T$ is of order m/M (the ratio of masses of gas particle and device). For any physical realization of the device, m/M is very small, and we expect a substitution of $T_i = T_0$ in the expressions for the friction coefficients [Eq. (5.121)] to be a good approximation. In fact, as will be shown later in a graph with the simulation results, the ('exact') numerical solution and this approximation are indistinguishable for a ratio M/m as low as 20. In this approximation, the evolution of the two temperatures can be described analytically. For simplicity of the resulting expressions, we choose identical gases in both reservoirs, $n_1 = n_2 = n$ and $\rho_1 = \rho_2$, such that $\dot{Q}_J^1 = \dot{Q}_J^2 = \dot{Q}_J$, yielding:

$$\begin{aligned} T_1(t) &= T_0 + \frac{\dot{Q}_J t}{n k_B} - \frac{\dot{Q}_c}{2k}\left[1 - \exp\left(-\frac{2kt}{n k_B}\right)\right], \\ T_2(t) &= T_0 + \frac{\dot{Q}_J t}{n k_B} + \frac{\dot{Q}_c}{2k}\left[1 - \exp\left(-\frac{2kt}{n k_B}\right)\right]. \end{aligned} \tag{5.122}$$

For large reservoirs (n large), the effect is for T_1 to decrease and T_2 to increase when $\dot{Q}_c > \dot{Q}_J$ (see also the discussion about limiting torque,

Section 5.9.2). However, for small n, as will be used in molecular dynamics simulations because of obvious computational limitations, the effect of the Joule heating in both reservoirs will become apparent after a relatively short time t. More specifically, T_1 reaches its minimum,

$$T_1^{\min} = T_0 - \frac{\dot{Q}_c}{2k} + \frac{\dot{Q}_J}{2k}\left[1 + \ln\left(\frac{\dot{Q}_c}{\dot{Q}_J}\right)\right], \tag{5.123}$$

at time $t_{\min} = nk_B \ln\left(\dot{Q}_c/\dot{Q}_J\right)/(2k)$. For $t > t_{\min}$, T_1 increases. This is also what would happen if one would place a household refrigerator in a narrow confinement.

As the molecular dynamics simulations pose a practical limit on the number of gas particles, we resorted to a simple alternative scenario, to demonstrate the effect of a 'real' refrigerator. Here, we assume T_2 to be fixed ($T_2 = T_0$). This setup emulates an infinitely large second reservoir. Substitution of $T_2 = T_0$ in the first line of Eq. (5.117) leads to a solution for T_1 (in the approximation of temperature independent friction coefficients):

$$T_1(t) = T_0 - \frac{\dot{Q}_c - \dot{Q}_J}{k}\left[1 - \exp\left(-\frac{kt}{nk_B}\right)\right]. \tag{5.124}$$

T_1 decreases monotonically from T_0 and asymptotically reaches

$$T_1^{\min} = T_0 - \frac{\dot{Q}_c - \dot{Q}_J}{k}. \tag{5.125}$$

Both scenarios, T_2 free and fixed, were tested against molecular dynamics simulations. The rotor setup was the same for both scenarios. Again, two right triangular rotor parts were placed in separate boxes. The configuration in one box was the mirrored copy of the other. One triangle had sides $1/\sqrt{2}, 1/\sqrt{2}, 1$. With x-axis and y-axis parallel to the short sides of the triangle and origin at the center of rotation $(0, 0)$, the center of mass for the following simulations was placed at $(-0.2, 0.1)$. The total mass of the rotor was $M = 20$. Densities in both reservoirs were $\rho_1 = \rho_2 = 2.5$. The initial temperature (at $t = 0$) was $T_0 = 1$ for both boxes. For the first scenario (both gases can change in temperature), closed boxes were used. For the second scenario [$T_2(t) = T_0$], the

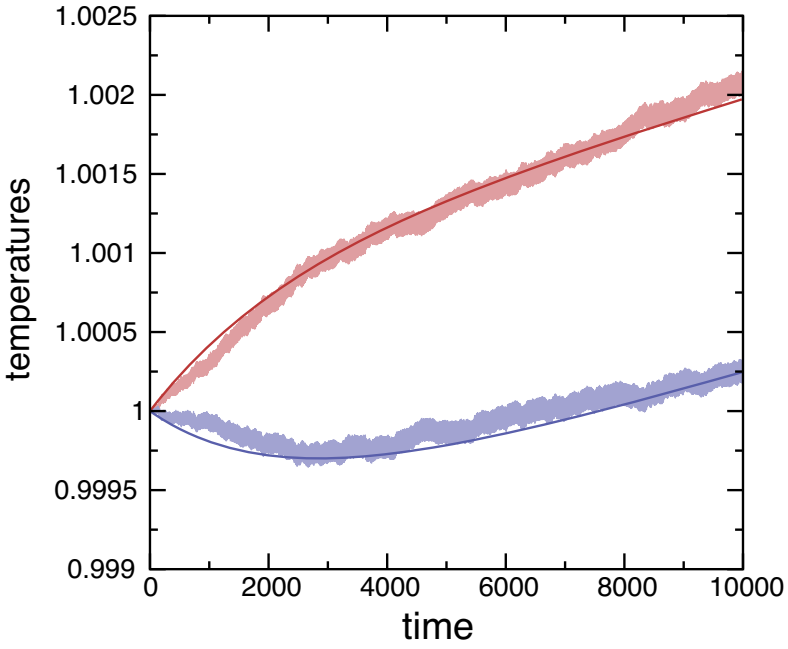

Figure 5.29: Molecular dynamics simulations of the Brownian refrigerator. Shown are the evolution of temperatures T_1 and T_2 of both gases in time, starting from equal initial temperature $T_0 = 1$, on application of a torque. Solid curves are theoretical calculations (numerical and analytical approximation indistinguishable in the graph). For parameters see main text.

box of the second gas was virtual. The applied torque was $\tau = 0.02$. The simulations generated 10 000 realizations for each scenario.

In Figs. 5.29 and 5.30 we compare the theoretical predictions with the simulation results for the first and the second scenario respectively. The cooling effect is certainly apparent. The theoretical curves (solid) correspond well to the simulations, considering the statistical accuracy of the simulations. The derived expressions for minimum temperatures are in good agreement.

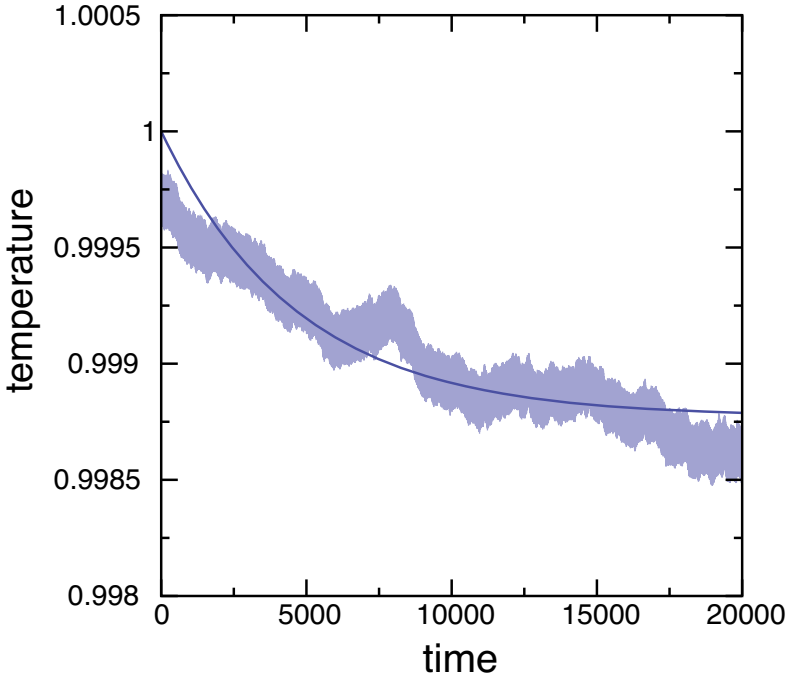

Figure 5.30: Molecular dynamics simulations of the Brownian refrigerator. Shown is the evolution of the temperature T_1 of the cooled gas in time [starting from $T_1(t = 0) = T_0 = 1$], when an infinitely large reservoir is emulated for the second gas [$T_2(t) = T_0$], on application of a torque. The solid curve represents the theoretical prediction (numerical and analytical approximation indistinguishable in the graph). For parameters see main text.

Acknowledgements

First of all, and perhaps a little unconventional for a thesis acknowledgement, I would like to express my gratitude for the very pleasant time I spent at the university where this work was done and in extension, the place where I lived for the previous three years. After moving to Hasselt, I was often very pleasantly surprised by the helpfulness and friendliness of the university staff and the people I met in my daily life.

It was a great privilege to work with Christian Van den Broeck. I thank Chris for his confidence in me when he selected me for the job and for the very fascinating topics he suggested me to work on. What I have learned under his guidance goes well beyond scientific knowledge and will certainly help me in my future plans.

I thank Bart Cleuren for his tremendous help. Bart possesses the peculiar and very useful quality that he is undaunted by any physics problem. I thank Bart for all the times we spent in his office going over the tiniest details of my work.

I very much enjoyed the collaboration with Ralf Eichhorn at Bielefeld University. I thank Ralf for all his efforts, especially in the final phase of my PhD, to have all the simulation results ready on time. And thank you for nicely covering my theoretical curves with data points...

I was also fortunate to have an opportunity to work with Jori Liesenborgs. I have the impression Jori only needed half a word to understand what I wanted to do.

I worked in a fantastic group. Mieke Gorissen was always there for help, conversation or diversion. I'm sure there would be less physics students enrolled at Hasselt University if it wasn't for Mieke. And now it's a written promise: I will return the tent, cleaned. Bob Rutten was a great office mate. Thank you for the snooker lessons and please drive safely (don't take my example!). I wish Mieke and Bob all the best with their PhD work. I was happy to be able to assist Carlo Vanderzande in teaching, he is one of the best physics educators I know. My lunch and

coffee breaks would not have been as relaxing or stimulating (depending on my need) without the company of Bart, Bob, Carlo and Mieke.

I also want to show my appreciation for the opportunity to meet with great scientists: Juan Parrondo, Lutz Shimanski-Geier, Raul Toral, Stephan Grill, Luca Peliti, Fabio Marchesoni, Igor Sokolov, Chris Jarzynski, Peter Reimann and many others. Conversations with them were a great stimulus for my own work. The same can be said of my fellow PhD students in statistical physics (now postdocs): David Andrieux and Alex Gomez-Marin. I certainly hope to meet you all again.

I am grateful to Venkataraman Balakrishnan for the chats during his guest professorship here and for his invitation to the Indian Institute of Technology in Madras, which allowed me to discover not only a very different academic environment, but an entire subcontinent as well.

I also keep fond memories of the eight week summer school at St. Etienne de Tinée. Best of luck to my fellow PhysBio students: Andrei Akhmetzhanov, Bruno Escribano, Christian Brettschneider, Christian Wolff, Flora Bacelar, Ignacio Peixoto, John Robinson, Jorge Carballido, Jorge Mejias, Katus Kovacs, Marcelo Weber Schiller, Niko Komin, Philipp Altrock, Sabino Metta, Sebastian Reyes, Sten Rüdiger, Toni Perez and of course Vanesse. We should organize a reunion party.

Thank you to all the people in Hasselt, Antwerp and Italy who gave me continuing support, friendship and hospitality.

I thank all the aunts and uncles for the various invitations for dinners and lifts to airports.

There is no way to thank Mara enough for all her support, love and trust in me.

I am indebted for the lifelong encouragement by my parents. They saw a biologist in me when I was very young. I'm sorry it turned out to be physics, but I hope this thesis makes up for something.

My deepest gratitude goes to my beloved brother. At one point you couldn't find me but now I'm back, to stay...

Samenvatting

Omdat we gewend zijn aan onze 'macroscopische' leefwereld, is het moeilijk om ons voor te stellen hoe een microscopisch klein voorwerp beweegt op nanometerschaal. Eén nanometer is één miljoenste van een millimeter. In een vloeistof wordt elke systematische beweging van het deeltje bijna ogenblikkelijk gedempt door de voortdurende interacties met de vloeistofdeeltjes. De enige beweging die overblijft, als we geen externe kracht uitoefenen op het voorwerp, is een willekeurige beweging, een 'wandeling' zonder richting. *Netto*, over lange tijd bekeken, verplaatst het voorwerp zich helemaal niet. Door de botsingen met de omgevingsdeeltjes is de energie van het voorwerp ook steeds 'uit evenwicht'. Onze vertrouwde (thermodynamische) principes over de efficiënte omzetting van energie in arbeid, die vertrekken van systemen in evenwicht, kunnen we dan ook niet zomaar overnemen naar de nanowereld.

Twee recente ontwikkelingen liggen aan de basis van dit werk. Enerzijds begrijpen we steeds beter hoe biologische systemen op de kleinste schaal bewegen. Vermeldenswaard zijn de stapsgewijze beweging van kinesinemoleculen over het cytoskelet en de draaiende beweging van F_1-ATPase. Beide behoren tot de klasse van zogenaamde 'moleculaire motoren'. Anderzijds is er de spectaculaire vooruitgang in de 'nanotechnologie'. Het is nu mogelijk materie op moleculaire schaal te manipuleren en zodoende allerlei functionaliteiten, zoals radertjes, schakelaars en zelfs motortjes op nanoschaal te bouwen.

In het ontwerp van deze artificiële apparaatjes wordt tot nog toe weinig rekening gehouden met de specifieke problemen die zich stellen op deze kleine schaal. Het storende effect van de omgeving wordt overwonnen door brute kracht. Een *Brownse motor* daarentegen *gebruikt* juist de willekeurige interacties met de omgeving op een slimme manier en zet ze maximaal om in een nuttig resultaat: een *netto* verplaatsing; of gerelateerd ermee: een arbeid. Om dit gelijkrichtende effect van willekeurige fluctuaties te bereiken moet de motor twee symmetrieën breken.

Enerzijds moet het thermisch evenwicht verstoord worden. Anders zou men arbeid kunnen putten uit een systeem in evenwicht, wat in strijd is met de basiswetten van de thermodynamica. Anderzijds moet de ruimtelijke symmetrie op één of andere manier gebroken worden, zodat een 'voorkeursrichting' ontstaat, waarin dan de netto verplaatsing geschiedt.

De studie van Brownse motoren waarbij de ruimtelijke symmetrie gebroken wordt door de specifieke *vorm* van de onderdelen van de motor, maakt het onderwerp uit van een deel van dit proefschrift. In een specifieke realisatie van de motor, de *thermische Brownse motor* wordt de noodzakelijke verstoring uit thermisch evenwicht teweeggebracht door het plaatsen van de verschillende onderdelen van de motor in omgevingen met *verschillende* temperatuur. Een volledig analytische berekening, waarin de interacties tussen de motor en de omgeving exact microscopisch worden behandeld, leidt dan tot bijvoorbeeld de netto snelheid die zo'n thermische Brownse motor kan behalen. Een voorbeeld: een motortje dat bestaat uit twee vast verbonden kegelvormige onderdelen, elk ongeveer 20 nanometer groot en in contact met omgevingen met een temperatuursverschil van 0,1 kelvin, haalt een *gemiddelde* snelheid van 0,1 micrometer per seconde (één micrometer is één duizendste van een millimeter).

We introduceren ook de *roterende* variant van de thermische Brownse motor. De verschillende onderdelen zijn dan vast verbonden met een rotatieas, waarrond het geheel kan draaien. We laten zien dat de 'Brownse rotor' zich heel anders gedraagt naar gelang de specifieke inplanting van de as. Heel intrigerend is ook hoe de noodzakelijke vormasymmetrie zich vertaalt in concrete vormen. *Chiraliteit* bleek hier van essentieel belang en optimaliseren van de vorm om een zo hoog mogelijke rotatiefrequentie te bereiken, resulteerde in een spiraalachtige figuur.

Een derde type Brownse motor werd op een heel andere manier verwezenlijkt. Nog steeds vertrokken we van een ruimtelijk asymmetrisch vormpje, maar dit maal slechts in contact met één thermische omgeving. Op het motortje wordt een fluctuerende kracht uitgeoefend, maar zó dat die netto opgeteld in de tijd nul is. Een symmetrisch lichaam beweegt wel heen en weer in zo een krachtveld, maar *netto* verplaatst het zich niet. Het bijzondere aan *asymmetrische* vormen is dat ze zich in het beschreven krachtveld wél netto verplaatsen en we hebben een formule afgeleid voor de zogenaamde driftsnelheid van dit type motortjes.

Een ander deel van dit proefschrift beschrijft het concept van een

warmtepomp of koelkast op nanometerschaal. Hiervoor vertrekken we van de roterende versie van de thermische Brownse motor. Het toestelletje heeft twee asymmetrische onderdelen die zich elk in een ander reservoir bevinden. Door het aanleggen van een *rotatiekracht* (krachtmoment) ontstaat er, via de verstoorde thermische fluctuaties, een warmtestroom van het ene naar het andere reservoir. Dit betekent we warmte kunnen 'pompen' *uit* één reservoir, en dat dit na verloop van tijd zal afkoelen. De volledige analyse is ingewikkelder: er treden immers nog andere warmtestromen op dan de beschreven koelingsstroom. Door het draaien van het rotortje gaat er door wrijving warmte naar beide reservoirs. Anderzijds is er een onvermijdelijke warmtestroom van het warme naar het koude reservoir, eenmaal er een temperatuursverschil gerealiseerd is. De vergelijking van deze warmtestromen leidt tot verdere mogelijkheden om de werking van de koelkast de optimaliseren en meer bepaald tot de beste waarde voor de aan te brengen rotatiekracht. De maximale koeling van de Brownse nanokoelkast is uiteraard bijzonder klein (femtojoules per seconde), maar de kleine afmetingen maken het erg geschikt om vele exemplaren in één laag te assembleren en zo het koelingsvermogen sterk te verhogen.

Verschillende resultaten van dit theoretische werk werden ook geverifiëerd met behulp van een computersimulatietechniek. Hierin werden de interagerende deeltjes uit de omgeving elk afzonderlijk gevolgd en de interacties exact berekend. De prestaties van de geïntroduceerde motortjes en koelkasten bleken de theoretische voorspellingen heel goed na te komen

List of Figures

List of Tables

List of Tables

Bibliography

[1] M. Nishiyama, E. Muto, Y. Inoue, T. Yanagida, and H. Higuchi, Nature Cell Biology **3**, 425 (2001); M. Nishiyama, H. Higuchi, and T. Yanagida, Nature Cell Biology **4**, 790 (2002).

[2] H. Noji, R. Yasuda, M. Yoshida, and K. Kinosita, Nature **386**, 299 (1997).

[3] R. Yasuda, H. Noji, K. Kinosita, Jr, and M. Yoshida, Cell **93**, 1117 (1998).

[4] P. Hänggi and F. Marchesoni, cond-mat/0807.1283 preprint, 2008.

[5] R. P. Feynman, *There's plenty of room at the bottom*, Caltech's Engineering and Science Magazine, Pasadena (1960).

[6] K. E. Drexler, *Nanosystems: Molecular Machinery, Manufacturing and Computation*, Wiley, New York (1992).

[7] M. Gross, *Travels To The Nanoworld*, Perseus, New York (1999).

[8] L. Gao, Q. Liu, Y. Y. Zhang, N. Jiang, H. G. Zhang, Z. H. Cheng, W. F. Qiu, S. X. Du, Y. Q. Liu, W. A. Hofer, and H.-J. Gao, Phys. Rev. Lett. **101**, 197209 (2008).

[9] A. Einstein, Ann. Phys. **17**, 549 (1905).

[10] M. v. Smoluchowski, Phys. Z. **13**, 1069 (1912).

[11] R. P. Feynman, R. B. Leighton, and M. Sands, *The Feynman Lectures on Physics I*, Addison-Wesley, Reading, MA (1963).

[12] J. M. R. Parrondo and P. Espagnol, Am. J. Phys. **64**, 1125 (1996).

[13] M. O. Magnasco, Phys. Rev. Lett. **71**, 1477 (1993).

[14] A. Ajdari and J. Prost, C. R. Acad. Sci. Paris (Ser. II) **315**, 1635 (1992).

[15] R. D. Astumian and M. Bier, 1994, Phys. Rev. Lett. **72**, 1766 (1994).

[16] R. Bartussek, P. Hänggi, and J. G. Kissner, Europhys. Lett. **28**, 459 (1994).

[17] C. R. Doering, W. Horsthemke, and J. Riordan, Phys. Rev. Lett. **72**, 2984 (1994).

[18] J. Prost, J. F. Chauwin, L. Peliti, and A. Ajdari, Phys. Rev. Lett. **72**, 2652 (1994).

[19] J. Rousselet, L. Salome, A. Ajdari, and J. Prost, 1994, Nature **370**, (1994).

[20] R.D. Astumian, Science **276**, 917 (1997).

[21] F. Jülicher, A. Ajdari, and J. Prost, Rev. Mod. Phys. **69**, 1269 (1997).

[22] P. Reimann, Phys. Rep. **361**, 57 (2002).

[23] P. Hänggi and R. Bartussek, *Lecture Notes in Physics*, Parisi J., Müller S. C., and Zimmermann W., Vol **476** Springer, Berlin (1996) 294-308.

[24] W. R. Browne and B. L. Feringa, Nature Nanotech. **1**, 25 (2006).

[25] B. L. Feringa, J. Org. Chem. **72**, 6635 (2007).

[26] M. A. Garcia-Garibay, Proc. Natl. Acad. Sci. **102**, 10771 (2005).

[27] A. M. Fennimore, T. D. Yuzvinsky, Wei-Qiang Han, M. S. Fuhrer, J. Cumings, and A. Zettl, Nature **424**, 408 (2003).

[28] C. Van den Broeck and R. Kawai, Phys. Rev. Lett. **96**, 210601 (2006).

[29] C. Van den Broeck, Phys. Rev. Lett. **95**, 190602 (2005).

[30] C. Van den Broeck, Adv. Chem. Phys. **135**, 189 (2007).

[31] M. van den Broek and C. Van den Broeck, Phys. Rev. Lett. **100**, 130601 (2008).

[32] N. G. van Kampen, *Stochastic Processes in Physics and Chemistry*, North-Holland, Amsterdam (1981).

[33] C. Van den Broeck, R. Kawai, and P. Meurs, Phys. Rev. Lett. **93**, 090601 (2004).

[34] P. Meurs, C. Van den Broeck, and A. Garcia, Phys. Rev. E **70**, 051109 (2004).

[35] C. Van den Broeck, P. Meurs, and R. Kawai, New J. Phys. **7**, 10 (2005).

[36] P. Meurs and C. Van den Broeck, J. Phys.: Condens. Matter **17**, S3673 (2005).

[37] L. Onsager, Phys. Rev. **37**, 405 (1931); *ibid.* **38**, 2265 (1931).

[38] I. S. Gradshteyn and I. M. Ryzhik, *Table of Integrals, Series, and Products*, Academic, New York (1980).

[39] P. S. Epstein, Phys. Rev. **23**, 710 (1924).

[40] A. M. Brouwer, C. Frochot, F. G. Gatti, D. A. Leigh, L. Mottier, F. Paolucci, S. Roffia, G. W. H. Wurpel, Science **291**, 2124 (2001).

[41] V. Balzani, M. Clemente-León, A. Credi, B. Ferrer, M. Venturi, A. H. Flood, and J. F. Stoddart, Proc. Natl. Acad. Sci. **103**, 1178 (2006).

[42] H. Linke, M. T. Downton, and M. J. Zuckermann, Chaos **15**, 026111 (2005).

[43] S. Leibler, Nature **370**, 412 (1994).

[44] R. Landauer, J. Stat. Phys. **53**, 233 (1988).

[45] K. Sekimoto, Progr. Theor. Phys. Suppl. **130**, 17 (1998).

[46] C. Jarzynski and O. Mazonka, Phys. Rev. E **59**, 6448 (1999).

[47] N. Nakagawa and T. S. Komatsu, Europhys. Lett. **75**, 22 (2006).

[48] J. P. Pekola and F. W. J. Hekking, Phys. Rev. Lett. **98**, 210604 (2007).

[49] H. B. Callen, *Thermodynamics and an Introduction to Thermostatistics*, Wiley, New York (1985).

[50] M. van den Broek, R. Eichhorn, J. Liesenborgs, and C. Van den Broeck, unpublished.

[51] M. van den Broek and C. Van den Broeck, Phys. Rev. E **78**, 011102 (2008).

[52] K. Handrich and F.-P. Ludwig , J. Stat. Phys. **86**, 1067 (1997).

[53] S. Sporer, C. Goll, and K. Mecke, Phys. Rev. E **78**, 011917 (2008).

[54] B. Cleuren B. and C. Van den Broeck, Europhys. Lett. **77**, 50003 (2007).

[55] B. Cleuren and R. Eichhorn, J. Stat. Mech., P10011 (2008) .

[56] G. Costantini, U. M. B. Marconi, and A. Puglisi, Europhys. Lett. **82**, 50008 (2008).

[57] H. Itoh et al., Nature **427**, 465 (2004).

www.uhasselt.be

Universiteit Hasselt | Campus Diepenbeek
Agoralaan | Gebouw D | BE-3590 Diepenbeek | België
Tel.: +32(0)11 26 81 11